THESIS FOR THE DEGREE OF DOCTOR OF PHILOSOPHY

Radiative Heat Transfer in Suspension-Fired Systems

ADRIAN GUNNARSSON

Department of Space, Earth and Environment

CHALMERS UNIVERSITY OF TECHNOLOGY

Gothenburg, Sweden 2019

Radiative Heat Transfer in Suspension-Fired Systems
ADRIAN GUNNARSSON
ISBN 978-91-7905-142-6

Doktorsavhandlingar vid Chalmers tekniska högskola
Ny serie nr 4609
ISSN 0346-718X

Department of Space, Earth and Environment
Division of Energy Technology
Chalmers University of Technology
SE-412 96 Gothenburg
Sweden
Telephone + 46 (0)31-772 1000

COVER: Schematic representation of the different possible heat transfer mechanisms involving convection (q''_{conv}), conduction (q''_c), and radiation (q''_r, E) within a cross-section of a rotary kiln with a present, and moving, bed material.

Printed by Chalmers Reproservice
Chalmers University of Technology
Gothenburg, Sweden 2019

Radiative Heat Transfer in Suspension-Fired Systems

ADRIAN GUNNARSSON
Division of Energy Technology
Department of Space, Earth and Environment
Chalmers University of Technology

Abstract

Radiation is the dominating heat transfer mechanism in most furnaces, and the radiative properties of combustion products represent important aspects regarding its suitability as a heat source. However, fuel and energy markets are undergoing rapid changes due to increasing concerns related to the security of supply and increased global warming. Industrial processes that have traditionally relied on a specific fuel must increase their flexibility in terms of their energy supply. Therefore, an increased understanding and improved modeling capacity of radiative heat transfer are required to facilitate a more rapid evaluation and implementation of novel fuels in large furnaces that have reduced emissions and sustained efficiency. For such studies, digital twins of processes may be a useful and economical alternative.

This PhD thesis on radiative heat transfer focuses on: (i) the application to one industrial process, i.e., rotary kilns for heat treatment of iron ore pellets; and (ii) radiative heat transfer from soot particles in various propane flames. In-flame measurements of the combustion conditions, radiative intensities and radiative heat fluxes were performed during several measurement campaigns with different burners, furnace geometries and fuels, including gaseous, coal, and co-firing fuels. The radiative heat transfer was modeled using a discrete transfer model and a 3D-modeling tool that applies a discrete ordinates method, with the latter being developed within this thesis.

The 3D-modeling tool was used to study the heat transfer conditions within the rotary kiln, as well as the heat treatment of the bed material, and a first attempt to validate the model in relation to actual measurements was made. Radiation was shown to account for more than 80% of the total heat transferred to the bed material, and the flame radiation was dominated by the particles present. Nevertheless, the possibility of using co-firing, including up to 30% biomass, was found to be feasible, and was not expected to have any significant impact on the radiative heat transfer within the process.

The soot volume fraction and the radiative properties of soot particles were measured following gas extraction and using a laser-induced incandescence system for the various propane flames, while altering the combustion conditions and oxidizer composition. The modeled radiative intensities of the flames correspond well with the measured values, indicating that the soot volume fraction was accurately measured by either technique. Furthermore, very high soot volume fractions were observed when there were high concentrations of oxygen in the oxidizer, revealing the potential for promoting the radiative heat transfer in such furnaces.

Keywords: Radiative heat transfer, combustion, rotary kiln, co-firing, soot volume fraction

List of Publications

This thesis is based on the following papers, which are referred to in this thesis according to their Roman numerals:

I. A. Gunnarsson, D. Bäckström, R. Johansson, C. Fredriksson, K. Andersson, *Radiative Heat Transfer Conditions in a Rotary Kiln Test Furnace Using Coal, Biomass and Cofiring Burners,* Energy and Fuels, 2017, 31, 7482-7492.

II. A. Gunnarsson, K. Andersson, B. Adams, C. Fredriksson, *Modelling the Radiative Heat Transfer in a Pilot-Scale Rotary Kiln Using a Discrete Ordinates Method,* submitted for publication.

III. A. Gunnarsson, K. Andersson, B. Adams, C. Fredriksson, *Full-Scale 3D-Modelling of the Radiative Heat Transfer in Rotary Kilns with a Present Bed Material,* submitted for publication.

IV. A. Gunnarsson, J. Simonsson, D. Bäckström, M. N. Mannazhi, P. E. Bengtsson, K. Andersson, *Radiative Heat Transfer Modeling and in Situ Diagnostics of Soot in an 80 kW_{th} Propane Flame with Varying Feed-Gas Oxygen Concentration,* Industrial & Engineering Chemistry Research, 2018, 57, 12288-12295.

V. D. Bäckström, A. Gunnarsson, D. Gall, X. Pei, R. Johansson, K. Andersson, R. K. Pathak, J. B. C. Pettersson, *Measurement of the Size Distribution, Volume Fraction and Optical Properties of Soot in an 80 kW Propane Flame,* Combustion and Flame, 2017, 186, 325-334.

In addition, the following paper is included in the Appendix:

A. J. Simonsson, A. Gunnarsson, M. N. Mannazhi, D. Bäckström, K. Andersson, P.-E. Bengtsson, *In-situ Soot Characterization of Propane Flames and Influence of Additives in a 100 kW Oxy-Fuel Furnace Using Two-Dimensional Laser-Induced Incandescence,* Proceedings of the Combustion Institute, 2019, 37, 833-840.

Adrian Gunnarsson is the principal author of Papers I–IV and responsible for the modeling, evaluation of the data and measurements related to radiative heat transfer. As second author, he has contributed with writing, discussion and editing of Papers V and A, and also contributed with modeling in Paper V and experiments in Paper A. Dr. Daniel Bäckström is the principal author and responsible for the measurements of Paper V. He also conducted measurements regarding the oil flame studied in Paper III, and has further contributed with guidiance in the modeling and experimental work, as well as with discussions and editing of Paper I. Dr. Christian Fredriksson has organized the experimental campaigns and provided the industrial perspective of the rotary kiln process in Papers I-III. Dr. Johan Simonsson, the principal author of Paper A, and doctoral student Manu Naduvil Mannazhi have together with Professor Per-Erik Bengtsson contributed with optical measuremetns and expertise regarding the laser-induced incandescenece experiments as well as data processing and editing of Paper IV. Dr. Dan Gall, Dr. Xiangyu Pei, Associate Professor Ravi Kant Pathak, and Professor Jan B. C. Pettersson have contributed with measurements and expertise during the particle experimetns in Paper V. Professor Klas Andersson has contributed with guidance in the experimental work and toghether with Associate Professor Bradley Adams and Dr. Robert Johansson, contributed with guidance and discussion of the modeling work as well as editing of the papers.

Additional work related to the topics of this thesis:

a) F. Normann, A. Gunnarson, K. Andersson, S. Nordgren, J. Sandberg *First Evaluation of Iron-Ore Pelletization with Improved Heat Utilization,* Clearwater Clean Energy Conference, 2017.

b) L. Houghton, B. Adams, A. Fry, A. Gunnarsson, K. Andersson *Radiometer Measurements in High Pressure Flames: System Design, Sensors and Calibration,* Clearwater Clean Energy Conference, 2018.

Acknowledgments

First of all, I would like to thank my examiner and supervisor Klas Andersson for all the support and guidance you have given me throughout this work in this interesting field of research. Your inspiring ideas have made me want to go further. Thank you, Bradley Adams, for supervising me in the modeling work, our discussions and your editing.

The measurements during the experimental campaigns would not have been possible to conduct without the invaluable help from Rikard Edland, Daniel Bäckström, Thomas Allgurén, Dan Gall, Johan Simonsson, Manu Mannazhi, Johannes Öhlin and Rustan Hvitt, thank you all. Special thanks to Daniel Bäckström, for your guidance in experimental as well as in modeling work and for enlightening my path in the area of radiative heat transfer.

LKAB and the Swedish Energy Agency are acknowledged for the financial support of this work. Special thanks to Christian Fredriksson, Johan Sandberg and Samuel Nordgren for the great collaboration. I would also like to thank the co-authors of my papers. Your help and input to this work is very much appreciated.

Thank you, Robert Johansson, for giving me a great start in my doctoral studies and your guidance in radiative heat transfer modeling. Fredrik Normann, thank you for all the inspiring collaboration and for pushing me forward in research as well as on the running track – We Love Combustion!

Thank you, Anna Köhler, for sharing the "Design office" and always *bee*-ing so positive and enthusiastic! Rikard Edland, for all the discussions, the many hours spent together in and out of office, and for the conclusion to always invest more. Tove Djerf, for being the great friend and colleague that you are. Thanks to the "A-team" for always taking the time to help with a little bit of everything. To all my current and former colleagues at Energy Technology, thank you for the interesting discussions, gaming nights, all the laughs, and for creating such a pleasant working place.

To my family that have always supported and encouraged me to go further but also to remind me to take some time for rest. I am Very Thankful to my friends, the Cheerful People whom Make my Life So Much more Spontaneous, Adventurous and full of Joy when not at the Job.

Finally, to Hilda, what would I do without your love and support? I treasure every minute that I can spend with you and I look forward for our future together – you truly are the best.

Adrian Gunnarsson
Lofoten, Norway, 2019

Table of Contents

1. Introduction 1
1.1 Combustion and Thermal Radiation 2
1.2 The Rotary Kiln Process 6
1.3 Aims and Objective 9
2. Previous Work and Progress Made 11
2.1 Rotary Kilns 12
2.2 Heat Radiation from Soot Particles 16
2.3 Co-Firing in a 1.5 MW_{th} Furnace 18
3. Heat Transfer Modeling 19
3.1 Radiative Heat Transfer 19
3.2 Cylindrical Furnaces 25
3.3 Rotary Kilns with a Passing Bed Material 33
4. Measurement Techniques 39
4.1 Intrusive Measurements 39
4.2 Non-intrusive Measurements 43
5. Experimental Furnaces 45
5.1 Experimental Combustion Furnace 45
5.2 Kiruna Kulsinterverk 2 46
5.3 Oxy-Fuel Test Rig 46
5.4 L1500 Multifuel Furnace 47
6. Selected Results and Discussion 49
6.1 Pilot-Scale Rotary Kiln 49
6.2 Industrial Full-Scale Rotary Kiln 52
6.3 Co-Firing in the L1500 Multifuel Furnace 53
6.4 Radiative Properties of Soot Particles 54
7. Conclusions 57
8. Suggestions for Future Work 59
9. Nomenclature 61
10. Bibliography 67

"....plus the fact that there may be literally millions of spectral lines, makes radiative transfer calculations a truly formidable task." – Michael F. Modest

Outline

This PhD thesis consists of a summary of the work (in ten chapters), the five appended papers, and an appendix. The first two chapters briefly describe the background to the topics included in the thesis and provide an overview of what has previously been done in this area by our research group. Chapter 3 describes the different heat transfer models used and developed in this thesis and the main equations of interest. Chapters 4 and 5 provide descriptions of the measuring equipment and the techniques used, as well as the furnaces studied in the measurement campaigns. Chapters 6 and 7 show some selected results, together with the associated discussions and conclusions drawn from the work. The thesis ends with some ideas for future work, a list of the nomenclature used, and a bibliography.

Papers I–III focus on the heat transfer in a rotary kiln used for iron ore pelletizing. Paper I assesses the possibility of using co-firing of coal and biomass in the grate-kiln process, which is used in the production of iron ore pellets. The radiative intensity and heat flux are measured, along with the gas temperatures, gas compositions, and particle concentrations in a cylindrical, pilot-scale rotary kiln at 580 kW_{th}. An axisymmetric discrete transfer model is used to model the radiative heat transfer, and the radiative heat profiles for different fuel combinations are compared. Paper II presents the development of a modeling tool applying a discrete ordinates method in order to enable studies of the radiative heat transfer along the axis of a furnace. The paper further evaluates the measurements obtained in the pilot-scale rotary kiln and the radiative heat flux and wall temperatures are modeled, and the addition of a colder bed material is examined. Paper III applies and elaborates the model used in Paper II to include conductive and convective heat transfers, as well as the movement and mixing of the bed material. Collected measurements and process data are used to model a full-scale industrial rotary kiln including the properties of the iron ore pellet bed.

Papers IV and V focus on the radiative heat transfer properties in propane flames, with the soot volume fraction being quantified using different measurement techniques. The radiative intensity is modeled using the discrete transfer model. In Paper IV, the soot concentration is altered by varying the oxygen concentration in the oxidant using oxygen-enriched air. The soot volume fraction is measured using laser-induced incandescence, together with an extinction laser. In Paper V, scanning mobility particle sizer spectrometry is used to measure the soot volume fractions for a non-sooty flame and a sooty flame. A photo-acoustic soot spectrometer is used to study the absorption and scattering coefficients of the soot particles at three wavelengths.

Paper A studies, in similarity to Paper IV, the soot volume fraction and how it varies for different oxygen concentrations using laser-induced incandescence, but for oxy-fuel propane flames. Appendix B presents measurement data gathered from co-firing flames conducted in a pilot-scale rotary kiln.

1. Introduction

Currently, vast amounts of greenhouse gases are being emitted continuously from industrial and electricity-producing sectors, associated with high energy and product demands, thereby contributing to increasing global warming. These emissions mainly originate from the combustion of fossil fuels around the world, with the produced carbon dioxide being of the greatest concern. While greenhouse gas emissions are often difficult to eliminate, preventing further global warming is considered to be one of the most urgent, as well as challenging, tasks of our time. The greenhouse gas emissions from electricity production can be drastically reduced by employing renewable energy sources, such as solar and wind power. Nonetheless, combustion processes remain important and necessary for many industries, as well as for the global energy system. Instead, replacing the fossil fuel with fully renewable fuels, e.g., exchanging coal with biomass, could be a part of the solution. Even substituting a portion of the fuel, using so-called 'co-firing' of fossil coal and renewable biomass, would eliminate some of the emissions. Another approach is to capture the carbon dioxide emitted from the combustion and store it (i.e., carbon capture and storage), thereby preventing the gases from ever reaching the atmosphere. Finally, emissions of greenhouse gases can be reduced by improving the efficiency of the combustion process. Moreover, by making the combustion process more efficient, the emissions levels of other products (gases or particles) can also be reduced. While carbon dioxide is linked to increases in global warming, other combustion products, such as soot particles, may have more direct and negative effects on human health.

To improve combustion processes, it is necessary to study and understand how heat is transferred through convection, conduction and radiation within the furnace. In suspension-fired furnaces that have luminous flames, heat transfer is mainly via radiation, which in some processes accounts for up to 90% of the total heat transfer [1]. Modeling tools, such as digital twins of processes, can be helpful and economical options for such studies. The radiative properties of the combustion gases and particles present are, however, complex but important to consider, since they contribute to the radiation through emission, absorption, and scattering. Therefore, it is of great interest to measure experimentally and using detailed theoretical models of the radiative heat transfer in combustion processes. To fully capture the total heat transfer, it is also necessary to model the convective and conductive heat transfers occurring in the furnace.

This thesis focuses on studies of radiative heat transfer from flames, using a gaseous or solid fuel in cylindrical, semi-cylindrical and cuboid furnaces. The impacts on radiative heat transfer of the soot particles in propane flames under various combustion conditions are studied, whereby the soot volume fraction is measured using two different techniques. The heat transfer in a coal- or oil-fired industrial, as well as a pilot-scale rotary kiln used for iron ore pelletizing are studied, involving both measurements and modeling work, including the development of a modeling tool to study the heat treatment of the bed material. Co-firing of coal and biomass is studied in the same pilot-scale rotary kiln, as well as in a horizontal, cuboid furnace.

1.1 Combustion and Thermal Radiation

Fuel combustion is a commonly used and effective way to generate heat and energy required by different processes, ranging from individual transportation and domestic heating systems to industrial processes and electricity production. During combustion, chemical energy is converted to hot gases as well as particles and heat is transferred to the surroundings via convection, conduction and radiation. In contrast to convective and conductive heat transfers, radiative heat transfer occurs at the speed of light, and while it may interact with a medium, no interacting medium is required for the transfer. At higher temperatures, such as in a flame, heat is more effectively transferred due to radiation, and it may dominate both convective and conductive heat transfers in a furnace. The fuel can be in gaseous, liquid or solid form, and the choice of fuel is determined by several parameters, such as the application, availability, heating value, and price. The radiative properties are, in turn, dependent upon the fuel and combustion conditions used. Therefore, it is important to understand the radiative heat transfer with the context of combustion. This work focuses on the combustion of hydrocarbon fuels, being coal, wood, and propane, using air, oxygen-enriched air or recirculated flue gases with additional oxygen as the oxidizer, in the so-called 'oxy-fuel combustion'.

1.1.1 Combustion Products

The products obtained from the complete, and desired, combustion of hydrocarbon fuels with air are carbon dioxide, water steam, and nitrogen. However, the fuel often contains various impurities, the combustion may be incomplete, and other bioproducts (e.g., nitrogen oxides) are formed, resulting in a flue gas mixture that contains several compounds and particle types. When modeling the radiative heat transfer, one must take into account the radiative properties of the different gases and particles.

Gases

The many rotational and vibrational energy levels available for the gaseous compounds enable, at combustion temperatures, the emission and absorption of electromagnetic waves in the infrared wavelength range. The potential absorption of these gases differs at different wavelengths, since only certain energy levels can be emitted or absorbed, and may be derived from quantum mechanics. Under typical combustion conditions, the maximum emissive power is in the wavelength range of 1–6 μm, or wavenumbers 1,667–10,000 cm^{-1}, which is referred to as thermal radiation [2]. Both water vapor and carbon dioxide are triatomic molecules with many rotational and vibrational energy levels within this spectral range and, therefore, a vast number of possible vibrational-rotational transitions, corresponding to spectral lines, are available and should be considered appropriately when modeling radiative heat transfer. Both gases can have a strong impact on the radiative heat transfer in a furnace, as they are present at relatively high concentrations. An example of the spectral black-body intensity at 1400°C, representing combustion temperature, is shown in Figure 1, together with the spectral intensity of a gas mixture of carbon dioxide (CO_2) and water (H_2O), at a concentration of 10% for both gases, also at 1400°C. The difference between the black body and gas intensity varies with the wavenumber. The peaks indicate where radiation is absorbed and emitted by the gases, and as is indicated, gases absorb and emit differently at different wavenumbers. Here, the spectral intensities were calculated using a statistical-narrow-band model with a bandwidth of 25 cm^{-1}.

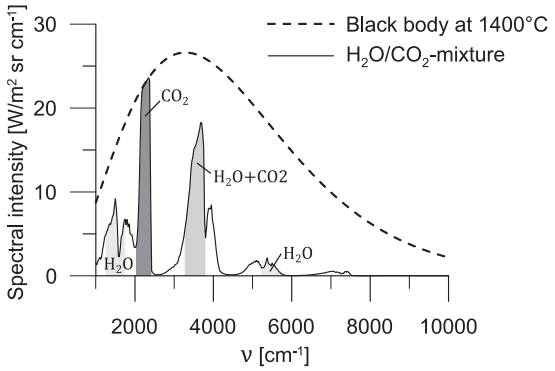

Figure 1. Example of the spectral intensities of a black body and a gas mixture of water steam (H_2O) and carbon dioxide (CO_2), at a concentration of 10% for both gases, all at 1400°C. Selected peaks represented by the gaseous water and carbon dioxide are indicated.

The more abundant nitrogen, but also oxygen, are diatomic molecules without an electrical dipole. Therefore, they have fewer motional degrees of freedom and far fewer available energy levels in the wavelength range of interest, and their impacts on the radiative heat transfer is usually negligible [2]. Therefore, from the radiative heat transfer perspective in a furnace, water vapor and carbon dioxide are usually the only two gases considered.

Particles

During the combustion of a solid fuel, particles are naturally present in the flame. The fuel particles lose mass as a result of drying, devolatilization and char combustion, and undergo changes in size and composition upon exposure to the hot surrounding gas. Ash and soot particles may form, depending on the fuel composition and combustion conditions. In similarity to gases, particles emit and absorb radiation, although they can be characterized as broad-band emitters (in contrast to gases), meaning that they emit and absorb radiation continuously across most of the spectrum. The radiation exchange is dependent on the surfaces of the particles, such that smaller particles can potentially and temporarily radiate more heat per mass than larger particles. Furthermore, particles may also scatter radiation, as they are much larger than the gas molecules and possibly larger than the infrared wavelengths. Scattering of incident radiation occurs at the particle due to three reasons in accordance to Figure 2: (i) diffraction, the path of the ray is altered at an angle θ without colliding with the particle; (ii) reflection; or (iii) refraction, whereby the ray penetrates the particle. Thus, the particle size distribution affects the emission, absorption and scattering properties in the furnace. Fuel, char, ash, and soot particles can potentially be present throughout the furnace.

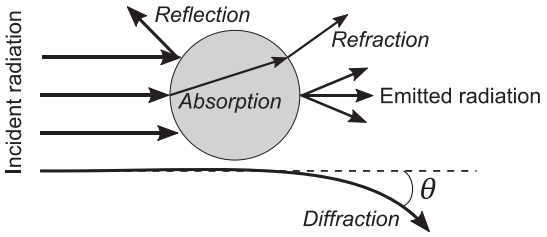

Figure 2. Particle scattering of incident radiation due to reflection, refraction and diffraction. Incident radiation may also be absorbed and the particle itself emits radiation.

In a suspension-fired solid-fuel flame, fuel and char particles are the most abundant particles, while ash particles mainly appear in the post-flame and recirculation zones. The different

particle types have different radiative properties, and flame radiation in pulverized coal-fired and cylindrical furnaces has been examined in several studies. Different parameters, such as the scattering efficiencies of the different particle types, concentrations, and size distributions [3], as well as the temperature distribution, extinction coefficients, and single-scattering albedo [4], have been examined. The importance of using separate temperatures for gases and particles has also been evaluated [5]. In these studies, it was found that coal and char particles were the main contributors to the heat flux at the wall, and the importance of scattering was underlined [3]. It was concluded that for predicting the radiative heat transfer in a coal-fueled furnace, a thorough understanding of the temperature and particle concentration distributions was more critical than having detailed information regarding the gas concentration or the particle index of refraction [5]. Therefore, it is desirable to determine both the temperature and particle concentration as accurately as possible when studying flames.

When gaseous or liquid fuels are used, while the particles are not fed to a burner, but as for a solid fuel, soot particles may form and be suspended in the flame, indicating incomplete combustion. The soot particles are small, with typical primary particle sizes of 20–50 nm in diameter, but may aggregate to several hundred nanometers, and is an important contributor to heat radiation, given that they both emit and absorb radiation [6]. Soot is generated by the pyrolysis of fuel in high-temperature regions of the furnace with lean oxygen concentrations [7]. The particles form, age, and combust in the flame through the phases of nucleation, surface growth, particle coagulation, and oxidation [8]. The transition from gaseous compounds to solid soot particles is, however, poorly understood, although polycyclic aromatic hydrocarbons (PAHs) have been demonstrated to play an important role in the soot nucleation step [9]. PAHs are considered to be formed from the collisions of smaller aromatic and alkyl compounds during the pyrolysis of hydrocarbons [10]. The absorption to the PAH of different compounds from the surrounding gas phase will lead to the formation of the smallest soot particle [10], [11]. Once formed, the particle will continue to grow and increase in size due to ongoing heterogeneous reactions, absorption, and coagulation with smaller soot particles following collisions [12]. Thus, soot formation in a flame is not only chemically controlled but is also dependent upon the surroundings, and it has been shown to be affected also by dilution and temperature [13]. Since large temperature gradients are present in flames, thermophoresis could have an impact on the trajectories of the soot particles and, possibly on the particle growth [14]. As the particles are eventually transported to more oxygen-rich regions of the flame, they will start to be oxidized and combusted. Therefore, the amount of soot that is emitted from a furnace reflects a competition between the formation and the destruction, via oxidation, of soot particles [10]. The radiative properties of soot particles have been examined in several studies (e.g., [15]–[18]), and it has been shown that the scattering caused by the soot particles is negligible due to their small size, and that the particle properties can be calculated using the Rayleigh theory [2]. Others have studied the contribution of the soot particles to radiative heat transfer. For instance, Mehta et al. [19] studied laboratory-scale, turbulent jet flames and concluded that as much as 70% of the emitted flame radiation was due to soot particles. However, any unexpected formation of soot can affect the performance of the furnace, with the consequence of increased operational cost. For these reasons, it is of interest to analyze the soot present in a furnace and to model the radiative heat transfer in the process.

1.1.2 Co-firing

In this work, co-firing refers to the combustion of treated and grounded wood together with coal. While coal is a fossil fuel, increasing the concentration of carbon dioxide in the atmosphere when combusted, wood is a renewable biomass. Thus, as long as the trees are replanted, the atmospheric concentration of carbon dioxide will not increase due to combustion of the wood. Typically, biomass from wood contains higher levels of volatile compounds and lower levels of fixed carbon and ash, and has a lower heating value than coal fuels [20]. The bulk density of the biomass is also lower than that of coal, which may result in drastically increased volume flows of the fuel, changing to co-firing combustion [21]. Moreover, the mixing of solid fuels can cause the particle distribution to vary over a broad size range. An example of a particle sample from a co-firing flame, using untreated wood biomass and coal, clearly shows the broad range of particle sizes, as depicted in Figure 3. Potential difficulties linked to co-firing include problems with fuel availability and supply, particle burnout, corrosion [21], [22], and fuel feeding to the burner, in that long wood fibers can cause fluctuations in the fuel feed [23]. Other concerns may be potential changes to the heat transfer within the furnace, resulting from the altered particle composition and size distribution.

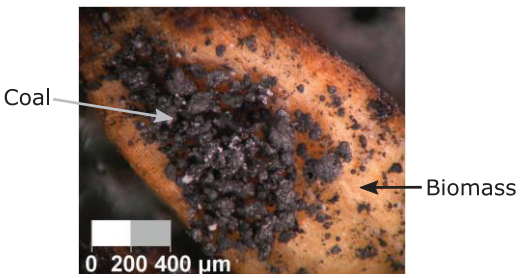

Figure 3. Example of particles gathered from a co-firing flame. The black coal particles are clearly much smaller than the white biomass particles on which they are positioned.

1.1.3 Oxy-Fuel and Oxygen-Enriched Air Combustion

During the combustion of hydrocarbon fuels, carbon dioxide will always form and be emitted to the atmosphere, unless the gas is captured and stored, using so-called 'carbon capture and storage' (CCS). CCS has been successfully demonstrated in, for example, the Norwegian Sleipner project, involving offshore, undersea saline formations into which carbon dioxide has been injected since 1996 [24]. To minimize the gas volume, the carbon dioxide should be separated from other flue gases before storage. One way to achieve this could be to apply oxy-fuel combustion, in which the oxidizer is changed from air to either pure oxygen or to recirculated flue gas, with the addition of pure oxygen [25]. Potentially, only water vapor and carbon dioxide would form from a pure fuel, and these could be easily separated through condensation. Thus, applying oxy-fuel combustion would simplify the flue gas separation and, for example, also eliminate the formation of thermal NO_x. Other changes to the combustion conditions will also occur, such as a lowered flame temperature if flue gases are recirculated, due to the higher specific heat capacity of the carbon dioxide. However, if the oxygen concentration is increased to a level above 21%, as in air, the combustion temperature will increase concomitantly [26]. Furthermore, the radiation conditions in the furnace will change as transparent nitrogen is substituted for absorbing and emitting carbon dioxide and water vapor, and the formation of soot particles will change in the gaseous flames. Beltrame et al. [8]

have shown an increase in soot formation when increasing the oxygen concentration in the oxidizer from 21% to 100%, for a counterflow diffusion flame. Several other researchers have found that a higher oxygen concertation causes an increase in soot formation until a certain oxygen concentration is reached, after which the abundance of soot particles decreases (see [27]–[31]). As the oxygen concentration is increased, the maximum temperature is increased, which enhances soot formation, although the flame volume becomes compressed, and the residence time in the high-temperature region is reduced, thereby inhibiting soot formation. In addition, the more abundant oxygen will oxidize the formed soot particles [30].

When operating a furnace in oxy-fuel mode with flue gas recirculation, a high concentration of carbon dioxide in the furnace is achieved. Adding carbon dioxide to the oxidizer suppresses soot formation, as observed by Guo et al. [7], who attributed this to thermal and direct chemical interaction effects, as well as to some dilution effect. The drop in flame temperature results in a decreased pyrolysis rate and decreased formation of important compounds during soot formation, such as C_2H_2 and PAHs [7]. The temperature effect was tested by Oh and Shin [32] by exchanging the carbon dioxide with a mixture of carbon dioxide and argon, so that the same heat capacity was achieved for the gas as if using only air and the same oxygen concentration. The reactions implicated in the decrease in soot formation from the additional carbon dioxide were studied by Liu et al. [33] and found to proceed according to R1 and R2, enhancing the oxidative attack of soot precursors:

$$CO_2 + H \leftrightarrow CO + OH \qquad \text{R1}$$

$$CO_2 + CH \rightarrow CO + HCO \qquad \text{R2}$$

As soot particles are effective radiative heat emitters, it could be argued that combustion with an increased concentration of oxygen in air, so-called ‘oxygen-enriched combustion’, is desirable to promote soot formation and enhance the radiative heat transfer in furnaces. Higher intermediate concentrations of soot along with a compressed furnace volume can be achieved, as the total volume of air required, followed by the emitted gases from the combustion processes, is reduced, together with an increase in flame stability and this could eventually lead to fuel savings [27], [29]. Different industrial processes have already been successfully operated using oxygen-enriched air, including boilers, incinerators and glass furnaces [34]. Oxygen-enriched combustion can be used effectively to replace oxy-fuel combustion if a strong convective heat transfer is required, as well as an increased luminosity, as is the case in aluminum melting [28], [29]. However, since the soot particles have been shown to be detrimental to health as they are carcinogenic and associated with respiratory illnesses [35], [36], it is important that the particles are eliminated in the furnace system.

1.2 The Rotary Kiln Process

Already in 1885, Frederick Ransome patented the first example of what is today known as a rotary kiln, and it was introduced to the cement industry [1]. Since then, rotary kilns have been developed and are commonly used in several industries, such as pulp and paper, cement, and iron ore pelletizing plants [37]. The rotary kilns are large, cylindrical, tilting, and slowly rotating furnaces, and the unit operation of the kiln involves mainly heat treatment of a solid bed material that passes from the higher to the lower end. The heat is supplied either directly or indirectly,

depending on the process heat requirements. In directly heated rotary kilns, the heat is mainly supplied by radiation from a large luminous flame along the kiln axis, with the burner positioned at the lower end of the rotary kiln [38], [39]. One problem associated with large industrial rotary kilns is the continuous and substantial emissions of carbon dioxide generated from the combustion, which are currently and frequently fueled by fossil coal [1]. The choice of fuel is mainly dictated by the availability, composition, cost, and high heating value of the fuel. To reduce the impact on global warming from industries, emissions of greenhouse gases from the stationary industrial sector need to be drastically reduced. In the case of rotary kilns, one way to achieve this might be to switch to less-carbon-intensive fuels. However, this might affect the heat transfer conditions in the rotary kiln, thereby compromising the quality of the product. The heat treatment of the bed material and the heat transfer that occur within the kiln are complex, since they not only include convective, conductive and radiative heat transfers, but also heat that is transferred in the angular and axial directions as the wall rotates and the bed mixes, as illustrated in Figure 4. The bed material close to the wall is transported from a lower position in a cross-section of the bed, until the point at which the bed falls over and is mixed into the main bulk of the bed. The bed can, therefore, be divided into two layers, a surface and a bottom layer, which are moving in opposite directions. In addition, heat may be released or consumed within the bed material as the result of chemical reactions, and heat losses occur at the outer wall of the kiln wall due to convection and radiation.

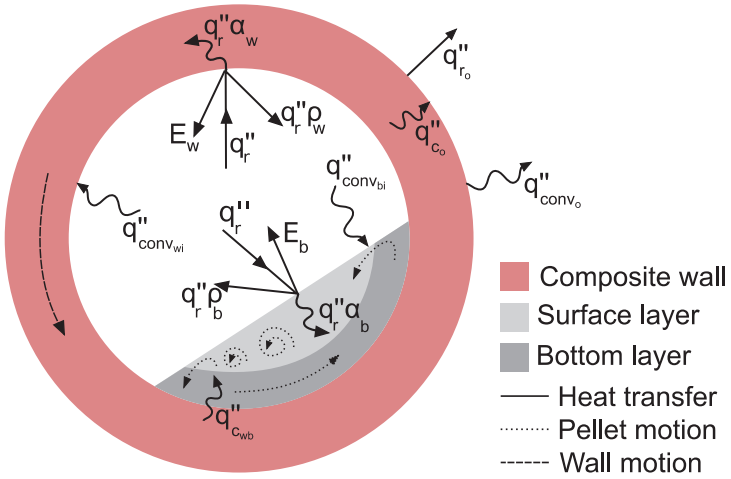

Figure 4. Cross-section of a rotary kiln with bed material present. Different possible heat transfer mechanisms involving convection (q''_{conv}), conduction (q''_c), and radiation (q''_r, E) at the kiln wall (w) and bed (b) are indicated. The incident radiative heat flux may be absorbed (α) or reflected (ρ) at a surface. The movement and mixing of the bed material due to the rotating kiln wall are shown for a considered surface and bottom layer of the bed.

However, radiation dominates the overall heat transfer in the kiln [1]. Thermal radiation from the flame is anticipated to be dominated by hot particles, mainly char, but also ash and soot particles, since a solid fuel is used. The radiative heat transfer from solid fuel flames in cylindrical furnaces has, as already mentioned, been studied and modeled earlier [3]–[5], albeit under more conventional combustion conditions. There is currently a lack of quantitative knowledge of the heat transfer conditions in rotary kilns using any fuel, mainly due to the rotation of the kiln, which complicates in-flame measurements. Therefore, it is of interest to study how well the radiative heat transfer and the heat treatment of the bed can be modeled in

this process. Some studies of the heat transfer between the wall and bed material have been conducted previously [39]–[41], as well as of the convective heat transfer [41], [42]. Earlier modeling studies of the radiative heat transfer in a rotary kiln [43]–[46] focused on the gases in the freeboard and the surfaces of the kiln, neglecting the particles present in flame or freeboard. In this work, particles present in the flame and freeboard gas are considered, and measurement data from a pilot-scale test furnace are used for modeling the radiative heat transfer.

While there are many applications of rotary kilns, this work focuses mainly on the rotary kilns used in the iron ore industry. To achieve a good iron ore quality and to facilitate transportation, the mined, crushed, and treated ore is commonly processed into a pelletized form. Figure 5 shows a schematic of a commonly used process for iron ore pelletization, the grate-kiln process, which is used by the Swedish mining company Luossavaara-Kiirunavaara Aktiebolag (LKAB). Raw iron ore pellets are fed onto a travelling grate, where they are partially dried and oxidized from magnetite to hematite using hot air and flue gases that pass through the bed and grate. From the grate, the iron ore pellets enter the more than 30-m-long and 5-m-wide (inner diameter) rotary kiln. As the pellets slide towards the lower end, they are further heated, oxidized, and sintered. Once they exit the rotary kiln, the pellets drop down into a rotating cooler. Ambient air is used in the four cooler zones (C1–C4). To exploit the heat from the pellets, the air that exits the cooler is transported to the grate zones (G2–G4) and kiln (Figure 5). The air leaving the first cooler zone, C1, is directed directly to the kiln, where it acts as preheated secondary air with a temperature in the range of 1050–1100°C. In comparison to more typical combustion processes, the volumetric flow of the secondary air is large to promote pellet oxidation within the kiln, with an oxygen content of about 16% in the flue gas. The flue gas that exits the kiln is directed through the pellet bed in zone G1. A more detailed description of a typical grate-kiln process can be found elsewhere [37].

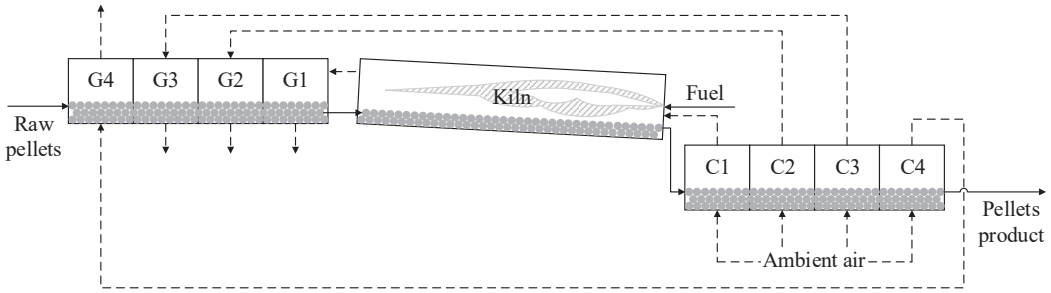

Figure 5. Schematic of the grate-kiln process used by LKAB. Raw iron ore pellets enter the grate at G4 and pass through the rotary kiln. The finished product exits the cooler section at C4.

Worldwide, approximately 2,500 million tons of iron ore were mined in 2018, where Australia, Brazil, and China being the three largest producers of iron ore according to the 2019 USGS Mineral Commodity Summaries [47]. The primary user of iron ore is the steel industry, and the combined carbon dioxide emissions from the iron and steel industries represented approximately 5.7% of total global emissions (30% of the industrial sector) in 2016 [48]. LKAB's carbon dioxide emissions accounted for about 1.3% of Sweden's total emissions (4% of the industrial sector) in 2018 [49].

1.3 Aims and Objective

The overall objective of this thesis is to improve the capability for characterization of radiative heat transfer in suspension-fired furnaces to support a growing demand for detailed modeling capacity of such units. Accurate and efficient modeling is crucial, for example, in design to assist a rapid transition to low-carbon technologies or during operation to be able to handle increased flexibility and operational demands. To validate such models, high quality measurement data are required, gathered during experiments intended to imitate industrial processes.

More specifically, this work assesses one application of radiative heat transfer in the heat treatment of iron ore pellets in a rotary kiln (Papers I–III) and one phenomenon of importance for radiative heat transfer in combustion, namely the influence of soot particles and their radiative properties (Papers IV and V).

The specific aims of this thesis are:

- To examine the respective contributions of the gases and particles to the total radiative heat transfer in flames in the rotary kiln process (Paper I);
- To examine the effect on radiative heat transfer of flames that use co-firing with different biomasses (Paper I);
- To develop a modeling tool to study the radiative heat transfer in detail and to examine the heat treatment of the bed material in rotary kilns (Papers II and III);
- To evaluate techniques for measuring the soot volume fraction in gaseous flames (Papers IV and V); and
- To determine the effects of intermediate soot formation and radiative heat transfer properties of soot particles under various oxygen concentrations and combustion conditions (Papers IV and V)

2. Previous Work and Progress Made

Owing to the significant contributions made by various research groups, such as Hottel & Sarofim [50], Siegel & Howell [51], Özisik [52], and Modest [2], research on radiative heat transfer in suspension-fired systems has advanced rapidly since the 1960's. The work presented in this thesis includes measurements and modeling of the radiative heat transfer in flames that employs hydrocarbon fuels, an area in which our research group has been active for many years. In-flame measurement data have been gathered during numerous measurement campaigns that were conducted to examine various combustion conditions, including pulverized coal-firing, co-firing, gaseous and oxy-fuel flames, using different measurement methodologies and modeling approaches for different applications, including oxy-fuel flames and rotary kilns [23], [53]–[55]. Based on the work of Modest [2], we have constructed models that allows studies of flame radiation in cylindrical and semi-cylindrical enclosures, in which both the gases and particles are considered. By validating the models with measurement data, they can be useful tools for predicting the radiative heat transfer for various furnaces and combustion conditions.

Figure 6 shows an overview of the previous and relevant studies (including the work included in this thesis) conducted by our research group. To reveal the path followed towards this thesis, previous studies (before 2014) are briefly presented in this chapter, along with the measurement campaigns, the scope of the papers included in the thesis and what models that were used.

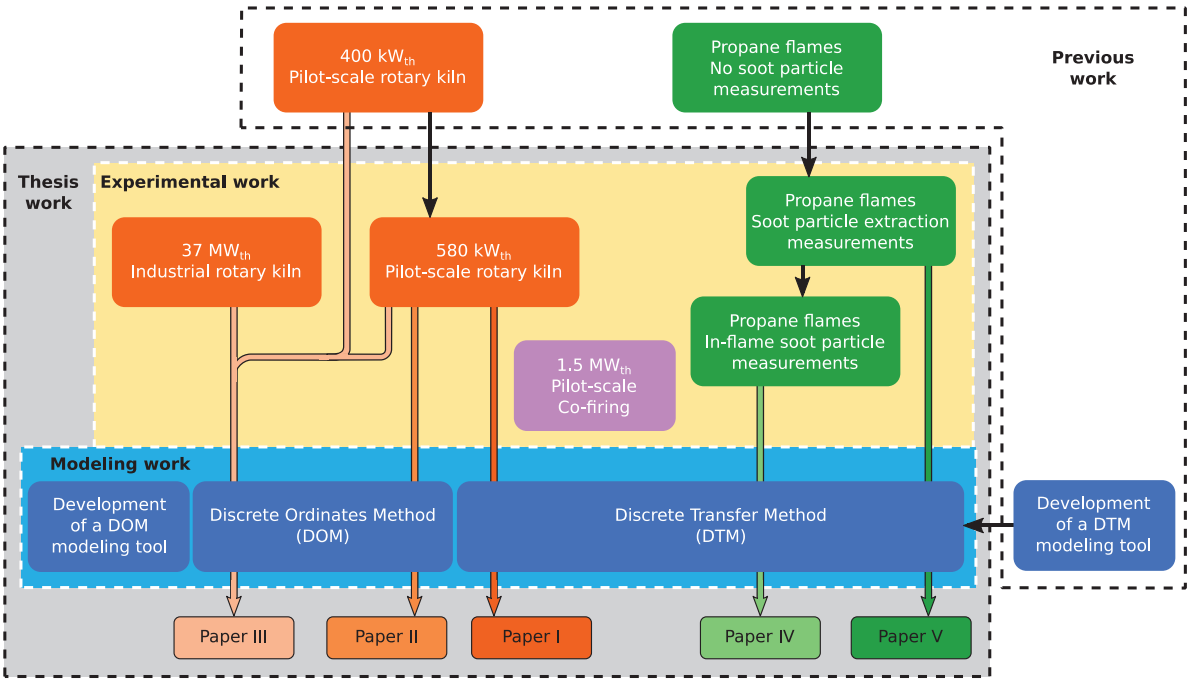

Figure 6. Overview of the different pathways for the included Papers I–V, indicated with colored arrows. The connections between the present thesis work (gray area) and previous work (white area) on rotary kilns (orange), propane flames (green), and radiative heat transfer modeling are indicated with black arrows. Additional measurements not presented in any of the papers is also included (purple). The thesis includes both experimental work (yellow area) and modeling work (blue area).

The campaigns of most interest are those that were conducted in a rotary kiln, a down-scaled rotary kiln test furnace, and a vertical cylindrical furnace. In addition, measurements that were made in an industrial rotary kiln and a measurement campaign that was performed in a cuboid furnace (1.5 MW_{th}) are included and briefly described here, but not in any of the papers. For further details of the different radiative heat transfer models, measurement equipment items and furnaces, please see Chapters 3, 4 and 5, respectively. Selected results from the experimental measurement campaigns and the modeling conducted within this thesis work are presented and discussed in Chapter 6.

2.1 Rotary Kilns

Two measurement campaigns have been conducted in a cylindrical, pilot-scale test furnace, which was designed to resemble a full-scale industrial rotary kiln, in collaboration with LKAB. The fuel flexibility of the grate-kiln process was studied by examining different fuels under combustion conditions similar to those found in an industrial rotary kiln used for iron ore pelletizing. The aim was also to study the radiative heat transfer properties within the test furnace and, thereby, gain insight of the properties within an industrial rotary kiln. Temperature data and operation parameters were gathered at a full-scale rotary kiln and used for a first validation attempt of the model.

2.1.1 Pilot-Scale Rotary Kiln

A campaign was conducted previously of this thesis in 2013 by Bäckström et al. [23], who studied eleven fuels or fuel combinations. A carbon-rich coal, which is used daily in LKAB's full-scale rotary kilns, was used as a reference coal (RC) during the campaign. Studied alternative fossil fuels for the process included a second coal (SC), similar to the RC in terms of both chemical composition and size distribution, heavy fuel oil and natural gas. The heavy fuel oil is used occasionally and during the start-up phase of the full-scale process. The co-firing cases were all examined with the RC using co-firing burners. Three biomasses were studied separately, each being tested at concentrations of 10% and 30%, based on the fuels' lower heating values, while maintaining the total heat load to the burner. The three biomasses used were: (i) biomass A (BA), comprising wood treated with steam explosion; (ii) biomass B (BB), comprising pelletized and ground wood; and (iii) biomass C (BC), consisting of torrefied biomass. In an additional co-firing case, biomass A was premixed (PM) with the RC and tested in the same coal burner used for pure coal.

Measurements of the temperature, gas composition, and radiative intensity were conducted along the furnace axis, together with downstream particle extraction. Figure 7 shows the measured radiative intensities along the furnace diameter for the fossil fuels. The data were obtained at a measurement port positioned 700-mm downstream of the burner, measured using a narrow angle radiometer (NAR) probe. The NAR entered the furnace at the 0-mm position and was traversed along the furnace diameter. At the port entrance, high radiative intensities were measured owing to the high concentrations of particles and the high temperatures in the detectors line-of-sight. As the probe was traversed closer to the center, the radiative intensity decreased in line with the total number of particles. At the opposite wall, at the 800-mm position, the radiative intensity came close to zero due to the presence of a cold background, in

the shape of a quartz window in the furnace wall. Comparing the two coals, significant differences were observed, even though they had appeared to be very similar in the fuel analysis (Figure 7a), which stresses the difficulty of predicting the flame radiation without performing experiments. The differences between the coals was difficult to explain due to a lack of flame data. This was mainly due to problems associated with particles clogging the suction pyrometer, which prevented the achievement of a high suction velocity and, therefore, accurate measurements of the flame temperatures. Furthermore, particle extraction was performed downstream of all the other measurements, which meant that particle data for positions close to the burner were lacking. The oil and gas flames were observed to be shorter than any of the solid fuel flames, as reflected by their low radiative intensity values (Figure 7b). This indicates that the heat-load profile of the pellets in the full-scale rotary kiln would be rather different than that obtained using the RC.

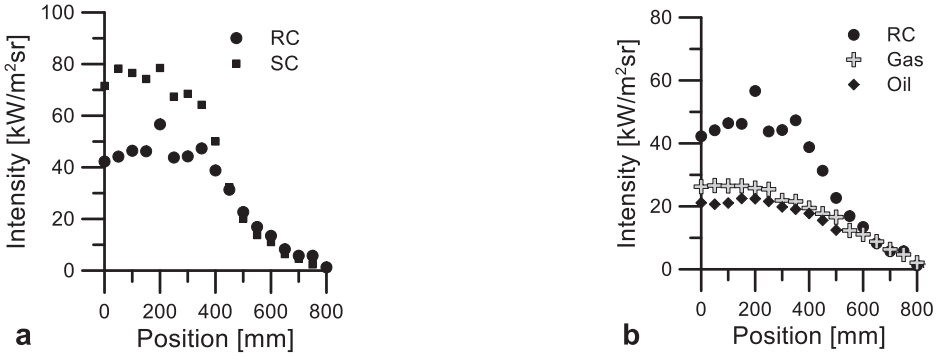

Figure 7. Radiative intensities measured along the furnace diameter, 700-mm downstream of the burner, during the measurement campaign conducted in 2013 by Bäckström et al. [23] for two coals (RC and SC) and gas and oil flames.

Figure 8 shows the measured radiative intensities (using the NAR) for the RC and the co-firing experiments studied. The PM case and the co-firing case with 30% BA showed slightly lower radiative intensities than the RC case (Figure 8a), while the other co-firing cases (BB and BC) appeared to have radiative intensity levels similar to that of the RC at the second measurement port (Figure 8, b and c, respectively). All the co-firing flames appeared to be shorter than the coal-fired flames.

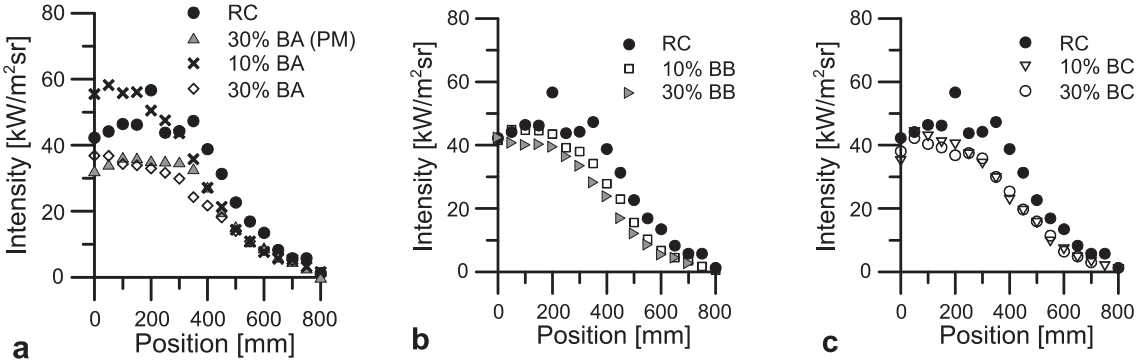

Figure 8. Radiative intensities measured along the furnace diameter, 700-mm downstream of the burner, during the measurement campaign conducted in 2013 by Bäckström et al. [23] for co-firing of RC with three biomasses (BA, BB, BC), and a co-firing flame where RC was premixed with BA (PM). The percentages shown correspond to the proportions of biomass in the co-firing cases.

Detailed radiation modeling was performed using a discrete transfer model for the different cases, and the model appeared to underestimate the radiative intensity in comparison to measurements. This was probably due to the problems associated with measuring an accurate flame temperature and underestimated particle concentrations. It was found, however, that the radiation from the present particles dominated the total flame radiation [23]. From the modeling work of the radiative intensity, it was concluded that improved measurements of temperature and particle concentrations were needed to more accurately estimate the radiative heat transfer.

In 2015, a second measurement campaign was conducted as a part of this thesis work. The same test furnace was used but incorporating some modifications to ensure better process control. A new burner was installed to achieve more stable conditions with respect to biomass feeding and, thereby, improve the quality of the experiments. Additional measurement ports were installed along the furnace axis to enable an increased access for measurements in the flame. The thermal input to the burner was increased from 400 kW_{th} to 580 kW_{th}, and the furnace diameter was decreased from 800 mm to 650 mm. As in the previous campaign, measurements of the temperature, gas composition, and radiative intensity were conducted along the furnace axis. However, extra care was taken to achieve and sustain a sufficient suction velocity using a new suction pyrometer and ejector system and the temperature measurements were considered to be superior to those in the earlier campaign. The sampling of particles was also improved, as particles were sampled within the flame and closer to the burner and additional measurements and measurement techniques were applied, including radiative heat flux measurements, Fourier Transform Infrared Spectroscopy (FTIR) for gas analysis, and an infrared camera for temperature estimations. Moreover, during the second campaign, greater emphasis was placed on co-firing flames, to examine the differences in temperature conditions and flame structure as compared to a coal flame. Furthermore, the overall test matrix was increased with respect to the numbers of fuels and fuel combinations, testing three additional coal fuels. The same RC was used, and co-firing of BA and BB was once again studied, using 30% biomass, but in contrast to the coal tests, the burner configuration was altered by changing fuel registers and by moving the burner further into the furnace so that it resembled the rotary kiln used by LKAB at another iron ore pelletizing plant. The measurement data gathered for the co-firing cases is presented in Appendix B.

In Paper I, the co-firing flames from the latter campaign were extensively studied and the radiative intensity was modeled using an axisymmetric discrete transfer model, evaluating the possibility of substituting a portion of the fossil fuel for renewable biomass. The radiative heat transfer is quantified in the process, and the separate contributions from the hot gases and particles to the flame radiation are examined. From the modeling results, it appears that the model estimates the radiative heat transfer more accurately for the different flames in the latter campaign, in comparison to the earlier campaign. It should, however, be noted that while much effort was put into ensuring high-quality measurements, at some measurement positions, problems were encountered with condensing tars when extracting the particles from the co-firing flames, and as a consequence some of the data had to be discarded. This lack of data somewhat limited the modeling work and highlights a problem that persists and should be addressed in future measurement campaigns.

To better study the radiative heat transfer along the axis of the pilot-scale furnace, a non-axisymmetric modeling tool that applies a discrete ordinates method has been developed within this thesis; the equations employed in this tool are further described in Chapter 3. Measurement data for the RC case from the latter campaign are used together with the developed model in Paper II to examine the effect on the incident heat flux to the wall when varying the radiative properties of the wall and flame. In an attempt to better imitate a rotary kiln, a stationary bed material is added to the furnace and the effect on the radiative heat flux is examined.

2.1.2 Industrial Rotary Kiln

From the measurement campaigns described above, valuable data regarding temperature, gas composition, radiative intensity, and radiative heat flux were gathered. This information is necessary to achieve an increased understanding of the heat transfer occurring within the rotary kiln. It would, however, be desirable to measure also these parameters in a rotary kiln at industrial scale, but as already stated, most of these parameters are very difficult to measure in a full-scale rotary kiln. Modeling of the heat transfer within the kiln can therefore be helpful to gain better understanding of the heat treatment of the bed material. It was, however, possible to use an infrared camera to study the temperatures at the rotary kiln during real process conditions. The outer wall of the rotary kiln was studied while standing next to the kiln and the inner wall and bed temperatures could be assessed, as well as the bed angle and flame occurrence through a small hatch, positioned close to the burner (Figure 9). Several other parameters of interest, such as the production rate and rotational speed, could be derived from the operational data.

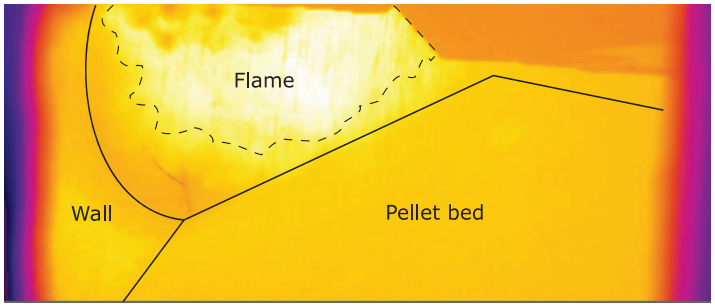

Figure 9. Temperature conditions inside a rotary kiln used for iron ore pelletization, captured using an infrared camera. The approximate extents of the wall, bed, and flame are indicated.

Further development of the modeling tool applying the discrete ordinates method has been performed in this thesis to include the heat treatment of the bed material in a rotary kiln, also including conductive and convective heat transfers (see Section 3.3). Together with the measurement data from the two campaigns involving the pilot-scale rotary kiln described above, the bed heat treatment for an oil flame (data from 2013) and a coal flame (RC data from 2015) were modeled for a full-scale rotary kiln, which is the focus of Paper III. The product temperature from the model is compared to measurement data, and the model is further used to examine the heat transfer contributions from conduction, convection and radiation to the bed material.

2.2 Heat Radiation from Soot Particles

In 2007, Andersson et al. [26] studied propane flames in the Chalmers 100-kW_{th} oxy-fuel test rig, equipped with a down-fired swirl-burner. The radiative properties of three 80-kW_{th} flames were studied, with one flame using air as the oxidant, and two flames operated in an oxy-fuel mode with recirculated flue gases and oxygen concentrations of 21% and 27%, respectively. For all three cases, the same stoichiometry was used ($\lambda = 1.15$), achieved by varying the recycling rate of the dry flue gas and the addition of a corresponding amount of oxygen. While measurements of the temperature, total radiative intensity, and gas composition were performed, no direct measurements of the soot content were conducted. It was, however, visually observed that the soot content initially decreased along with the flame temperature and the measured radiative intensity when the furnace was changed from operating with air (Figure 10a) to operating with oxy-fuel at 21% oxygen (Figure 10b). However, with a further increase of the oxygen content, soot formation again visually increased along with the measured radiative intensity (Figure 10c). The radiative intensity was modeled using the discrete transfer model, considering the gas temperature and the concentrations of water steam and carbon dioxide, but no soot particles. By comparing the measured and modeled radiative intensities, the soot particles could be identified as making up for the difference between the two values (see Figure 10c), and it became obvious that the present soot particles had a significant contribution to the total heat transfer.

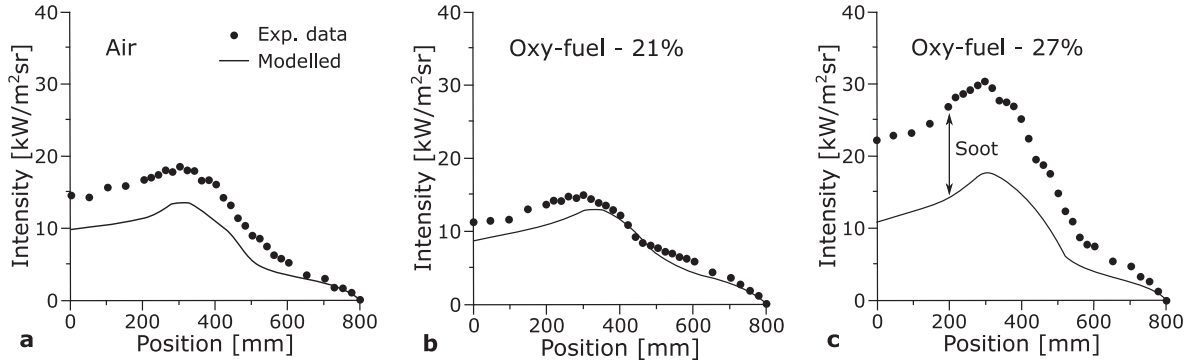

Figure 10. Measured and modeled radiative intensities along the furnace diameter for a flame using air as the oxidant (**a**) and when operating the furnace in oxy-fuel mode with 21% (**b**) and 27% (**c**) oxygen, respectively [26].

Subsequently, due to the soot particles evident impact on the radiative heat transfer, it was desirable to measure the soot contents and examine the radiative properties of different propane flames. At the start of this thesis work in 2014, Bäckström et al. [56] used the same test facility to estimate the soot volume fraction and study the optical properties of the soot. The 80-kW_{th} air-propane flame was studied, and to produce soot particles, the primary air flow to the burner was closed using a valve, which resulted in a different and less-effective mixing, which in turn caused the formation of soot particles. Gas samples were extracted to measure the soot volume fraction using a Scanning Mobility Particle Sizer (SMPS), while the optical properties of the soot particles were simultaneously measured with a Photo-Acoustic Soot Spectrometer (PASS-3) instrument. In Paper V, the obtained optical properties of the soot particles are compared to earlier literature findings and by using the measured soot volume fraction, the radiative intensity is modeled for the propane flames using the discrete transfer model.

However, during the gas extraction, before the soot volume fraction could be measured, present particles could break or new could form. It would therefore be desirable to measure the soot volume fraction non-intrusively and within the flame. In 2016, the same furnace was used once more with the same thermal input of propane to the burner, to measure the soot volume fraction using optical and non-intrusive methods. This campaign was conducted in collaboration with the Combustion Physics Department at Lund University of Technology and a diode laser was used with a Laser-Induced Incandescence (LII) system. With this optical technique, a laser sheet is shaped and focused in the central part of the furnace, and it was possible to capture 2D images of the soot volume fraction along the furnace diameter, with a considerably increased spatial and temporal resolution, using a CCD camera. However, LII has mainly been used at flames of smaller scales [28], [57], causing some extra uncertainties at the studied scale, related to the laser sheet thickness. During this campaign, it was also of interest to operate the combustion process so that high intermediate concentrations, albeit with low final emissions, of soot were achieved, in order to enhance the efficiency of radiative heat transfer from the flame [27], [28]. This was tested by either varying the oxygen concentration in the oxidant by enriching air with oxygen or varying the oxygen concentration while operating the furnace in an oxy-fuel mode. A photo of the actual experimental set-up used is shown in Figure 11a and a schematic of the setup with an Nd:YAG-laser, a CCD-camera and the NAR is shown in Figure 11b.

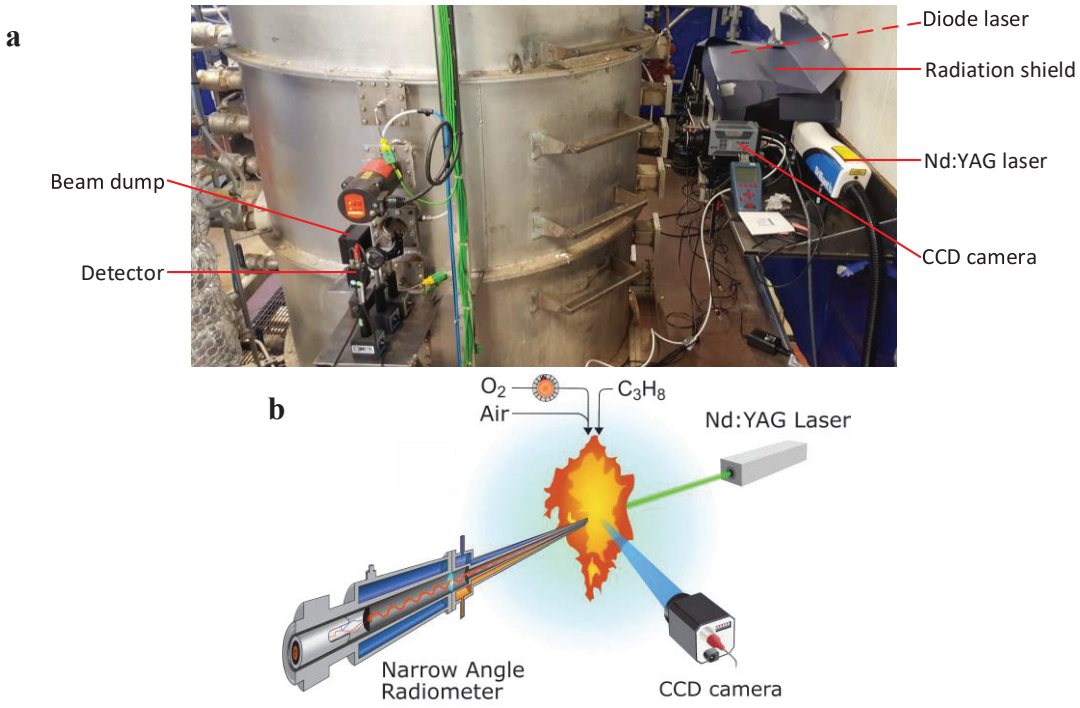

Figure 11. Experimental setup used in the 2016 campaign (Paper IV [58]). **a** Photograph showing the furnace and the measurement equipment, the diode laser is located beneath the radiation shield and the laser beams are directed through the flame onto the detector. **b** Schematic of the equipment setup.

The results from this campaign are presented in the publications of Gunnarsson et al. [58] (Paper IV) and Simonsson et al. [59] (Paper A). In Paper IV, the oxygen-enriched air flames are examined and the radiative intensity for the flames are modeled using the discrete transfer model. The gas and particle contributions to the total radiative intensities are examined. Paper A examines the oxy-fuel flames and more thoroughly describes the experimental setup.

2.3 Co-Firing in a 1.5 MW_{th} Furnace

The radiative heat transfer properties of co-fired flames were also examined during a measurement campaign conducted in a horizontal furnace with a quadratic cross-section, operated to imitate a 1.6-GW_{el} power plant. The furnace is located in Utah and is referred to as the L1500 multifuel furnace. The campaign was conducted in 2018 as a collaboration with the University of Utah and Brigham Young University. A coal flame and a co-firing flame of coal and torrefied biomass were studied. In the co-firing case, the biomass comprised 15% of the total fuel feed, based on a total heat input of 1.5 MW_{th}. The temperature, gas composition, radiative intensity, and radiative heat flux profiles were analyzed during the campaign.

3. Heat Transfer Modeling

To model the heat transfer in furnaces, radiative, convective and conductive heat transfers should be included, so as to describe accurately the total heat transfer. The largest portion of the total heat transfer is attributable to radiation in many furnaces [1] and is the main focus of this thesis, which is why most of the emphasis is placed on this heat transfer mechanism. However, if only the radiative heat transfer within a furnace is to be considered, calculating the heat transfer still remains complex. Several elements need to be considered, given that the different gases and particles present within the flame and furnace emit, absorb, and scatter radiation. This chapter presents the main equations used to model the radiative heat transfer in cylindrical and semi-cylindrical furnaces, how present gases and particles are treated, and how measurement data is introduced to the different models. A large part of this thesis focuses on rotary kilns in which a bed material is present that exchanges heat with the flame, the passing gas and the kiln walls. In the presence of such a bed, heat transfer through conduction and convection, as well as the heat that is transported with the mass of the bed or wall must be included. Such a modeling tool has been developed within the work of this thesis and the structure of the tool is presented here.

3.1 Radiative Heat Transfer

The radiative intensity tells us how much heat is being transferred along a set direction $\hat{s}$. The intensity change is described by the radiative transfer equation (RTE), as the sum of the contributions from emission, absorption, and scattering away from and in to $\hat{s}$. For a given wavenumber, ν, the RTE can be written as:

$$\frac{dI_\nu}{ds} = \kappa_\nu I_{b\nu} - (\kappa_\nu + \sigma_{s\nu})I_\nu + \frac{\sigma_{s\nu}}{4\pi}\int_0^{4\pi} I_\nu(\hat{s}_i)\Phi_\nu(\hat{s}_i,\hat{s})d\Omega_i \quad (1)$$

where κ and σ_s are the absorption and scattering coefficients, respectively, $\hat{s}_i$ is the direction of the intensity being scattered in the $\hat{s}$ direction, and $d\Omega_i$ is the solid angle of the ray in the $\hat{s}_i$ direction. The scattering phase function, Φ_ν, describes the probability that a ray from the $\hat{s}_i$ direction will be scattered in the $\hat{s}$ direction [2]. The absorption coefficient is dependent upon both the gases and particles present, while the scattering coefficient for thermal radiation is only related to the presence of particles.

3.1.1 Gas Radiation

If the medium, through which a ray of light travels, only consists of gases and there are no particles, the scattering may be neglected [2], thereby simplifying the RTE to:

$$\frac{dI_\nu}{ds} = \kappa_\nu I_{b\nu} - \kappa_\nu I_\nu = \kappa_\nu(I_{b\nu} - I_\nu) \quad (2)$$

As shown in Eqn. (2), the absorption coefficient is dependent upon the wavenumber (see also Figure 1), such that solving the RTE requires knowledge of the spectral properties of the gases. The RTE can be solved for each spectral line by performing line-by-line calculations. However, these calculations are computationally cumbersome, requiring very detailed knowledge of

every spectral line, and they cannot be reasonably applied to other than a limited group of simplified problems. If the system is instead very complex, as in, for example CFD models, a simpler gas model must be utilized, e.g., a global gray gas model for which a fixed absorption coefficient is used throughout the furnace. However, other approaches exist that are intermediate to these two extreme models in terms of the model complexity and accuracy, and how computationally demanding they are. Such models may still give valuable insights into the radiative heat transfer in furnaces and are suitable for many engineering problems. Two such examples are statistical narrow-band models and weighted-sum-of-gray-gases models.

Statistical-narrow-band model

The statistical-narrow-band model (SNBM) represents a detailed approach to estimating gas radiation. In the SNBM, actual absorption coefficients for each spectral line are replaced with the averaged values for narrow spectral bands, together with random spacing and the strengths of the spectral lines. To enable statistical treatment of the bands, the spectrum has to be divided into bands that are sufficiently wide to contain many lines, while being narrow enough to assume constant black-body radiation in the band [60]. Different probability functions have been developed, for example by Goody [61] and Malkmus [62]. To generate realistic representations of the varying line strengths, S_l, the probability density function presented by Malkmus, according to Eqn. (3), has been used in the present work, since it is recognized as the best model currently available for polyatomic molecules [2].

$$p(S_l) = \frac{1}{\bar{S}_l}\exp\left(-\frac{S_l}{\bar{S}_l}\right), \qquad 0 \le S_l < \infty \tag{3}$$

Using the Malkmus SNBM, Soufiani and Taine have calculated the temperature-dependent narrow band parameters of the mean line spacing, d_k, and the mean line-intensity to the typical line-spacing ratio, k_k, for H_2O, CO_2 and CO [63]. These were subsequently updated with additional parameters for CH_4 by Rivière and Soufiani [64]. The spectrally averaged transmissivity of a narrow band k with a bandwidth $\Delta\nu$ of 25 cm^{-1} is calculated for a gas (g) according to Eqn. (4).

$$\bar{\tau}_{\nu_k,g} = \exp\left[-\frac{2\gamma_g}{d_k}\left(\sqrt{1+\frac{Y_g P S k_k d_k}{\gamma_g}}-1\right)\right] \tag{4}$$

In this work, only water steam and carbon dioxide are considered. Using reference values of 296 K and 1 bar for the temperature and pressure, respectively, the mean line half-widths, γ_g, for these two gases are given as:

$$\gamma_{H_2O} = \frac{P}{P_{ref}}\left\{0.462 Y_{H_2O}\left(\frac{T_{ref}}{T}\right) + \left(\frac{T_{ref}}{T}\right)^{0.5}\left[0.079\left(1-Y_{CO_2}-Y_{O_2}\right)+0.106Y_{CO_2}+0.036Y_{O_2}\right]\right\} \tag{5}$$

$$\gamma_{CO_2} = \frac{P}{P_{ref}}\left(\frac{T_{ref}}{T}\right)^{0.7}\left\{0.07Y_{CO_2}+0.058\left(1-Y_{CO_2}-Y_{H_2O}\right)+0.1Y_{H_2O}\right\}$$

The total transmissivity, for all the present gases, may be calculated as the product of the transmissivity values of the separate gases:

$$\bar{\tau}_{\nu_k,tot} = \prod_g \bar{\tau}_{\nu_k,g} \tag{6}$$

In those cases in which the pathway is neither isothermal nor homogeneous, the Curtis-Godson [2], [65] approximation is used, whereby each inhomogeneous optical path is instead replaced with a hypothetical homogeneous path with the corresponding transmittance. The transmissivity along a path, S, is related to the absorption and scattering coefficients according to Eqn. (7). For a non-scattering gas, the scattering coefficient is equal to zero.

$$\tau_\nu = e^{-(\kappa_\nu + \sigma_{s\nu})S} \tag{7}$$

Weighted-sum-of-gray-gases model

A less-detailed, but still effective, approach to modeling the radiative properties of gases is to use the weighted-sum-of-gray-gases (WSGG) model. This model was first presented by Hottel and Sarofim [50] and considers the molar ratio of water steam to carbon dioxide. The gases in the furnace are represented by a mixture of a set number of gray gases. Each gray gas, j, has a fixed absorption coefficient that reflects the real gas ratio, such that each gray gas represents all the spectral regions with an absorption coefficient in a specific range and may be calculated according to Eqn. (8). The coefficients K1 and K2 are given in Table 1.

$$\kappa_j = \mathrm{K1}_j + \mathrm{K2}_j \frac{Y_{H_2O}}{Y_{CO_2}} \tag{8}$$

In the spectral regions in which the gases neither emit nor absorb, the radiation is represented by a so-called clear gas for which the absorption coefficient is set to zero, $\kappa_0 = 0$. Weights for each gas, a_j, are calculated, depending on the same molar ratio and the gas temperature $\left(T_{ref} = 1200\ K\right)$, corresponding to the fraction of the black-body radiation assigned to each gas. The weight of the clear gas, a_0, is set so that the sum of the weights is equal to 1.

$$\begin{gathered} a_j = \sum_i c_{j,i} \left(\frac{T}{T_{ref}}\right)^{i-1} \\ a_0 = 1 - \sum_{j=1}^{J} a_j \\ c_{j,i} = C1_{j,i} + C2_{j,i} \frac{Y_{H_2O}}{Y_{CO_2}} + C3_{j,i} \left(\frac{Y_{H_2O}}{Y_{CO_2}}\right)^2 \end{gathered} \tag{9}$$

The coefficients used in this work to calculate the absorption coefficients and the weights for the gray gases are listed in Table 1 for a modified WSGG model, derived from the work of Johansson et al. [60]. The modified version of the WSGG model was developed for molar ratios in the range of 0.125–2.0, temperatures in the range of 500 – 2500 K, and pressure path lengths in the range of 0.01–60.0 bar m, for a set of one clear and four gray gases.

Table 1. WSGG-model coefficients for each of the four gray gases, *j*, as derived from the work of Johansson et al. [60]

j	1	2	3	4
$K1_j$	0.055	0.88	10	135
$K2_j$	0.012	-0.021	-1.6	-35
$C1_{j,1}$	0.358	0.392	0.142	0.0798
$C1_{j,2}$	0.0731	-0.212	-0.0831	-0.0370
$C1_{j,3}$	-0.0466	0.0191	0.0148	0.0023
$C2_{j,1}$	-0.165	-0.291	0.348	0.0866
$C2_{j,2}$	-0.0554	0.644	-0.294	-0.106
$C2_{j,3}$	0.0930	-0.209	0.0662	0.0305
$C3_{j,1}$	0.0598	0.0784	-0.122	-0.0127
$C3_{j,2}$	0.0028	-0.197	0.118	0.0169
$C3_{j,3}$	-0.0256	0.0662	-0.0295	-0.0051

Neither the absorption coefficient nor the weights are dependent upon the pressure path length, although the total emissivity of the gases is.

$$\varepsilon = \sum_{j=0}^{J} a_j (1 - \exp(-\kappa_j PS(Y_{CO_2} + Y_{H_2O}))) \tag{10}$$

Using the WSGG model, the RTE in Eqn. (2) may be expressed as:

$$\frac{dI_j}{ds} = \kappa_j \left([a_j I_b] - I_j \right) \tag{11}$$

3.1.2 Particle Radiation

The particles present in the furnace not only emit and absorb radiation, but they may also scatter radiation. Thus, the radiative properties of particles must be modeled in an appropriate way. For an interacting ray of light traveling through a cloud of spherical particles with radius *a,* the radiative properties are given by three dimension-less parameters: (i) the complex index of refraction; (ii) a size parameter; and (iii) the clearance-to-wavelength ratio*,* as shown in order in Eqn. (12).

$$m_\lambda = n_\lambda - ik_\lambda$$

$$x = 2\pi a/\lambda \tag{12}$$

$$c/\lambda$$

For cases with a clearance-to-wavelength ratio >0.5, which is the case for almost all heat transfer problems, the ratio is unimportant [66]. Therefore, in the present work, this parameter is ignored, and the scattering is deemed to be independent, i.e., the scattering at one particle is not affected by surrounding particles. The complex index of refraction consists of one real part, the refractive index n_λ, and one imaginary part, the absorptive index k_λ. It should be noted that each of the particle types have distinct radiative properties. In this work, we differentiate

between fuel, ash, and soot particles, although all the particles are treated as spheres. Absorption and scattering properties are usually calculated from the Rayleigh theory, for smaller particles, such as soot; and Mie theory, for larger particles, i.e., fuel, char, and ash particles [2].

Rayleigh Theory

For particles that are much smaller than the radiated wavelengths, such as soot particles, the scattering is negligible and, the RTE can be described in the same manner as in Eqn. (2), albeit for particles. Using the Rayleigh theory, the absorption coefficient can be calculated from the particle volume fraction rather than from the size of the particles. With the complex refractive index of the particles, the absorption coefficient can be calculated according to:

$$\kappa_\lambda = E(m_\lambda)\frac{6\pi f_\mathrm{v}}{\lambda} \tag{13}$$

where f_v is the particle volume fraction, λ is a given wavelength, and $E(m_\lambda)$ is a function of the complex refractive index, such that:

$$E(m_\lambda) = -Im\left[\frac{(m_\lambda^2-1)}{(m_\lambda^2+2)}\right] = \frac{6n_\lambda k_\lambda}{\left(n_\lambda^2-k_\lambda^2+2\right)^2+4n_\lambda^2k_\lambda^2} \tag{14}$$

Wavelength-dependent functions of the complex refractive index have been developed for soot particles by Stull & Plass [15], Dalzell & Sarofim [16], Lee & Tien [17] and Chang & Charalampopoulos [18]. However, more recent studies have claimed that the wavelength dependency on the $E(m_\lambda)$-function is low or negligible. Coderre et al. [67] have suggested that the function value is remarkably constant at around 0.35, in the wavelength range of 450–750 nm. However, in the present work, a wider spectral range is in focus and the complex refractive index derived from the work of Chang & Charalampopoulos [18] is used for the soot particle properties, with validity for the wavelength range of 0.4 – 30.0 μm.

$$\begin{aligned} n_\lambda &= 1.811 + 0.1263\ln\lambda + 0.027\ln^2\lambda + 0.0417\ln^3\lambda \\ k_\lambda &= 0.5821 + 0.1213\ln\lambda + 0.2309\ln^2\lambda + 0.01\ln^3\lambda \end{aligned} \tag{15}$$

Mie Theory

The Mie theory, which was developed by Gustav Mie [68], describes the radiative scattering of light by spherical particles. While the theory is complex, it essentially solves the Maxwell equations for an electromagnetic wave traveling through a medium that contains a sphere. The theory generates absorption and scattering coefficients, which are calculated from the respective efficiency factors, Q_{abs} and Q_{sca}, and the projected surface areas of the particles, A_{proj}.

$$\begin{aligned} \kappa &= Q_{abs}A_{proj} \\ \sigma_s &= Q_{sca}A_{proj} \end{aligned} \tag{16}$$

The efficiency factors are calculated in this work using the derivations of Hulst [69] or Bohren and Huffman [70]. The absorption efficiency factor is calculated from the extinction and scattering efficiency factors such that:

$$Q_{abs} = Q_{ext} - Q_{sca}$$

$$Q_{sca} = \frac{2}{x^2}\sum_{n=1}^{\infty}[(2n+1)(|a_n|^2 + |b_n|^2)] \tag{17}$$

$$Q_{ext} = \frac{2}{x^2}\sum_{n=1}^{\infty}[(2n+1)(\mathbb{R}\{a_n\} + \mathbb{R}\{b_n\})]$$

where n is an integer for an infinite series, and the complex numbers a_n and b_n are the Mie scattering coefficients [69], as functions of the complex refractive index. Although the series are infinite, it is not necessary to calculate the sum for a value of n that is larger than a value termed n_{max}. As the n-value exceeds the value of the size parameter x by 2 or 3, the contribution to the sum is negligible [69]. The stop criterion used in this work is taken from the work of Bohren and Huffman [70], according to Eqn. (18):

$$n_{max} = x + 4x^{1/3} + 2 \tag{18}$$

In this work, the Mie theory is used for particles of ash and fuel. The complex refractive index of the fuel particles is in this work fitted to the data from Foster and Howarth [71] (Table 2).

Table 2. Refractive indices used for fuel (coal and char) particles [71].

n_λ	[μm]	k_λ
$1.67 + 0.033\lambda$	$\lambda < 5$	$k_\lambda = 0.3$
	$5 \leq \lambda < 10$	$k_\lambda = -0.5 + 0.16\lambda$
	$10 \geq \lambda$	$k_\lambda = 1.1$

The complex refractive indices for the ash particles show rather large variations in the literature at wavelengths < 5μm. A function that is derived from the combined data from Lohi et al. [72] (0.6–2.6 μm), Gupta and Wall [73] (2.6–5.0 μm), and Goodwin and Mitchner [74] (>5 μm) is used, as previously done by Johansson et al. [75] (Table 3).

Table 3. Refractive indices used for ash particles [72]–[74]

[μm]	n_λ	[μm]	k_λ
$\lambda < 6$	1.5	$\lambda < 2.6$	$-0.0015 + 7.5 * 10^{-3}\lambda$
$6 \leq \lambda < 8$	$1.5 - 0.35(\lambda - 6)$	$2.6 \leq \lambda < 5$	$0.0119 + 2.33 * 10^{-3}\lambda$
$8 \leq \lambda < 11$	$0.8 + 0.5(\lambda - 8)$	$5 \leq \lambda < 9$	$-1.19 + 0.244\lambda$
$11 \leq \lambda < 12$	$2.3 - 0.5(\lambda - 11)$	$9 \leq \lambda < 11$	1.0
$12 \geq \lambda$	1.8	$11 \leq \lambda < 12$	$8.7 - 0.7\lambda$
		$12 \geq \lambda$	0.3

3.1.3 Gas and Particle Interactions

In the furnace, gases and particles co-exist and interact with each other. Using the Rayleigh theory for soot particles and the Mie theory for ash and fuel particles, the total particle absorption and scattering coefficients at a point can be calculated as the sum of the coefficients for the different particle types:

$$\kappa_\nu = \kappa_{\nu,soot} + \kappa_{\nu,coal} + \kappa_{\nu,ash}$$
$$\sigma_{s\nu} = \sigma_{s\nu,coal} + \sigma_{s\nu,ash} \tag{19}$$

The particle absorption and scattering coefficients can be used to calculate transmissivity along a distance *s,* according to Eqn. (7). The total transmissivity can be calculated as the product of the transmissivities of the gases and particles:

$$\tau_{\nu_k} = \tau_{\nu_k,g}\tau_{\nu_k,p} \tag{20}$$

Gray particle properties can be calculated from the spectral properties and used in a gray model, such as the WSGG model, according to Planck averaging:

$$\kappa_{gray,particles} = \frac{1}{I_b}\sum \Delta\nu I_\nu \kappa_\nu$$
$$\sigma_{s,gray,particles} = \frac{1}{I_b}\sum \Delta\nu I_\nu \sigma_{s\nu} \tag{21}$$

3.2 Cylindrical Furnaces

Calculating the radiative intensity field in a furnace requires a model that solves the RTE, including emission, absorption, and scattering due to the gases and particles present. The furnaces examined and modeled in this work are cylindrical, and two modeling approaches are used, namely the *discrete transfer model* and the *discrete ordinates method.* Both models employ the S_N-approximation and discrete ordinates to identify appropriate directions and weighted rays of intensities.

The input data required by the radiation models comprise mainly temperature, gas composition and particle property profiles, and they should preferably be gathered from measurements. The model outputs of most interest are the separate and total radiative intensities from the gases and particles, as well as the radiative heat flux to the furnace wall.

3.2.1 S_N-approximation

In the models, the radiative intensity is calculated in a set number of directions, solving the RTE. The directions of the rays are, in this work, derived according to an S_N-approximation. The *N* term denotes the number of different direction cosines used for each principal direction, such that the total number of directions is given by: $N \cdot (N+2)$, typically distributed according to either the S_4-, S_6- or S_8-approximations. According to Fiveland [76], the angular discretization with the S_4-approximation may yield sufficiently reasonable solutions for some systems, while higher values give more detail but require considerably more computational effort. Each direction is given by the direction cosines ξ_m, η_m and μ_m for a ray traveling along the discrete direction $\hat{\boldsymbol{s}}_m$ according to Eqn. (22) and Figure 12 [77], [78]:

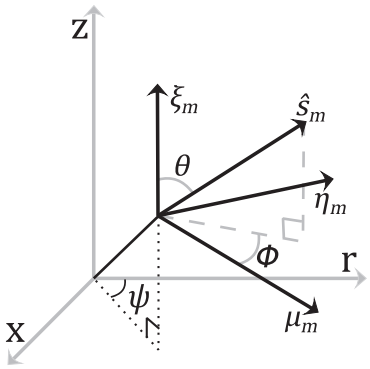

$$\hat{\boldsymbol{s}}_m = \xi_m \hat{\boldsymbol{\imath}} + \eta_m \hat{\boldsymbol{\jmath}} + \mu_m \hat{\boldsymbol{k}}$$

$$\xi_m^2 + \eta_m^2 + \mu_m^2 = 1$$

$$\xi_m = \cos\theta \qquad (22)$$

$$\eta_m = \sin\theta \sin\phi$$

$$\mu_m = \sin\theta \cos\phi$$

Figure 12. The direction cosines (ξ_m, η_m and μ_m) for the discrete direction $\hat{s}_m$ in a cylindrical enclosure.

where θ and ϕ are the polar and azimuthal angles, respectively, and ψ a space variable in the azimuthal direction. To cover the whole sphere, of 4π sr, to which radiation may be emitted from a point, the ordinates may be positive or negative. Each set of ordinates is also connected to a weight, *w*, such that:

$$\sum_{m}^{N} (\xi_m^2 + \eta_m^2 + \mu_m^2) \cdot w_m = 4\pi\, sr \qquad (23)$$

when both positive and negative signs of the cosine directions are considered. The directions given in one eighth of a full sphere, where all the ordinates are positive, are given for the S_8-approximation in Table 4, [2]. All other directions are given by altering the combination of positive or negative signs in front of the ordinates, resulting in eight directions for each row.

Table 4. Discrete ordinates for the S_8-approximation, as collected from a previous work [2].

Ordinates			Weights
ξ	η	μ	w
0.1422555	0.1422555	0.9795543	0.1712359
0.1422555	0.5773503	0.8040087	0.0992284
0.1422555	0.8040087	0.5773503	0.0992284
0.1422555	0.9795543	0.1422555	0.1712359
0.5773503	0.1422555	0.8040087	0.0992284
0.5773503	0.5773503	0.5773503	0.4617179
0.5773503	0.8040087	0.1422555	0.0992284
0.8040087	0.1422555	0.5773503	0.0992284
0.8040087	0.5773503	0.1422555	0.0992284
0.9795543	0.1422555	0.1422555	0.1712359

3.2.2 Discrete transfer model

The discrete transfer model (DTM) was developed to solve the RTE for representative rays of intensity in a volume by tracing the rays that travel from one surface to another in predetermined directions. The model was first developed by Lockwood and Shah [79], who tested the model for one-, two-, and three-dimensional problems and found good accordance with analytical solutions and with solutions generated using the Monte Carlo method. The rays used were set so as to be directed to a point, such that they were distributed angularly in an equal fashion in

space. In this work, the furnace is treated as an infinitely long cylinder with axisymmetric properties within the DTM [75]. That is, the temperatures, as well as the gas and particle concentrations are symmetrically distributed around the axis of the furnace and there are no gradients in the axial direction. This simplification of an axisymmetric cylindrical furnace means that when one is tracing a ray through the center position of a furnace, it is only necessary to make the calculation for rays in a quarter of a hemisphere. Thus, when tracing a ray in either the forward or backward direction, the number of rays needs to be considered is decreased to: $N \cdot (N+2)/8$.

The radiative intensity is calculated along a number of grid points set between the furnace wall and the center position. Rays from the directions given by the S_N-approximation, crossing the grid points, are traced and the total number of rays in the model is equal to the number of grid points multiplied by the number of rays in each point [75]. The grid-point discretization of the path can is illustrated in Figure 13.

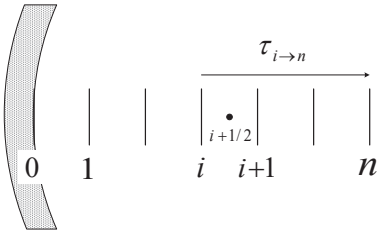

Figure 13. Discretization of the radiative path in the discrete transfer model.

As the ray is traced, the intensity at cell node n, $\bar{I}_{\nu_k,n}$, is dependent upon the emissions of all the upstream cells, as well as the radiation leaving the wall. The intensity is calculated as the sum of the difference in transmissivity between the two cell walls of the same cell, along the path to n, multiplied by the spectral black body intensity, $\bar{I}_{b\nu}$. Here, the gas properties are calculated in the DTM using the Malkmus SNBM, and if only gases and/or soot particles are present along the path the solution to the RTE for a narrow band k may be written according to Eqn. (24) at the end of the path, at position n:

$$\bar{I}_{\nu_k,n} = \bar{I}_{\nu_k,0}\bar{\tau}_{\nu_k,0\to n} + \sum_{i=0}^{n-1}\left(\bar{\tau}_{\nu_k,i+1\to n} - \bar{\tau}_{\nu_k,i\to n}\right)\bar{I}_{b\nu_k,i+½} \tag{24}$$

If scattering particles are present along the path, the Mie theory is used for the particle properties and solving the RTE becomes more complex and may be expressed as:

$$\bar{I}_{\nu_k,n} = \bar{I}_{\nu_k,0}\bar{\tau}_{\nu_k,0\to n} + \sum_{i}\left(\left(1-\bar{\omega}_{\nu_k,i+½}\right)\bar{I}_{b\nu_k,i+½} + \frac{\bar{\omega}_{\nu_k,i+½}}{4\pi}G_{k,i+½}\right)\left(\bar{\tau}_{\nu_k,i+1\to n} - \bar{\tau}_{\nu_k,i\to n}\right) \tag{25}$$

where G is the incident intensity integrated over all directions, and $\bar{\omega}_{\nu k}$ is the scattering albedo. The albedo is the relative importance of the scattering, such that a value of 0 is equivalent to no scattering and a value of 1 signifies pure scattering and no absorption and is given as:

$$\bar{\omega}_{\nu_k} = \frac{\bar{\sigma}_{s\nu_k,coal} + \bar{\sigma}_{s\nu_k,ash}}{\bar{\beta}_{\nu_k,coal} + \bar{\beta}_{\nu_k,ash} - \ln\left(\bar{\tau}_{\nu_k,g}\right)/\Delta s_{cell}} \tag{26}$$

where β is the extinction coefficient ($\beta = \kappa + \sigma_s$) and Δs_{cell} is the cell length. The total radiative intensity at position n is then calculated as the sum of all the spectral intensities and the bandwidth of each band k:

$$I_{tot,n} = \sum_k \Delta\nu_k \bar{I}_{\nu_k,n} \tag{27}$$

The incident radiative heat flux to the furnace wall is calculated from the weighted sum of the intensities for the different directions, m, according to the S_N-approximation:

$$q_r'' = \sum_{i=m}^{N} I_m w_m \zeta_m \tag{28}$$

with ζ_m representing any direction cosine. The wall surface is assumed to be gray and diffuse.

3.2.3 Discrete ordinates method

As gradients along the furnace axis are not considered in the DTM, it is of interest to study the entire cylindrical furnace using a three-dimensional model. Developed from neutron transport by Carlson and Lathrop [80], the discrete ordinates method (DOM) divides the cylindrical furnace volume into cells in the radial r, axial z, and angular ψ directions, so that the total number of cells is given by Eqn. (29):

$$n_{tot} = n_r \cdot n_\psi \cdot n_z \tag{29}$$

An example of cell discretization for a cylindrical furnace is shown in Figure 14a. The DOM has been used previously for modeling radiative heat transfer in cylindrical furnaces [78], [81], [82]. The properties, such as gas composition, particle-projected surface area, and temperature, are set at the cell nodes, while the surface properties are set at the cell surface nodes, i.e., no symmetry assumption is required. Compared to the DTM, in the DOM, the modeled furnace is not infinite and, thus, also has a bottom (burner) and a top (flue gas exhaust) end. However, considering the rotary kiln used for iron ore pellet production, a bed of iron ore pellets fills approximately 8%–12% (X_{bf}) of the furnace volume. If the bed is assumed to be evenly distributed along the axis of the furnace, it can be represented by a flat surface (Figure 14b), as has been done previously [83]. The furnace volume can be considered as a "semi-cylindrical" enclosure with two cell types, *I* and *II*.

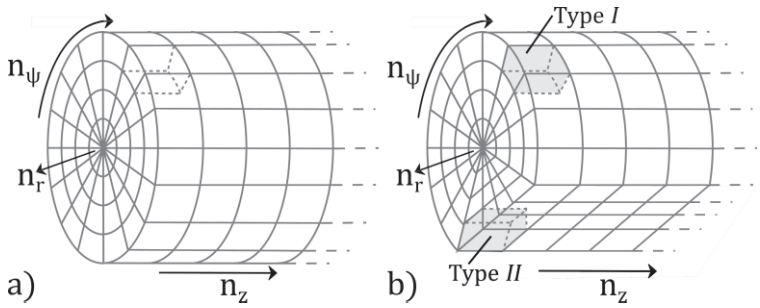

Figure 14. a Cell discretization of a cylindrical furnace. Considering the rotary kiln used for iron ore pellet production, a bed is present and can be represented in the model according to **b** with two cell types, *I* and *II*.

It is desirable to maintain the angle, $\Delta\omega$, between two cells in the angular direction (ψ) constant while adding the bed material. To do so, the total number of cells in the angular direction (N_ψ) can be varied to minimize the bed filling degree error, X_{bfe}, expressed in Eqn. (30). In radians, the bed filling degree, X_{bf}, and $\Delta\omega$ are related as follows:

$$\Delta\omega = \frac{2\pi}{N_\psi}$$
$$X_{bf} + |X_{bfe}| = \frac{2\pi - \Delta\omega}{2\pi} + \frac{\cos\left(\frac{\Delta\omega}{2}\right)\sin\left(\frac{\Delta\omega}{2}\right)}{\pi} \tag{30}$$

For the cylindrical and semi-cylindrical enclosures of a rotary kiln, the RTE may be expressed in terms of cylindrical coordinates [81] according to Eqn. (31) (see Figure 12).

$$\frac{\mu_m}{r}\frac{\delta(rI_m)}{\delta r} + \frac{\eta_m}{r}\frac{\delta I_m}{\delta\psi} + \xi_m\frac{\delta I_m}{\delta z} - \frac{1}{r}\frac{\delta(n_m I_m)}{\delta\phi} = -(\kappa+\sigma_s)I_m + \kappa I_b + \frac{\sigma_s}{4\pi}\int_{4\pi} P(\Omega,\Omega')I_{m'}d\Omega' \tag{31}$$

To solve Eqn. (31), for cell types *I* and *II*, Eqn. (31) is multiplied by the expressions given by Eqn. (32):

Type *I*	$2\pi r\ dr\ dz\ d\psi$
Type *II*	$r\frac{1}{\cos^2(\Delta\omega)}\ dr\ d\psi\ dz$

(32)

and integrated over the volume elements for each cell type. For both cell types, the expression is then:

$$\mu_m\left(A_{i+1}I_{m,i+1} - A_iI_{m,i}\right) + \eta_m\left(B_{j+1}I_{m,j+1} - B_jI_{m,j}\right) + \xi_m\left(C_{k+1}I_{m,k+1} - C_kI_{m,k}\right) + \frac{\alpha_{m+½}I_{m+½} - \alpha_{m-½}I_{m-½}}{w_m} = V_p\left[-(\kappa+\sigma_s)I_m + \kappa I_b + \sigma_s I_s\right] \tag{33}$$

The $\alpha_{m\pm1/2}$-terms are introduced to handle the discretization of the direction vector η and to correct for the curvature of the cylindrical furnace [80], [84]. The A_i, B_j and C_k terms represent the cell wall areas through which the radiation enters and leaves the cells, in the radial, angular, and axial directions, and V_p is the cell volume. The subscripts i, j and k represent the cell numbers in the radial, angular, and axial directions respectively. The two cell types, *I* and *II*, result in six cell surfaces, as shown in Figure 15.

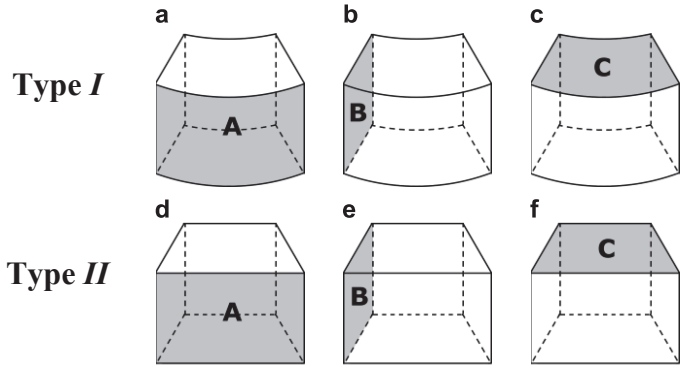

Figure 15. Representation of the two cell types and surface areas present using the discrete ordinates method for a cylindrical furnace without (**a**–**c**) and with (**d**–**f**) a bed material being present.

Defining the cells from a line drawn between the center of the furnace and the middle of the bed surface, in the angular direction, $r_{n_r,c}$ is the shortest distance from the central axis of the kiln to the bed surface. Each cell surface can then be expressed according to Eqn. (34).

$$A_{I,i} = r_i \Delta\omega_j \Delta z_k \qquad A_{II,i} = r_{i,c}\left(\tan(\omega_{j+1}) - \tan(\omega_j)\right)\Delta z_k$$

$$B_{I,j} = \Delta r_i \Delta z_k \qquad B_{II,j} = \Delta r_i \Delta z_k \tag{34}$$

$$C_{I,k} = \pi(r_{i+1}^2 - r_i^2)\Delta\omega_j \qquad C_{II,k} = \frac{r_{i+1,c}^2 - r_{i,c}^2}{2}\left(\tan(\omega_{j+1}) - \tan(\omega_j)\right)$$

The cell volume for any cell can be calculated according to Eqn. (35).

$$V_P = C_k \Delta z_k \tag{35}$$

To find the $\alpha_{m\pm1/2}$-terms, a case in which divergence-less flow is assumed can be used according to Carlson and Lathrop [80], i.e., a case with neither intensity sources nor sinks and all intensities are alike. Considering the different cell surfaces, it may be observed that for cell type *I*: $B_{j+1} = B_j$, and for both cell types (*I* and *II*): $C_{k+1} = C_k$, while $A_{i+1} \neq A_i$ for all cells. The right-side of the expression in Eqn. (33) becomes zero and for the two cell types, the following expressions are achieved:

$$\textbf{Type } \textit{I} \qquad \alpha_{m+½} - \alpha_{m-½} = -\,w_m \mu_m (A_{i+1} - A_i)$$

$$\textbf{Type } \textit{II} \qquad \alpha_{m+½} - \alpha_{m-½} = -w_m\left[\mu_m(A_{i+1} - A_i) + \eta_m\left(B_{j+1} - B_j\right)\right] \tag{36}$$

With the first α-term, $\alpha_{1/2} = 0$, the following terms may be readily calculated. In contrast to the DTM, the radiative heat transfer is not traced along one discrete ray along the furnace diameter. The rays spread from the nodal points in the cells over a sphere, and calculations are performed for one-eighth of a sphere at a time. The RTE is solved in each discrete direction, which results in as many coupled partial differential equations, and an iterative process is required. The procedure starts at the outer wall at one end of the cylinder. Assumed values for the angular and reflected intensities are used in the first iteration and, thereafter, updated in each

iteration. The WSGG model is used to model the gases in the furnace and the Mie and Rayleigh theories are used for the different particle types, while the gray properties are calculated for each cell using Planck averaging according to Eqn. (21). The radiative intensity to a node-point *P* from one direction in a quadrant, with the beam directed from the wall to the furnace center, is expressed by Eqn. (37) [81].

$$I_{mP} = \frac{\mu_m A I_A + \eta_m B I_B + \xi_m C I_C + \frac{\alpha I_\alpha}{w_m} + (\kappa I_b + \sigma_s I_{sca}) V_P}{\mu_m A + \eta_m B + \xi_m C + \frac{\alpha}{w_m} + (\kappa + \sigma_s) V_P} \tag{37}$$

Here, the upstream intensities of I_A, I_B and I_C are calculated using a diamond differencing scheme. The diamond scheme is, however, known to suffer from the shortcoming of eventually producing negative intensities. In the model, if any such values appear, they can be set to zero. The radiative heat flux incident to the furnace wall can be calculated as the sum of the incident radiations from all directions, as in Eqn. (28). The wall and bed surfaces are assumed to be gray and diffuse.

3.2.4 Modeling input data

Various parameters, such as the gas and particle temperatures, gas composition, particle surface area, and soot volume fraction are used as input data to the models. In the DTM, axisymmetry is assumed and radial profiles are created for each parameter as it is introduced to the model. In the DOM, it is possible to set any parameter value in each cell node and no symmetry is required. These parameters should be estimated in some way, preferably through accurate measurements. The input data used in this work are mainly based on measurements made in various flames. However, as the access for performing measurements is limited, some assumptions are necessary between two measurement positions. For cells that are located at positions between two measurement positions, interpolated values were calculated using a linear average in both models, except for the temperature and particle concentration values.

In this work, for the radial temperature profiles, the temperatures measured on each side of the furnace central axis, say the right-side and left-side, were used, and the average value was calculated considering the temperatures to the power of four, according to Eqn. (38). However, separate temperatures for the gases and particles were not measured, and it has been assumed that the particles have the same temperature as the surrounding gas.

$$\bar{T} = \left(\frac{T_{Right}^4 + T_{Left}^4}{2} \right)^{\frac{1}{4}} \tag{38}$$

In the studied cases using a solid fuel, particles were extracted only at the center positions, mainly due to time restrictions during the measurement campaigns. Therefore, the particle distribution has to be estimated from a single point. It was assumed that the particles were either spread along a portion of the furnace diameter, from the central axis by employing a cosine-function, or that the measured concentration was the same across the entire furnace diameter, as discussed in Paper I. The second option was used at downstream positions, close to the end of the flame. For the first option, which was used at positions closer to the burner and within

the flame, the particle-projected surface area, A_{proj}, is assumed to be distributed at position r on the furnace radius R according to Eqn. (39):

$$\begin{aligned} 0 \le r \le R_f \qquad & A_{proj}(r) = f_{proj} \cdot \frac{R^2}{R_f^2} \cdot 1.681 \left(\cos\left(\frac{\pi \cdot r}{R_f} \right) + 1 \right) \\ R_f < r \le R \qquad & A_{proj}(r) = 0 \end{aligned} \tag{39}$$

where R_f, is the flame radius, i.e., the distance from the furnace center where particles are assumed to be present, and f_{proj} is the projected surface area if the particles are equally distributed across a disc along the flame diameter. For positions that lie very close to the burner, the fuel size distribution, measured before feeding to the burner, was used instead. For these positions, the total project surface area, integrated over the whole furnace diameter, was assumed to be known and the particles were assumed to be equally distributed, resembling a top hat, for different flame radii. Figure 16 shows three examples of particle distribution in a furnace with a radius of 325 mm, for a position very close to the burner (Figure 16a), and for a position within the flame (Figure 16b). The three profiles depend on the value of R_f, although the central peak value is constant, corresponding to the particle extraction measurements.

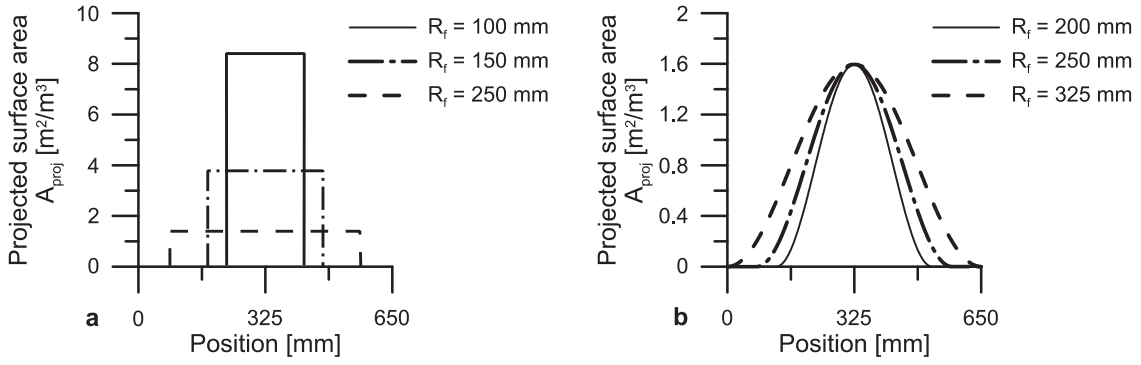

Figure 16. Example of particle distribution over a furnace diameter of 650 mm using three different flame radii according to either a top-hat (**a**) or cosine-function **(b**) distribution.

The flame radius can be revealed by studying the measurements of the radiative intensity along the furnace diameter (for example see Figure 8). This topic is discussed further in Paper I.

3.2.5 Scattering

As mentioned above, when radiation approaches a particle, scattering can occur through diffraction, reflection or refraction. Radiative scattering depends on multiple properties of the particle, such as the size, shape, and composition of the particle [2]. However, in this work, all particles are assumed to be spherical, and it has been shown in the work of Gronarz et al. [85] that particle shape has little importance for scattering. The scattering efficiency factor is calculated for coal and ash particles as already described using the Mie theory for both the DTM and the DOM. It is, however, difficult to describe in a satisfactory way in the models how the scattered light is distributed when leaving the particles, i.e., the scattering phase function. Two commonly applied simplifications involve the assumption that the scattering is: (i) isotropic, i.e., the scattered light is distributed equally in all directions; or (ii) only in the forward direction,

i.e., no scattering. To demonstrate the effect on radiative intensity of scattering, an example is illustrated in Figure 17. Here, a case assuming isotropic scattering is compared to a case assuming only forward scattering, applying the DTM. The modeled case was a coal flame with particles distributed over a portion of the furnace diameter. A cold background (25°C) was used to study the radiation from the flame and the in-scattered radiation from the surroundings. An otherwise surrounding furnace wall at 500°C (Figure 17a) was compared to a warmer wall at 1200°C (Figure 17b). It is clear from the results that in-scattering has a stronger impact on the radiative intensity when the furnace wall is hot. This is due to radiation from the warm wall being scattered in the narrow direction studied here, directed towards the cold background.

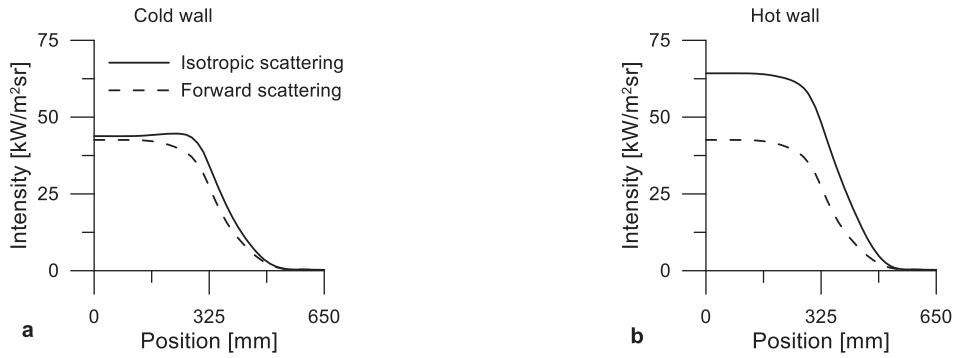

Figure 17. Full isotropic scattering of the incoming radiation is compared to forward-scattering for a flame with a solid fuel. The wall temperature is 500°C (**a)** or 1200°C (**b**).

In our earlier studies, scattering was assumed to be isotropic, which resulted in only minor errors (Figure 17a) for a colder furnace wall. However, for cases in which the furnace wall is heated, as in the rotary kiln furnace, the effects of scattering are considerably more potent (Figure 17b). It has, however, been shown that scattering is usually much stronger in the forward direction of the incoming radiation [2] and Gronarz et al. [86] have suggested using a forward scattering of about 80%. Therefore, further work should be focused on improving the modeling of the scattering due to particles in the radiation models. Moreover, the different types of particles warrant more detailed studies.

3.3 Rotary Kilns with a Passing Bed Material

The bed material in a rotary kiln is heated primarily through radiation from the flame and kiln wall. However, it is also heated by conduction from the contact with the wall and convection via the passing gas, and possibly through exothermic reactions within the bed. The wall receives heat from the flame and cooling from the bed material and outer heat losses as it rotates. Furthermore, since the temperature difference between the bottom bed layer and wall is relatively large for most of the kiln length, it can be argued that it is also important to take into account radiative heat transfer under the bed. To calculate the product temperature, all these mechanisms should be considered when modeling a rotary kiln with a bed material.

3.3.1 Bed Motion and Advective Heat Transfer

According to the definition provided by Henein et al. [87], the bed motion of iron ore pellets in the rotary kiln is considered to have a rolling bed mode, characterized by a rather even bed level in a cross-section of the kiln and continuous motion of the surface bed layer. The bed material

is here considered to be divided into two parts in the model: a surface (s) layer and a bottom (b) layer, in accordance with Figure 4 and similar to what has been assumed in earlier works, [39], [40], [45]. A fictitious boundary line is assumed between the two layers such that no heat is transferred at the contact points between the two layers. The pellets within a single cell of the bottom layer are assumed to be at rest in relation to the wall, i.e., there is no mixing of the pellets and the bed is assumed to have no slip to the wall. Unlike the bottom bed layer, perfect mixing is assumed in the surface layer at each separate angular position, with the consequence that the bed material within a surface layer cell is isothermal. The portion of the bed material that follows the wall, within a bottom bed layer cell, is defined from the cell volume of the first angular bed cell of the bottom layer, $n_{\psi b} = 1$, located at angular position $n_{\psi} = N_{\psi} - N_{\psi b}$ on the kiln wall, according to Figure 18. As the wall and bed move, this mass of pellets is immediately substituted with pellets derived from the surface layer in an equivalent amount, given as a volume portion from the surface layer cell at $n_{\psi s} = N_{\psi s}$. Pellets in the surface layer then move accordingly from higher to lower positioned angular cells all the way from cell $n_{\psi s} = 1$. The time that it takes for the wall to move one full step in the model (angular length of one cell) is denoted as t_{ψ} and is dependent upon the rotational speed of the kiln wall and cell discretization. At position $n_{\psi b} = N_{\psi b}$, the bottom bed pellets have reached the highest position in the cross-section of the bed and are mixed into the surface layer at $n_{\psi s} = 1$. The time that it takes for a pellet in the bottom layer to travel the full cross-sectional length of the bed (from $n_{\psi b} = 1$ to $n_{\psi b} = N_{\psi b}$), is, therefore, $t_{\psi b} = t_{\psi} N_{\psi b}$.

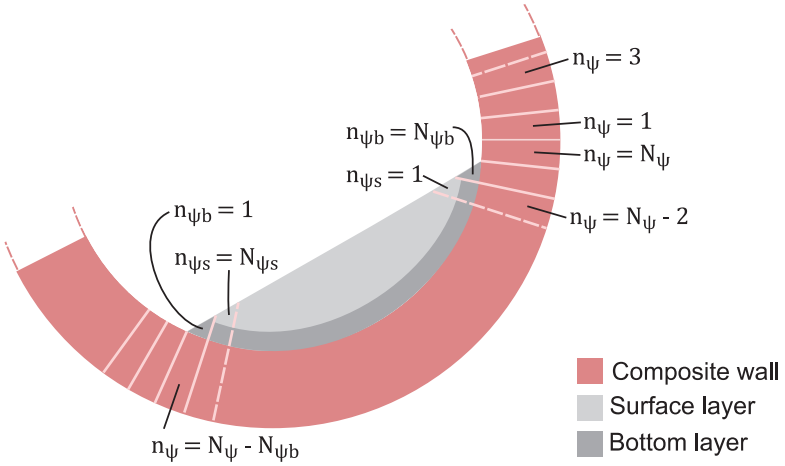

Figure 18. Cell discretization of the wall and bed material in a surface (s) and in a bottom (b) layer, for a rotary kiln.

3.3.2 Radiative Heat Transfer

To calculate the radiative heat transfer in the rotary kiln, the DOM is used. The incident radiative heat flux to the furnace kiln wall or bed material can be calculated from Eqn. (28). If there is net heat flux to the bed or wall, the surface temperature may be updated in the model from the accumulated heat due to radiation. Assuming gray and diffuse properties for the different surfaces and further assuming that the bed (b) and wall (w) temperatures are constant during time t_{ψ}, the accumulated heat, W, at the surface can be expressed according to Eqn. (40).

$$W_{rad} = [\varepsilon A_A (q_r'' - \sigma T^4)]_{b/w} t_\psi \quad (40)$$

Here, ε is the emissivity of the surface and σ the Stefan-Boltzmann constant. It can be argued that radiative heat transfer also occurs below the bed material, between the wall and the bed material close to the wall. Due to the spherical shape of the pellets, only a portion of the wall surface area, A_w, is in direct contact with the bed, X_c, while the remaining surface will emit and absorb radiation from its surroundings, as illustrated in Figure 19 for which a well-packed bed is assumed to have the type face-centered cubic packing.

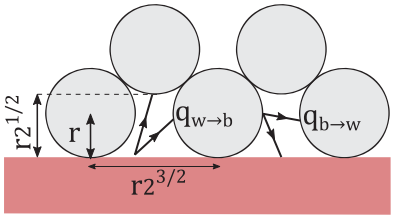

Figure 19. Radiative heat transfer under the bed material, assuming a face-centered cubic packing structure for the iron ore pellets.

Since a portion of the radiation will always be reflected within the cavity, the absorbed energy is dependent on the emitted and the reflected radiation and can be expressed in terms of the radiosity, J, from the wall and bed material respectively. It is assumed that the radiation from the wall never reaches further into the bed than to the first- and second-pellet layers closest to the wall. The view factors, F, are calculated for the face-centered cubic packing structure, depending on the pellet radius.

$$\begin{aligned} W_{rad,below,\to b} &= (A_{Aw}F_{wb}J_w + A_{Ab}F_{bb}J_b - A_{Ab}J_b)\varepsilon_b(1 - X_c)t_\psi \\ W_{rad,below,\to w} &= (A_{Ab}F_{bw}J_b - A_{Aw}F_{wb}J_w)\varepsilon_w(1 - X_c)t_\psi \end{aligned} \quad (41)$$

Radiative heat exchanges between the pellets are otherwise ignored, as the temperature difference between neighboring pellets is considered to be small.

3.3.3 Conductive Heat Transfer

To describe the conductive heat transfer between the wall and bed material that occurs under the bed, an unsteady-state penetration model of the bottom bed layer has been used, under the assumptions of no mixing within the bottom bed layer and no slip to the wall. As the bed material and wall meet, the two surfaces will adopt the same surface temperature where they are in contact. The contact surface temperature, T_{cs}, can be calculated according to Eqn. (42):

$$T_{cs} = \frac{(k\rho C_p)_w^{0.5} T_w + (k\rho C_p)_b^{0.5} T_b}{(k\rho C_p)_w^{0.5} + (k\rho C_p)_b^{0.5}} \quad (42)$$

where k is the thermal conductivity, ρ is the density of the solid material, and C_p is the specific heat capacity. Early attempts to construct such a penetration model were made by Wes et al [40], with modifications introduced subsequently by others [41], [88], [89], in which a fictitious gas film was introduced as a heat transfer resistance. Later, Herz et al. [39] examined how well

the models aligned with actual measurements and found that the penetration model used by Wes and colleagues among others showed reasonable levels of agreement. In the present work, no fictitious gas film is considered, and penetration models are used for both the wall and bed material. The heat transferred between the two materials due to conduction is described according to Eqn. (43) over a period of $t_{\psi b}$ seconds:

$$W_{cond,b/w} = A_w X_c \left[\rho C_p \int_0^{t_{\psi b}} \int_{d_T=0}^{d_T=0.99} \delta \, T(\delta, t) \, d\delta \, dt \right]_{b/w} \tag{43}$$

where d_T is the temperature distribution within the thermal penetration depth δ of the bed or wall. The distribution is set so as to vary from the contact surface temperature, T_{cs}, to a temperature that is 99% of the temperature difference between the initial material temperature (of the bed or wall) and the contact surface temperature, which may be derived from the Gaussian error function according to Eqn. (44) [90]. That is, however, under the assumption that as the bed and wall meet (at $n_{\psi b} = 1$ according to Figure 18), each cell is considered isothermal within one angular cell, at each respective temperature. Furthermore, the depth of the temperature profile cannot be greater than the thickness of the bottom bed layer or wall thickness, $l_{b/w}$, after $t_{\psi b}$ seconds. This is controlled and checked in the model.

$$d_T = \left[\frac{T(\delta, t) - T_{cs}}{T_i - T_{cs}} \right]_{b/w} = \left[\operatorname{erf}\left(\frac{\delta}{2} \left(\frac{k t_\psi}{\rho C_p} \right)^{-0.5} \right) \right]_{b/w} \tag{44}$$

$$l_{b/w} > \delta_{b/w} = 3.64 \left[\sqrt{\frac{k t_\psi}{\rho C_p}} \right]_{b/w} \quad (\text{for } d_T = 0.99)$$

3.3.4 Convective Heat Transfer

Heat is also transferred between the gas passing through the kiln and the bed or wall surfaces due to convection. Global expressions of the heat transfer coefficient obtained from the work of Gorog et al. [42] have been used here and elsewhere, e.g., [91], [92]. The heat transfer from the gas to either surface is described by:

$$h_{g \to w} = 0.036 \frac{k_g}{D} Re_D^{0.8} Pr^{0.33} \left(\frac{D}{L} \right)^{0.055} \tag{45}$$

$$h_{g \to b} = 0.4 \, G_g^{0.62} \tag{46}$$

where D is the diameter and L is the length of the rotary kiln, and G_g is the mass flux of gas passing through the kiln. It should, however, be noted that convective heat transfer is only considered in one direction within the model. Thus, while the wall and bed may be heated or cooled by the gas, the gas temperature is kept constant, as it is set as an input parameter to each cell node, based on real measurements.

3.3.5 Reactive Bed Material

As the iron ore pellets are transported through the rotary kiln, magnetite is oxidized to hematite, in a strongly exothermic reaction that should be accounted for in the model. From the process point-of-view, the bed material should already be fully oxidized as it enters the rotary kiln, although some oxidation will occur within the kiln. In the kiln, the amount of available oxygen in the gas within the bed is limited by the fuel combustion, as well as by the mixing of the pellets with the freeboard gas, so the oxidation is difficult to model in a satisfactory way. Therefore, as a simplification, set bed compositions into and out of the rotary kiln, gathered from the full-scale process, are instead used, and the heat from reaction is added as a source term, evenly distributed along the axis of the kiln. The heat of reaction is taken from Forsmo et al. [93]:

$$4Fe_3O_4 + O_2 \rightarrow 6\,Fe_2O_3 \qquad \Delta H = -119\ kJ/mol \qquad \text{R3}$$

The oxidative reaction of iron ore within the grate-kiln process has been studied extensively elsewhere, and detailed models have been developed (for example, see [93]–[96]).

3.3.6 Heat Losses

Heat losses occur at the rotary kiln as heat is transported through the wall to the colder surroundings of the kiln, where heat is transferred by both radiation and convection. The outer wall temperature of the rotary kiln, T_{w_o}, may be calculated from the composite wall materials properties and the outer surrounding temperature, T_∞, according to Eqn. (47).

$$T_{w_o} = T_{W_i} - \frac{T_{w_i} - T_\infty \cdot \dfrac{\ln\left(\frac{D_o}{D_i}\right)}{\bar{k}_w}}{\dfrac{\ln\left(\frac{D_o}{D_i}\right)}{\bar{k}_w} + \dfrac{1}{D_o/2}\left(\dfrac{1}{h_o} + \dfrac{1}{\varepsilon_{w_o}\sigma\left(T_{w_o} + T_\infty\right)\left(T_{w_o}^2 - T_\infty^2\right)}\right)} \tag{47}$$

For the full-scale rotary kiln, the outer convective heat transfer coefficient, h_o, is obtained in the model using a correlation of a rotating cylinder, as previously described by Barr et al. [44].

$$h_o = \frac{k_{go}}{D_o} 0.11\{(0.5Re_\omega^2 + Gr_o)Pr_o\}^{0.35} \tag{48}$$

For the pilot-scale rotary kiln, i.e., a stationary kiln that is a horizontal cylinder, the natural convection on the outside can be expressed from the Nusselt number for a horizontal cylinder, as described by Churchill and Chu [97]. Forced convection on the outside of the kiln is considered to be negligible since the furnace is enclosed within a building.

$$Nu_D = \left(0.60 + \frac{0.387Ra_D^{\frac{1}{6}}}{\left[1 + \left(\frac{0.559}{Pr}\right)^{\frac{9}{16}}\right]^{\frac{8}{27}}} \right)^2 \tag{49}$$

4. Measurement Techniques

In order to better understand and model the radiative heat transfer in furnaces, high-quality measurements of different in-flame parameters are required. Ideally, these measurements would be conducted without interfering with the flame and without affecting the combustion conditions, i.e., using non-intrusive methods. However, this is not always possible, and for some parameters, intrusive methods have to be used. The measurement techniques used in the present work are described below, together with schematics of the measurement equipment.

4.1 Intrusive Measurements

4.1.1 Suction pyrometer

Performing accurate measurements of the flame temperature is challenging, as simply using a thermocouple will result in errors due to radiative influences. Consider a case in which the furnace walls are colder than the flame at the measurement position. Ignoring any radiative absorption by the gas, a simple energy balance at the thermocouple is as follows:

$$A_{tc}h\left(T_f - T_{tc}\right) = A_{tc}\varepsilon\sigma(T_{tc}^4 - T_w^4) \tag{50}$$

That is, due to the radiative heat losses to the surrounding walls, T_w, the temperature measured by the thermocouple, T_{tc}, will be lower than the actual flame temperature, T_f. However, the measurement error may be reduced by increasing the convective heat transfer coefficient, h, from the flame to the thermocouple. Applying suction around the thermocouple increases the gas velocity and, thereby, the convective heat transfer. The radiative heat loss can be decreased further by shielding the thermocouple. This type of instrument is called a suction pyrometer, and it is common to use a single shield for measurements of a gaseous flame, as in Papers IV and V, and a triple shield for measurements of a solid fuel flame, as was used for the data in Papers I–III. Figure 20 presents a schematic of a triple-shielded suction pyrometer of the International Flame Research Foundation (IFRF) type, attached to a water-cooled probe. A type B thermocouple was used for all the measurements in this work.

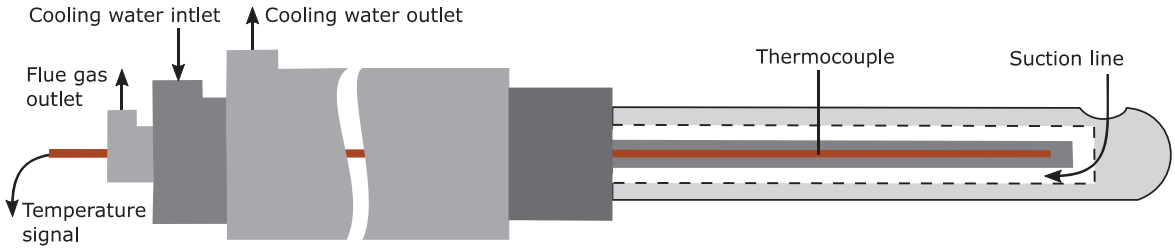

Figure 20. Schematic of a triple-shielded suction pyrometer connected to a water-cooled probe. Gas is sucked through an opening in the outer shield and passed through the middle and inner shields. The thermocouple is protected from the gas by the inner-most shield.

It should be noted that while the increased suction velocity reduces the measurement error, the extracted gas volume also increases, and the measurement will not be a point measurement. Furthermore, the suction applied by the suction pyrometer affects the gas flow pattern of the flame. That is, the suction velocity should be sufficiently high to minimize the measurement error but low enough to ensure a small measurement volume. One problem that can occur when

performing measurements with this instrument is that the suction line becomes clogged with heavy particle loads or ash melts, resulting in a reduced suction velocity and higher levels of uncertainty.

4.1.2 Fourier-Transform Infrared Spectroscopy

To measure the gas compositions within the furnaces, gases were extracted from the furnaces and analyzed using Fourier-Transform Infrared Spectroscopy (FTIR). In FTIR, the absorption at different wavelengths are measured in a small cell, and Fourier transforms are used to convert the measured absorption to a spectrum, which is then compared to a database that contains a high number of species. From this comparison, it is possible to determine which gas species are present and at what concentrations. For more details of the FTIR instrument and technique, see the work of Griffiths and Haseth [98]. The gas was extracted using a water-cooled probe, which prevented the probe from being damaged by the high temperatures of the flames. However, it is desirable to prevent the condensation of water in the system. For this purpose, the probe is equipped with an electrically heated inner tube, which ensures that the gas entering the FTIR is at a temperature of about 200°C. If measurements are performed in a solid fuel flame, high numbers of particles are present, and a filter must be placed at the tip of the probe to avoid clogging the system and to protect the FTIR from particles (Figure 21). The filter used in this work was composed of sintered alumina oxide. For a gas flame, such filters are normally not required, as very few particles are present, although a filter may still be useful if a very sooty flame is being probed. Gas extractions in combination with FTIR were used to gather the measurement data used in Papers I–V.

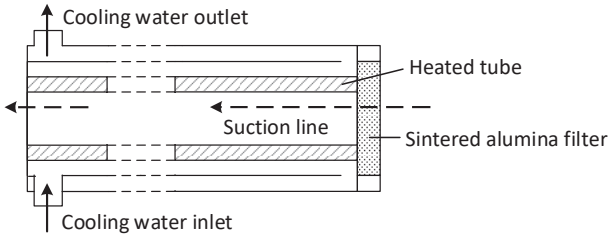

Figure 21. Water-cooled, gas-extraction probe with a sintered alumina oxide filter at the tip. Electrical heating is applied to the inner tube, maintaining a gas sample temperature of 200°C.

4.1.3 Particle extraction probe

Measurements of the particle concentration and size distribution were performed by extracting gas samples including particles from the flame using a probe. The particle sampling inlet was oriented perpendicular to the probe axis (see Figure 22) and was directed towards the burner during the sampling. The extracted gas was diluted with nitrogen in the tip of the probe, to quench any reactions. The overall dilution rate could be estimated by comparing the oxygen concentration in the diluted sampling gas with that at the measurement position. When studying solid fuel flames (Papers I-III) the probe was cooled using water and connected to a low-pressure impactor with thirteen sizing steps, ranging from 30 nm to 10 μm; those particles with a diameter larger than 10 μm were captured in a cyclone. For the sampling of soot particles in a gaseous flame (Paper V) an oil-cooled probe was used instead, maintaining the sample gas temperature at 120°C. The probe was connected to the SMPS and PASS-3 instruments to measure the size distribution and radiative properties of the particles.

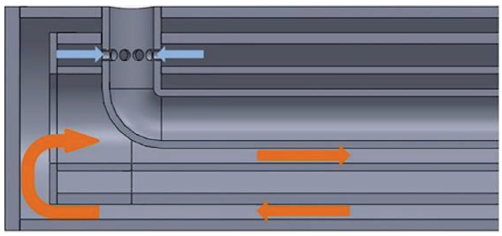

Figure 22. Water-cooled or oil-cooled (orange arrows) particle extraction probe (the top) used to collect in-flame particles. The opening is oriented perpendicular to the probe suction line, and the sample gas is diluted with nitrogen (blue arrows) in the tip of the probe.

It should be noted that it is very complicated to measure the particle distribution in an accurate way. To disturb the flow as little as possible, it is desirable to perform the particle extraction isokinetically, i.e., sampling the particles at a suction velocity that is equal to the flame velocity. However, it has been shown in previous works that have used similar probes that accurate measurements do not require that the sampling is perfectly isokinetic [99]. Moreover, a heavy load of particles has the undesired effect of clogging the probe, even more so if the fuel is biomass, in which case tars may condense in the probe.

4.1.4 Scanning Mobility Particle Sizer

A Scanning Mobility Particle Sizer (SMPS) [100] (Figure 23), provides the size distribution with high resolution for particles with diameters < 1 µm. It is commonly used for atmospheric measurements and is frequently applied in combustion studies to measure soot particles extracted from various flames [101], [102]. In the SMPS, particles are charged by a radioactive source, enters a laminar flow of nitrogen, and then, by applying a voltage over the gas, separated on the basis of their different electrical mobilities in a Differential Mobility Analyzer (DMA) [103]. In a second step, the particles are allowed to grow by addition of iso-butanol and counted in a Condensation Particle Counter (CPC) using a light source and an optical detector. The particle concentration is obtained by making assumptions regarding the particle density and shape (e.g. soot agglomerates). This measurement technique was used in the study described in Paper V.

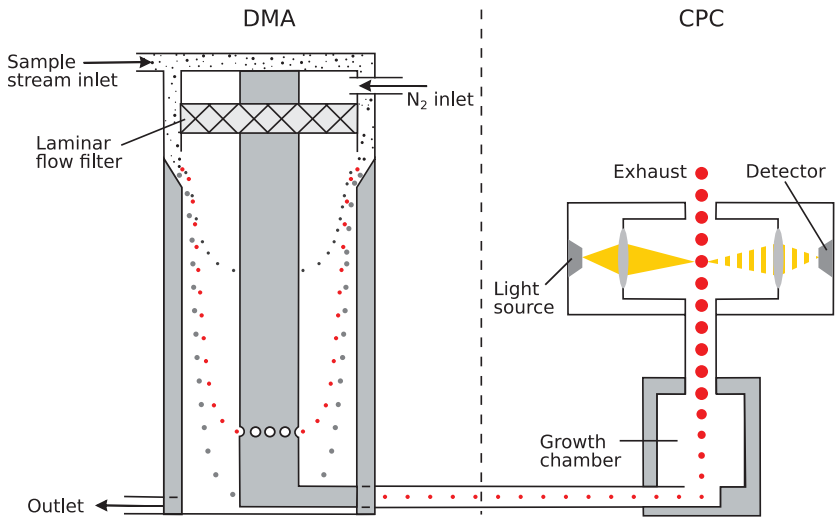

Figure 23. Schematic of the SMPS used to measure the particle size distribution of soot.

4.1.5 Photo-Acoustic Soot Spectrometer

The absorption and scattering coefficients of soot particles can be measured using a Photo-Acoustic Soot Spectrometer (PASS-3) instrument (Figure 24). Lasers with three different wavelengths (405, 532 and 781 nm) are applied to a gas sample, here extracted from a gaseous flame, as described in Paper V. The simplified theory is that the particles absorb the laser energy, and become heated, and as heat is transferred to the surrounding gas, a sound wave is produced, which is captured by a microphone. The sound wave is then correlated to the particle absorption. The scattered light is measured in a nephelometer and related to the scattering coefficient. For more details of the PASS-instrument see the review of Moosmüller et al. [104].

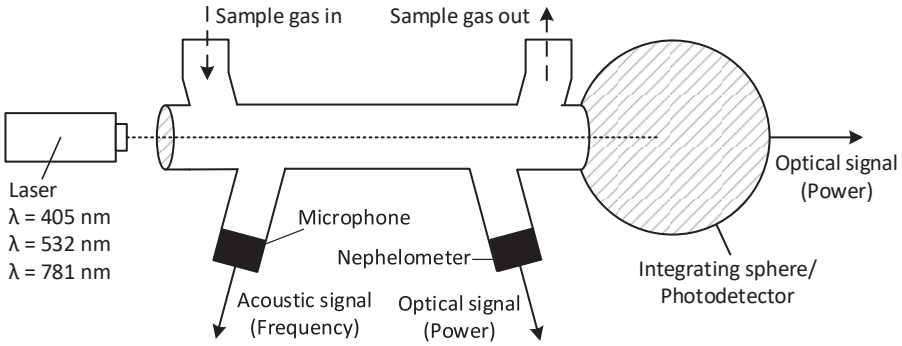

Figure 24. Schematic of the PASS-3 instrument used to measure the absorption and scattering coefficients of soot particles.

4.1.6 Narrow-angle radiometer

The radiative intensity is measured along the furnace diameter using a narrow angle radiometer (NAR) instrument (Figure 25), which has been used in several studies by our research group, [23], [25], [26], [55]. This water-cooled probing instrument is equipped with a thermopile sensor at the back-end of the 2.3 m-long probe. Incoming light passes through the inner passage of diameter 1 cm, and is focused on the sensor. Thus, light rays that originate exclusively at a narrow angle to the sensor's normal will reach the sensor, and the instrument can be considered to measure exclusively the radiative intensity in its line-of-sight. A voltage signal is measured that corresponds to the radiative intensity calibrated to a high-precision, black-body furnace before the start and at the end of a measurement campaign.

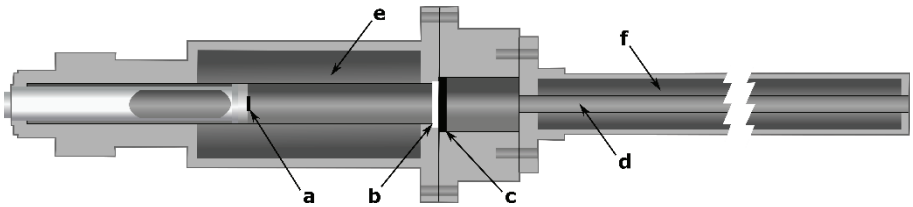

Figure 25. Schematic of the narrow-angle radiometer that was used to measure the total radiation intensity. The probe includes the following components: **a**, thermopile sensor; **b**, focusing lens; **c**, shutter; **d**, collimating tube; **e**, water-cooled sensor housing and **f**, water-cooled probe.

The NAR is traversed through the flame to measure the flame radiation, and most of the direct background radiation (from, for example, a hot furnace wall) can be eliminated if the probe is directed towards a cold background, such as a quartz window. To minimize bending of the probe, owing to high flame temperatures, the probe is made of titanium. A small flow of

nitrogen is used in the ray path to prevent any gases or particles entering the probe. To maintain a constant sensor temperature, separate cooling systems are applied to the probe and the sensor housing. The NAR was used for the measurements reported in Papers I–V.

4.2 Non-intrusive Measurements

4.2.1 Infrared measurements

To better understand the combustion process, it is desirable to visually capture the flame in the furnace. While many cameras could be used for this purpose, an infrared camera can be used to study also the temperature within the furnace. A FLIR A655SC camera with the possibility to measure temperatures up to 2000°C at a sampling frequency of 200 Hz and with a resolution of 640×120 pixels was used in the work for this thesis. Figure 26 shows sample images along the ECF furnace axis (see Section 5.1) captured by the camera for a coal flame. The camera was placed outside the furnace ports and was protected by a cooling house. The recorded videos were analyzed using the FLIR Research IR Max software (Papers I-III).

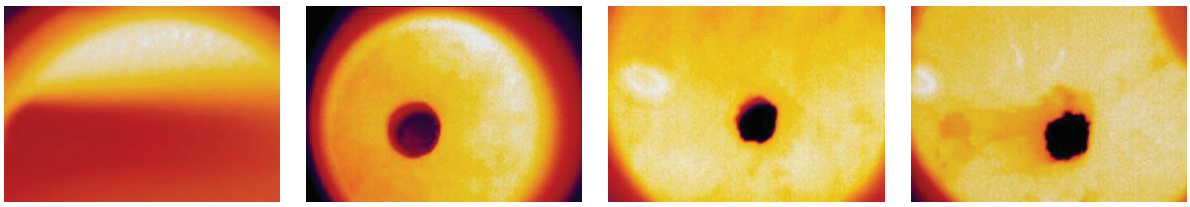

a **b** **c** **d**

Figure 26. Representative images captured by the infrared camera for a coal flame, showing the interior of the furnace with hot particles and the inner wall. The suspension flow moves from the left to the right in the panels, with **a** being close to the burner and **b**, **c** and **d** being located progressively downstream of **a**. Particles can be observed as denser fields that are passing the ports.

4.2.2 Diode laser and laser-induced incandescence

The in-flame soot volume fraction was estimated in Paper IV using a diode laser together with a Laser-Induced Incandescence (LII) system. The 808-nm (λ_d) diode laser was used to measure the extinction through the flame, measuring the signal going through the furnace, and this was used to calibrate the LII-signal. The LII-signal was captured using an intensified CCD camera, capturing 2D images from the 1064-nm Nd:YAG laser sheet introduced to the furnace. The soot particles absorb the laser energy, are rapidly heated to their sublimation temperatures in the range of 3500–4000 K, and start to emit black-body radiation. Thus, the particle temperature is much higher than that of the surroundings at this point, and the emitted radiation, i.e., the incandescence, is easily captured [105] by an intensified CCD camera placed perpendicular to the laser sheet. A simplified schematic of the laser and detector arrangement is shown in Figure 27. The two lasers were directed to pass through the same part of the flame, although the measurements were not performed simultaneously, so as to avoid signal interference.

The soot volume fraction is estimated by converting the LII-signal to quantitative 2D soot volume fractions [57], [106]. The average soot volume fraction is calculated over an absorbing path length L where soot particles are present, estimated from the two-dimensional images, using the incident intensity, I_0, and transmitted intensity, I, as follows:

$$f_{\mathrm{v}} = \frac{\lambda_d}{6\pi L E(m_\lambda)} \ln\left(\frac{I_o}{I}\right) \tag{51}$$

where f_{v} is the volume fraction of soot, λ_d is the wavelength of the diode laser, and $E(m_\lambda)$ is a function of the complex refractive index of soot m_λ [see Eqns. (12) and (14)]. An average of the LII-signal along the diameter of the flame is calculated, and given that the soot volume fraction is approximately proportional to the LII-signal [107], the soot volume fraction in each pixel of the 2D image can be estimated. The value used for $E(m_\lambda)$ will have a great impact on the soot volume fraction [59], as they are inversely proportional to each other. However, the value of $E(m_\lambda)$ varies in the literature, see e.g. [18], [67], and should be selected with care.

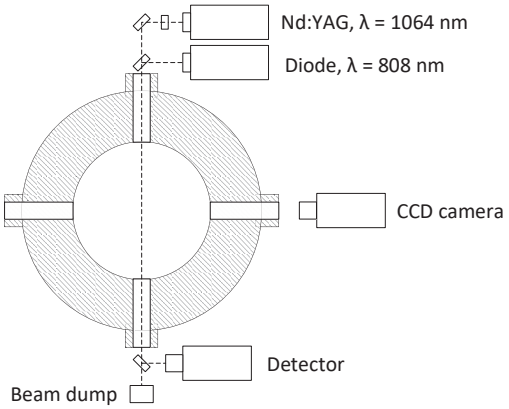

Figure 27. Simplified schematic of the laser setup used in the Chalmers 100-kW_{th} oxy-fuel test rig with a diode laser and the LII system.

4.2.3 Ellipsoidal radiometer

The incident radiative heat flux to the furnace wall can be measured in a non-intrusive manner if it is placed in line with the furnace inner wall. In this work, the incident radiative heat flux was measured using an ellipsoidal radiometer that was placed in the tip of a probe, with a view angle close to that of a hemisphere (Figure 28). The measured voltage signal corresponds to the incident radiative heat flux, and the radiative heat transferred from the whole furnace to a small point on the furnace wall is measured. The data acquired by this instrument were used for Papers I and II.

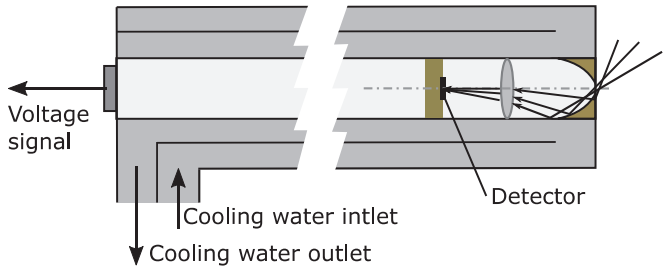

Figure 28. Schematic of the ellipsoidal radiometer used for measuring the incident radiative heat flux to the furnace wall.

5. Experimental Furnaces

The experiments and measurements presented in this thesis were conducted in one industrial and three experimental furnaces. While three of the furnaces are cylindrical, they are of different dimensions, are operated differently, and are used for different purposes. The furnaces used were: a 580-kW_{th} experimental combustion furnace (located at LKAB in Luleå, Sweden); a 37-MW_{th} industrial rotary kiln (located at LKAB in Kiruna, Sweden); a 100-kW_{th} oxy-fuel test rig (located at Chalmers University of Technology in Gothenburg, Sweden); and a 1.5-MW_{th} square horizontal furnace (located at the University of Utah in Salt Lake City, UT, USA).

5.1 Experimental Combustion Furnace

Experiments to examine the radiative heat transfer in rotary kilns were conducted in a cylindrical and refractory lined test furnace (Figure 29 b), which is referred to as the Experimental Combustion Furnace (ECF). The ECF was constructed as a down-scaled version of a full-scale rotary kiln used in a grate-kiln process for iron ore pelletizing by LKAB, using constant velocity scaling. The furnace is tilted at an angle of 3° from the horizontal line, with the burner positioned at the lower end and the burner axis placed in line with the furnace axis. The burner has six registers for primary air and fuel [108]. During the experiments presented in this thesis, the burner was fed solid fuels, either pure coal or co-firing with coal and biomass, corresponding to a thermal input of 580 kW_{th}. Large volumes of preheated secondary air (about 2,300 Nm^3/h) were introduced into two large honeycomb registers, one situated above and one situated below the burner, as described previously [23], according to Figure 29a. In the first section of the test furnace, lying closest to and downstream of the burner, 13 measurement ports are located along the axis of the furnace, allowing for in-flame measurements. The ports are labeled MH0–MH12, and on the opposite side to the ports, quartz windows are placed to act as cold backgrounds when performing radiative intensity measurements. The first section has an inner diameter of 650 mm, widening to 800 mm in the second section. To resemble the pellet bed heat sink in the full-scale process, a cooling system was installed at the bottom of the furnace. Further details of the furnace and the different fuel cases tested in the furnace can be found in Paper I, and these elements are used for Papers I–III.

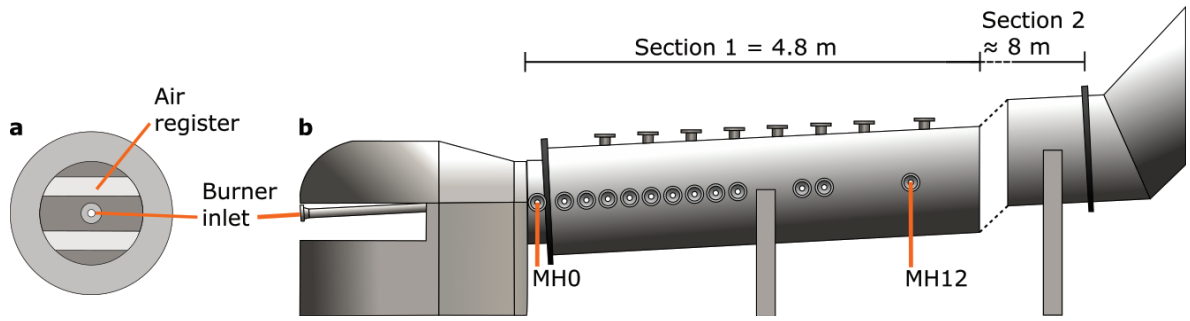

Figure 29. Schematic of the ECF used to study radiative heat transfer in the rotary kiln process. The thermal input to the burner is 580 kW_{th} and the burner is placed to the left in the figure. Measurement ports that allow in-flame measurements are shown along the axis of the furnace (MH0–MH12).

A similar test furnace was used during an earlier experimental campaign conducted by Bäckström et al. [23] in 2013. The two campaigns differ in that in the earlier campaign; (i) the test furnace axis was horizontally lined with an inner furnace diameter of 800 mm along the whole axis; (ii) the thermal input was lower at 400 kW_{th}; and (iii) there was no cooling section at the bottom of the bed. Moreover, it had six fewer measurement ports available. Some of these measurements are used in Paper III. In both campaigns, the test furnace was stationary and there was no bed material.

5.2 Kiruna Kulsinterverk 2

A full-scale rotary kiln should perhaps not be considered an experimental furnace, although it is possible to perform some measurements also at an industrial scale. The rotary kiln studied in this work, called the Kiruna Kulsinterverk 2 (KK2), is approximately 34 m long (L) and has an average inner radius (R) of about 2.7 m. The kiln has an inclination (β) of about 3.5° and an angular rotation speed (ω) of about 1.4 rpm, causing the pellets to mix and move forward in the kiln. The thermal input is about 40 MW_{th}, dependent on the production rate, which varies but is annually about 4 million tonnes [37]. The bed material constitutes approximately 10% of the total kiln volume, and the jet-like coal flame has occasionally been observed to reach almost the full length of the kiln. The burner is regularly fueled with coal, although occasionally, and at start-up, oil is used instead. Figure 30 shows a schematic of the rotary kiln.

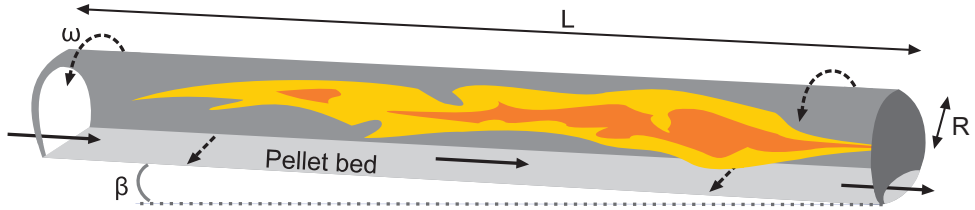

Figure 30. Schematic of an industrial rotary kiln used for iron ore pelletizing. As the kiln rotates, the iron ore pellet bed migrates towards the lower end of the kiln where the burner is positioned.

Performing probing measurements within the kiln would obviously be very challenging since the kiln is rotating, and no measurement ports are available today. At a position close to the burner, it is however, possible to visually study the inside of the kiln, e.g. using an infrared camera, observing the temperature of the different surfaces (see Section 2.1.2). From the process control, operational data of the process was however available. Such measurements and data were used for paper III.

5.3 Oxy-Fuel Test Rig

Soot formation and the radiative heat transfer from soot particles were studied in the Chalmers 100-kW_{th} oxy-fuel test rig. A schematic of the down-fired, cylindrical furnace is presented in Figure 31a, and the furnace can be used to study both gaseous and solid fuels. The inner diameter and height of the furnace are 800 mm and 2400 mm, respectively. A swirl burner is mounted on top, with the fuel introduced at the center of the burner and air being introduced through two annular swirling registers with swirl angles of 45° and 15° for the primary and

secondary air registers, respectively, as shown in Figure 31b. A refractory cone is positioned close to the burner to stabilize the flame. A more detailed description of the burner can be found in the paper of Hjärtstam et al. [109]. The amount of oxidant flowing through each register can be altered by closing or opening a valve to either register. The four water-cooled tubes present in the furnace cool the flame to temperatures close to those seen in more conventional combustion processes. Measurement ports (M) are located at different axial distances from the burner, or levels, allowing for in-flame probing, as well as access for the optical measurements. Four measurement ports are available at each level, equally distributed around the furnace circumference. Quartz windows may be placed in an opposite port for visual observation and to act as a cold background when performing measurements of radiative intensity. The test rig can be operated in oxy-fuel mode through recirculation of the flue gases and the addition of oxygen. Injections of different compounds to the oxidant, such as NO or SO_2, or the addition of water solutions of salts to the flame through a port directed to a position close to the burner (MS) are also possible, allowing studies of the effects of such additives. This furnace was studied in Papers IV and V.

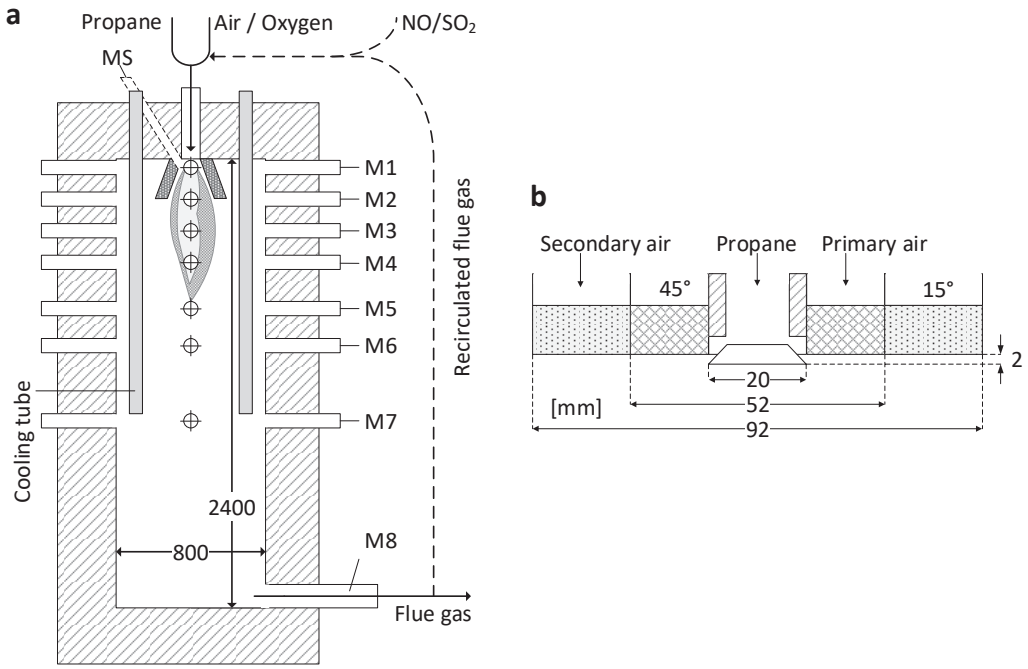

Figure 31. a Schematic of the cylindrical Chalmers 100-kW_{th} oxy-fuel test rig. Measurement ports (M) are located along the axis of the furnace. **b**, Cross-section of the burner showing the propane flow at the center of the burner and the primary and secondary air registers with their respective swirl angles. Dimensions are given in millimeters.

5.4 L1500 Multifuel Furnace

At the University of Utah, a 1.5-MW_{th} furnace, referred to as the L1500, has been used in this work for studies of coal-firing and co-firing of coal and biomass flames. The L1500 is a horizontally fired furnace with a quadratic inner cross-section of 1.1×1.1 m and a total length of almost 12.5 m [110] (Figure 32). The burner is a dual concentric swirl burner, designed to provide good flame stability. Cooling panels available within the furnace allow for adjustment of the flue gas temperature profile and the maintenance of realistic boiler temperature profiles

[111]. Several measurement ports are available along the furnace axis for probing or visually observing the flame, with the possibility of using cold backgrounds in a manner similar to that described for the ECF and 100-kW_{th} furnaces. The test facility has been used in several studies, to examine, for example NO_x-emissions, particulate control, burner development, retrofitting coal burners [111], and co-firing with coal and biomass [110].

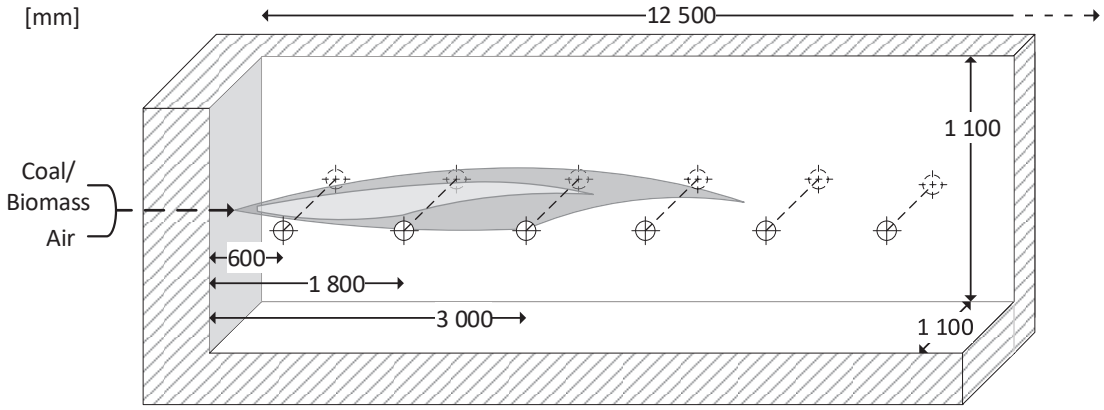

Figure 32. Schematic of the first few meters of the L1500 multifuel furnace, which was a thermal input of 1.5-MW_{th}. The distance from the burner for the first three ports are shown.

6. Selected Results and Discussion

The main results of this thesis are from the experimental studies and the modeling of the radiative intensity and the radiative heat flux in different furnaces. The modeled total radiative intensity and incident radiative heat flux correspond to the intensity measured with the narrow angle radiometer and the heat flux measured using the ellipsoidal radiometer (see Chapter 4), respectively.

The radiative heat transfer properties of the rotary kiln process (for iron ore pelletizing) were studied in two measurement campaigns using the ECF, as described in Chapters 2 and 5. This thesis includes modeling results that are based on the measurements from both campaigns. The measurements acquired during the latter campaign in 2015 have been evaluated and modeled extensively in Paper I, focusing on the cases using the co-firing burner configuration. Since the quality of the produced iron ore pellets is largely affected by the radiative heat transfer from the flame, the radiative heat flux directed to the wall of the furnace is an important parameter to study and understand, as further examined in Paper II, applying the DOM. Using measurements from both campaigns, a full-scale rotary kiln was modeled, and the heat transfer mechanisms within the kiln are examined in Paper III.

The soot volume fractions in various propane flames were studied during two measurement campaigns included in this thesis (see Chapter 2). Both campaigns were conducted in the Chalmers 100-kW_{th} oxy-fuel test rig, as described in Chapter 5, using the optical measurement technique presented in Paper IV and the gas extraction measurements described in Paper V (see Chapter 4).

6.1 Pilot-Scale Rotary Kiln

During the 2015 campaign in the ECF, measurements of the radiative intensity using the co-firing burner were conducted at three of the measurement ports, MH1, MH3, and MH7, which are axially positioned in relation to the burner according to Figure 29. The ports were positioned 433, 933 and 1,933 mm from the burner, respectively, and the measured radiative intensities are shown in Figure 33 for the RC, BA, and BB co-firing cases, using 30% biomass based on the lower heating value. The NAR probe enters the furnace at the 0-mm position, recording high radiative intensities, as the entire furnace diameter, with high concentrations of particles and hot gases, is in the line-of-sight of the detector. When the probe was traversed along the furnace diameter, the measured radiative intensity decreased, along with the number of particles in the line-of-sight of the probe. At the 650-mm position, at the opposite wall, the intensity decreased to values close to zero due to the cold background of the quartz window. Comparing the measurements for the three fuel combinations tested, it is evident that the differences are minor for the RC case and the co-firing BA case, while the co-firing BB case gives somewhat lower values at the different ports. The results imply that co-firing of coal and biomass could be used in the rotary kiln.

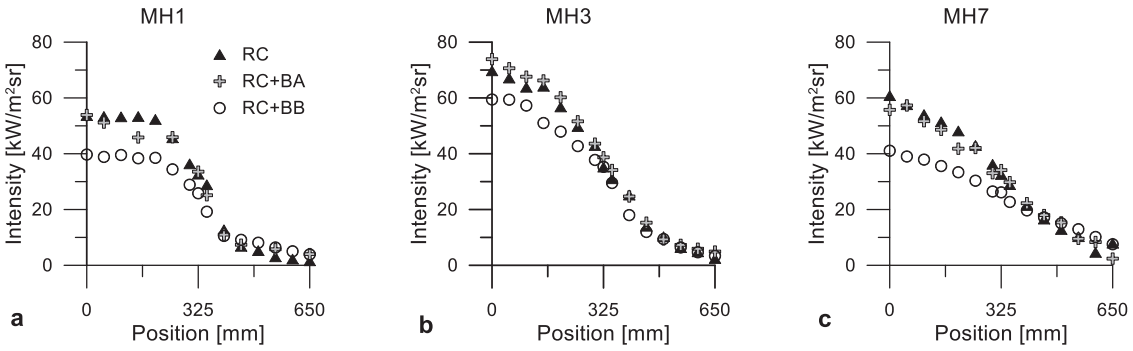

Figure 33. Measured radiative intensities at measurement ports **a** MH1, **b** MH3 and **c** MH7, for the three fuel combinations tested in Paper I. RC, Reference coal; BA, biomass A (wood treated with steam explosion); BB, biomass B (pelletized and ground wood).

Using measurements of temperature, gas composition, and particle concentration as input data to the DTM, the total radiative intensity was modeled in Paper I for the different co-firing cases. The measured and modeled radiative intensities along the furnace diameter are shown in Figure 34 for the BA co-firing case. A comparison of the modeled contributions from the gases and particles to the total radiative intensity reveals that particle radiation (dashed line) predominates, and that the fraction of the radiative intensity that arises from the gases (dashed-dotted line) is small for all the cases and ports. Comparing the axial ports, the measured radiative intensity appears to increase when moving from port MH1 to MH3, but decreases once again when moving downstream to port MH7. This is probably an effect of cold fuel particles that had not yet been ignited at port MH1, while a greater proportion of the particles had been ignited at port MH3, resulting in higher flame temperatures and radiative intensities. At port MH7, the particle concentration is lower due to the progression of the combustion, and the radiative contribution from particle emission is lower. The radial gradient of the radiative intensity plots at the central position decreases along the furnace axis, moving downstream from port MH1 to MH7, as the particles become more evenly distributed along the furnace radius. The model appears to underestimate the radiative intensities at positions close to the entrance of port MH3, probably due to the temperatures or the particle concentrations being too low at these positions. However, the overall agreement observed between the measured and modeled radiative intensity is satisfactory for the different ports and cases. This implies that the measurements of temperature and particle concentrations carried out in this campaign were largely accurate and represented an improvement over the earlier campaign.

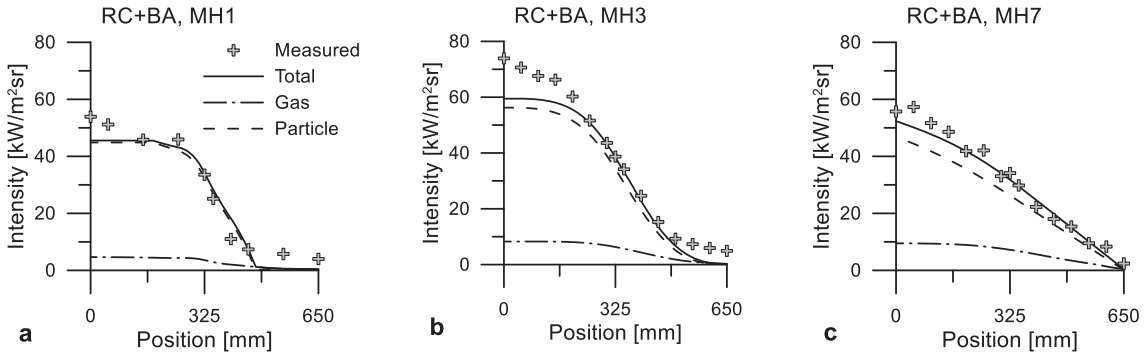

Figure 34. Measured and modeled radiative intensities for the co-firing case of the reference coal (RC) and biomass A (BA), as obtained during the ECF 2015 measurement campaign at ports: **a**, MH1; **b**, MH3; and **c**, MH7.

During the 2015 campaign, the radiative heat flux to the inner wall of the furnace was measured for ports MH0, MH1, MH3, and MH7 for the different studied co-firing cases using the ellipsoidal radiometer, as shown in Figure 35. Port MH0 is positioned closest to the burner. Comparing the different fuel combinations, only minor differences were observed between the measurements for all the ports. This outcome raises the possibility of using co-firing in the full-scale rotary kiln with respect to the heat transfer conditions, as the radiative heat transfer profile appears to be similar for all three cases.

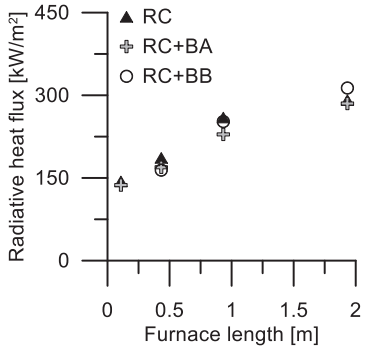

Figure 35. Measured incident radiative heat fluxes for the different fuels and measurement ports, reference coal (RC), co-firing with biomass A (BA), wood treated with steam explosion, and co-firing with biomass B (BB), using pelletized and ground wood.

The RC data were also examined in Paper II, modeling the incident heat flux to the furnace wall using the DOM for the first section of the ECF, which is 4.8 m in length according to Figure 29. Measurement profiles were introduced to the model, taken at axial locations corresponding to the measurement ports, and averaging was employed for the cells between the ports, using a cell resolution of 30×60×100. In a first modeling attempt, the incident radiative heat flux was calculated for wall temperatures, as estimated using the infrared camera (Figure 36a). The model appears to overestimate the radiative heat flux for the downstream port MH7. In a second attempt, the wall temperature was instead set so as to be equal to the gas temperature closest to the wall, as measured with a suction pyrometer. The result, shown in Figure 36b, displays better agreement. In a third modeling attempt, the wall temperature was calculated from an energy balance of the incident and emitted radiation and outer heat loss according to Eqns. (40) and (49), as shown in Figure 36c, with good agreement.

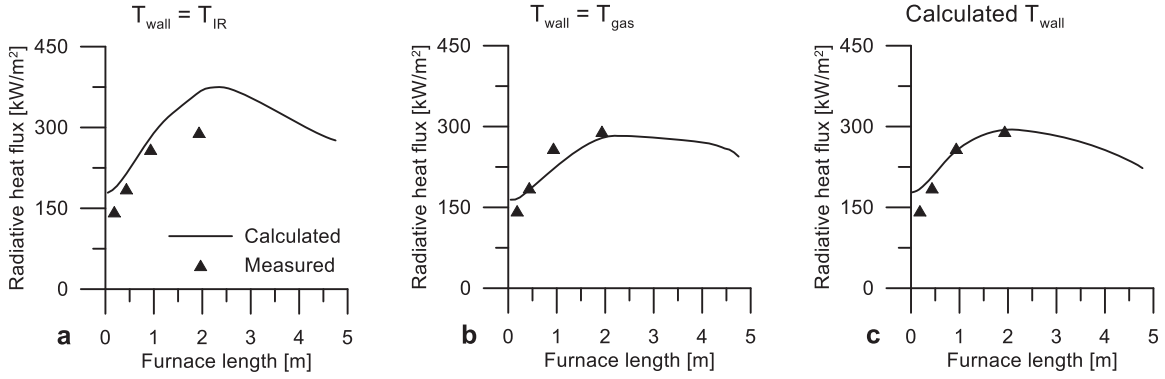

Figure 36. Measured and modeled incident radiative heat fluxes for the RC case in the co-firing burner using the discrete ordinates method. The wall temperature was set based on data from: **a**, the IR-camera; **b**, the gas temperature close to the wall; and **c**, calculated from an energy balance.

6.2 Industrial Full-Scale Rotary Kiln

Measurement data gathered during the two ECF campaigns were used to model a full-scale industrial rotary kiln. Employed were two different flames, a coal flame (2015) and an oil flame (2013), resembling the combustion conditions in the KK2 and using constant velocity scaling. Using the developed DOM tool, the modeling included radiative, conductive, and convective heat transfers, as well as the movement and mixing of the reactive bed material and the rotation of the wall, as described in Section 3.3. After feeding a bed material into the kiln, the bed and wall temperatures are calculated as the bed travels through the kiln. Temperature maps of the modeled inner wall and bed temperature are shown in Figure 37 for the coal (**a**) and oil (**b**) flames respectively. The bed temperature is observed to increase in the axial direction as the bed travels through the kiln towards the burner position (L-position). The wall temperature increases in the angular direction as it is heated from the flame and the wall rotates, as a wall cell is transported from $\psi = 0$ towards the point where it meets the bed, due to the rotation of the wall. While under the bed material, the wall is cooled as heat is transferred to the pellets until $\psi = 2\pi$, at which point the wall resurfaces and appears at $\psi = 0$, and is heated by the flame once again. Since the bed material in the surface layer mixes while the wall rotates, temperature profiles in the angular direction are not as obvious for the bed material. The oil flame is shorter but with a higher peak temperature, which is reflected in the higher wall peak temperature closer to the burner, whereas the outlet gas temperature is cooler than for the coal flame, also causing a cooler bed feed to the kiln. However, the beds appear to leave the kiln at similar temperatures, albeit slightly cooler for the oil case, meaning that more heat is absorbed by the bed closer to the burner for the oil flame.

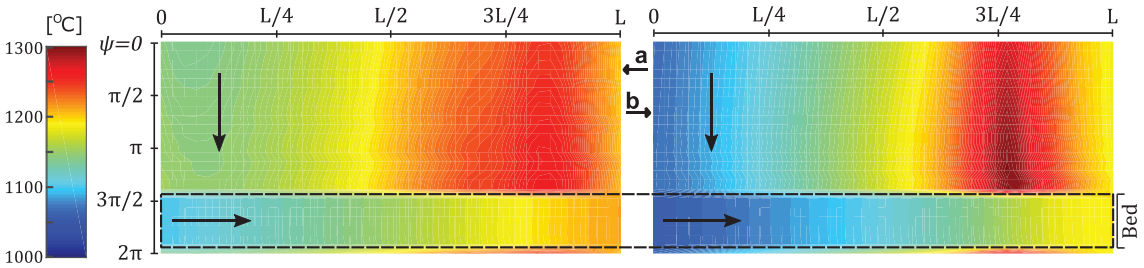

Figure 37. Surface temperatures of the inner wall for a coal flame (**a**) and an oil flame (**b**). The angular positions of the bed, and the movement of the bed and wall are indicated.

The modeled (mo) temperatures were compared to the measured (me) temperatures, and a temperature error was estimated according to Eqn. (52).

$$T_E = \frac{T_{me} - T_{mo}}{T_{me}} * 100 \tag{52}$$

The temperature errors between the measured and modeled product bed temperatures were 0.7% and 2.4% for the coal flame and oil flame, respectively. This provides confidence that the modeling tool could be considered as rather predictive.

The different net contributions from radiative, conductive, and convective heat transfers to and/or from the bed material were studied along the rotary kiln axis, as shown in Figure 38. Radiative heat transfer predominates along almost the entirety of the axis of the rotary kiln. However, close to the burner, at the L-position, convective heat transfer is the dominant heat

transfer mechanism. At this position, the bed material has reached high temperatures and it has travelled past the position of the maximum flame temperature, and the gas coming from the cooler section is relatively cool, resulting in an effective, convective transfer of heat. It should be noted, however, that the total net heat transfer occurring at this position is relatively small in comparison to the total heat transfer throughout the kiln length. The overall heat transfer due to radiation is about 81% and 84% for the coal and oil flames, respectively, clearly showing the importance of an accurate radiative heat transfer model while working with rotary kilns.

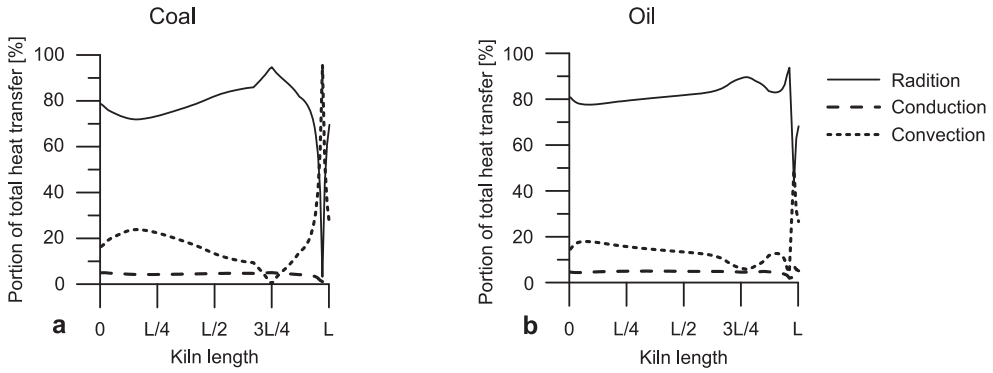

Figure 38. The contributions of the different heat transfer mechanisms of radiation, conduction, and convection to the bed material along the rotary kiln axis, for the coal flame and oil flame cases.

6.3 Co-Firing in the L1500 Multifuel Furnace

During the measurement campaign conducted in 2018 in the L1500 multifuel furnace, co-firing of a fossil coal and torrefied biomass was examined, using 15% biomass. The measured radiative intensities and incident heat fluxes to the inner wall of the furnace are shown in Figure 39. The radiative intensities measured at port 3 (Figure 39b) appear to be similar for the two cases, so the radiative intensity profile is not affected by the biomass exchange. At port 2 (Figure 39a), the maximum measured radiative intensities appear to be different for the two cases. Considering the small difference in incident heat flux (Figure 39c) between the two cases, the difference noted at port 2 may be due to a miss-directed NAR during the measurements. While the cold background was targeted, at positions close to the entrance port, it appears that the NAR was directed towards the opposite wall instead. Since the radial heat profiles are similar for the two cases, this result raises the possibility of using co-firing in boilers.

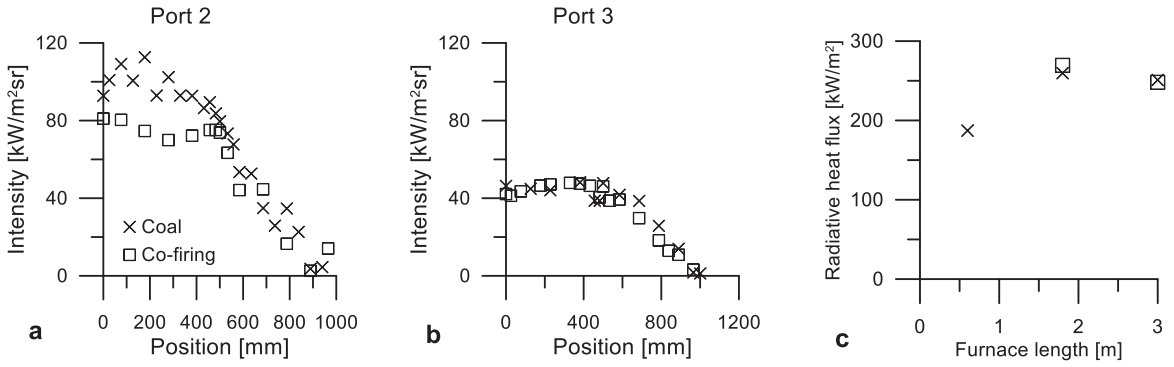

Figure 39. Measured radiative intensities at ports 2 (**a**), 1800 mm from the burner, and 3 (**b**), 3000 mm from the burner, as well as the incident radiative heat fluxes along the furnace axis (**c**) in the L1500 multifuel furnace.

6.4 Radiative Properties of Soot Particles

Two air/propane flames were studied in the 2014 campaign for an open and closed primary air register, respectively, as described in Paper V. The former flame appeared to have very few soot particles (non-sooty); their numbers were lower than those reported previously in the work of Andersson et al. [26], although the conditions used in these studies were similar. The discrepancy was likely due to the installation of a refractory burner quarl in the period between the two campaigns. The latter flame was, in contrast, considered to be sooty and the soot volume fraction was estimated using a SMPS to be about 65 ppb at port M3 (see Figure 31). Figure 40 shows the measured and modeled radiative intensities, including the measured soot volume fraction for the case with a closed primary air valve, and as can be observed, including the soot particles the modeled intensities match well with the measurements. The soot volume fraction obtained with the SMPS was considered to be reliable.

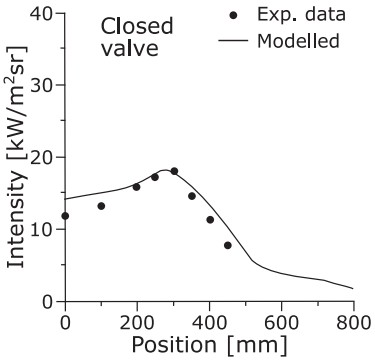

Figure 40. Measured and modeled radiative intensities for a closed primary air valve, including the soot particles present (Paper V) [56].

Spectral absorption and scattering coefficients were measured for the soot particles using the PASS-3 instrument. Figure 41 shows the measured spectral absorption coefficients (circles) for three wavenumbers at port M3 for the sooty flame. Using a least-square method of the soot volume fraction, the measurements were compared to spectral expressions found in the literature [15]–[18]. For all four models tested, there was generally good agreement between the trends of the measured and modeled absorption coefficients. The calculated values of the soot volume fraction from the PASS-3 were, however, lower than what was measured with the SMPS. Though, it should be kept in mind that there are more uncertainties using the PASS-3 instrument to calculate the soot volume fraction.

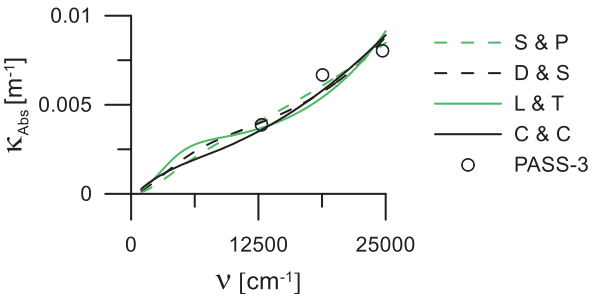

Figure 41. Measured values at port M3 for the absorption coefficients of the soot particles, using the PASS-3 instrument, as compared to functions previously published by Stull and Plass (S & P) [15], Dalzell and Sarofim (D & S) [16], Lee and Tien (L & T) [17], and Chang and Charalampopoulos (C & C) [18].

In the latter campaign in 2016, the soot volume fraction was measured using an extinction laser together with the LII system, for air, oxygen-enriched air, and oxy-fuel flames, as described in Paper IV. With the LII and the CCD camera, it was possible to capture 2D images of the soot volume fraction along the diameter in the central part of the furnace, as shown in Figure 42 for an air (21% O_2) flame and an oxygen-enriched air flame with an oxygen concentration of 30%. The contrast in the figure is saturated to show more clearly the presence of soot particles. The soot volume fraction ranges from black to white, reflecting the LII-signal in each pixel, for a laser sheet with a height of 45 mm.

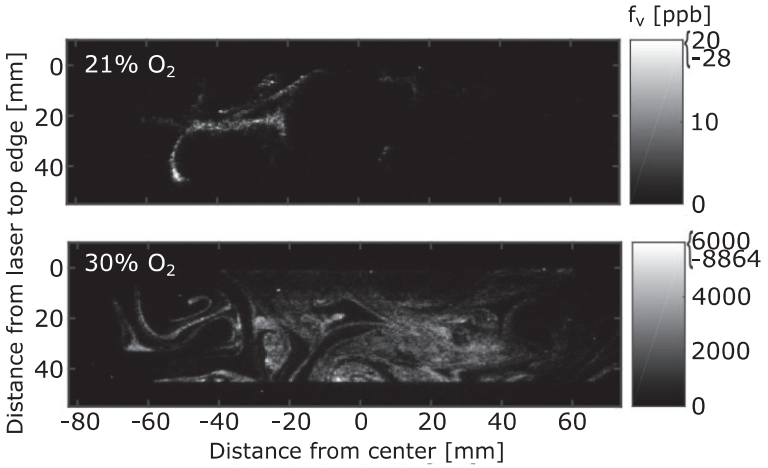

Figure 42. Photograph of the soot appearance captured with a CCD camera for an air flame and an oxygen-enriched air flame with 30% oxygen. The brightness of each pixel is related to the magnitude of the soot volume fraction.

The measured soot volume fractions from the different air (A), oxygen-enriched air (E), and oxy-fuel (OF) flames at port M3 are shown in Figure 43. Two different air flames were tested using an open (A1) and a closed (A2) primary air register. With an open primary air register, the air was enriched with oxygen to generate oxygen concentrations of 25% (E25), 27% (E27), and 30% (E30). By recirculating of flue gases and adding oxygen, oxy-fuel flames with oxygen concentrations of 30% (OF30), 35% (OF35), 40% (OF40), and 42% (OF42) were achieved. The cross-section for which measurements were possible was limited by the height of the laser sheet and the width of the measurement port. The central axis of the furnace is located at the 0-mm position in Figure 43. The results show that there are significant increases in soot formation from the oxygen-enriched air and oxy-fuel flames as the oxygen concentration in the oxidant is increased above a certain threshold value. Comparing the oxygen-enriched cases with the oxy-fuel cases, it is clear that a distinct shift in soot formation occurs at higher oxygen concentrations for the oxy-fuel flames, i.e., 27% oxygen compared to 40% oxygen. The increased soot volume fraction attributed to both thermal and chemical effects. As the oxygen concentration is increased, the peak temperature is increased, and the gas volume flow is reduced, which affects the mixing. In the oxy-fuel cases, soot formation is suppressed by the increased concentration of carbon dioxide, which reduces the flame temperature.

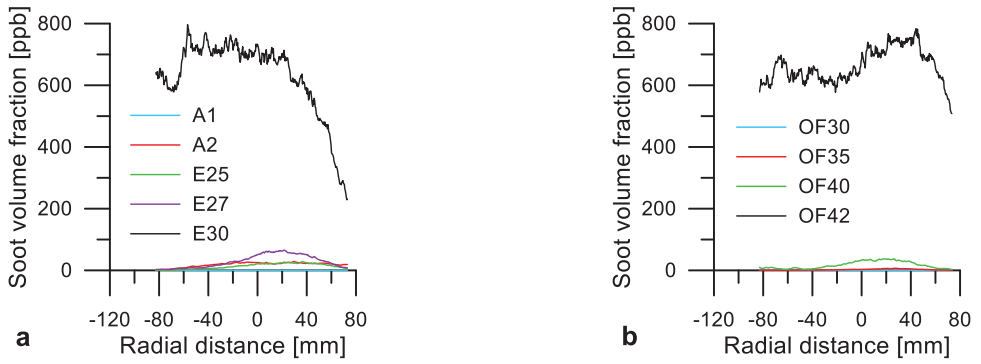

Figure 43. The measured soot volume fractions for: **a**, air (A) and oxygen-enriched air (E) flames; and **b**, oxy-fuel (OF) flames, using a diode laser and a LII system. A1 and A2 correspond to air flames with a fully open and a fully closed primary air register, respectively. The numbers following the E and OF designations are the respective oxygen concentrations in the oxidant.

In the cases with higher oxygen concentrations, the measured radiative intensities were substantially higher. This may be due to higher flame temperatures or an increased soot volume fraction, which is in line with the measurements obtained using the LII system. Together with the soot volume fractions, measurements of temperature and gas composition were performed and thereafter used to model the radiative intensity using the DTM for air/propane and oxygen-enriched air/propane flames. The modeled intensities agreed well for the different flames with <30% oxygen in the oxidant. Figure 44a shows the measured and modeled radiative intensities for the A2 flame, with values comparable to those in Figure 40. For the E30 flame, some of the measurements are more uncertain as the heavy particle loads clogged the suction pyrometer, resulting in comparably low temperatures measured at positions close to the furnace center, and further temperature measurements had to be canceled. Figure 44b shows, however, the measured and modeled radiative intensities for the E30 flame, using the available measurement data. Comparing the two flames, the radiative intensity level is clearly increased with the oxygen concentration and, as can be observed, the largest contributor to the total radiative intensity has switched from gas to soot particles.

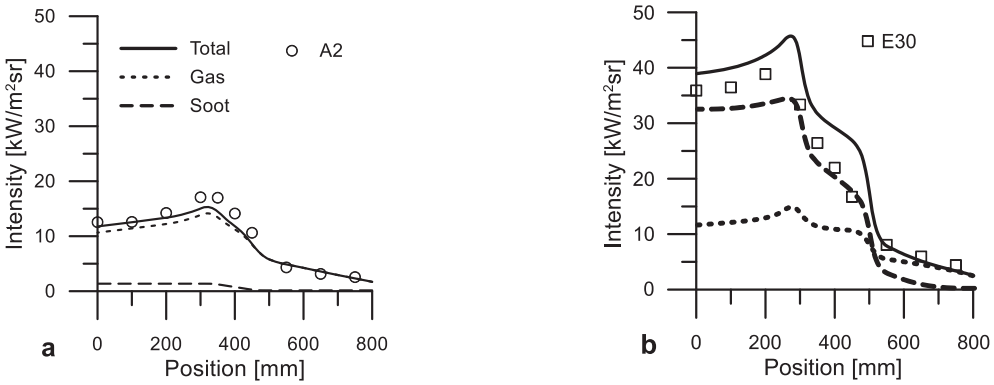

Figure 44. Measured and modeled radiative intensities for propane flames with **a**, air as the oxidant and with a closed primary air register (A2); and **b**, 30% oxygen in the oxygen-enriched air used as the oxidant (E30). The gas and soot particle contributions to the total radiative intensities are included.

7. Conclusions

The work presented in this PhD thesis was designed to examine the radiative heat transfer conditions and phenomena in, mainly, cylindrical furnaces. The combustion of three different co-firing cases using a reference coal, and co-firing with two different biomasses, using 30% biomass, were evaluated in Paper I. Comparing the measurements of the radiative heat fluxes and intensities, the overall heat transfer conditions appears similar for the cases. The similarities indicate that it is possible to use biomass for co-firing in a rotary kiln, used for iron ore pellet production without significantly affecting the radiative heat transfer and substantially lowering the carbon dioxide emissions. Using the discrete transfer model, the radiative intensities were modeled for the three cases and showed good agreement with the measurements, implying that the measurements were performed in an accurate way during the campaign. Furthermore, it is shown that particle radiation in the flame is the main contributor to the total radiative intensity from the flame. A modeling tool that applies a discrete ordinates method was developed and used in Paper II, to study the radiative intensity and heat flux to the wall of the ECF. The heat flux to the wall is shown to be sensitive to the wall temperature, although the model exhibits satisfactory predictive qualities for the incident radiative heat flux and wall temperatures. Overall, the tool appears promising for describing the radiative heat transfer in a full-scale rotary kiln process. In Paper III, the modeling tool is further developed for the heat treatment of a bed material, including convective and conductive heat transfers. The bed heat treatment from two flames in a full-scale rotary kiln were modeled, and the bed product temperature was compared to actual measurements, with a reasonable level of agreement being noted. It is further shown that more than 80% of the total heat transfer to the bed material is due to radiative heat transfer. However, to validate further the model, the collection of more full-scale data from an industrial rotary kiln is desirable, together with additional full-scale experiments.

Moreover, the radiative properties of soot particles and their contribution to the total radiative heat transfer were studied for various propane flames in the oxy-fuel test rig, with assessment of the soot volume fractions using two different measurement techniques. By closing the primary air register to the burner, increased soot production could be observed for a propane/air flame using both the intrusive SMPS (Paper V) and non-intrusive LII (Paper IV) measurement techniques. The soot formation was observed to increase in line with the oxygen concentration, using the oxygen-enriched air or oxy-fuel mode, at different oxygen concentrations, while retaining the stoichiometry. Dramatic increases in soot formation were observed, in excess of 27% and 40%, for the oxygen-enriched air and oxy-fuel flames, respectively, increasing the soot volume fractions more than 14-fold compared to the lower oxygen concentrations. These results suggest the possibility to increase the intermediate soot concentration and, thereby, promote the radiative heat transfer in furnaces. The radiative intensity was modeled using the discrete transfer model, and the values correspond well with the measurements made, indicating successful measurements of the soot volume fractions. The PASS-3 instrument was used to study the radiative properties of the soot particles and the absorption coefficients derived from the measurements showed trends towards good agreement with the models of the complex index of refraction used in the Rayleigh theory.

8. Suggestions for Future Work

During the experimental campaigns, severe problems were occasionally encountered with particle sampling. In flames with heavy particle loads at the sampling positions, the particles may clog the measurement probe, resulting in measurement errors. For co-firing flames, these problems are exacerbated by the presence of condensing tars. Therefore, it is of interest to continue the work of developing and refining measurement techniques for particle extraction. Furthermore, as the sampling process is time-consuming, it is desirable to make the sampling process more time-efficient or to allow for longer sampling times. In the context of particle sampling, it is important to describe the radiative scattering in an appropriate way for coal-fired and co-firing flames, as has been addressed in this work. Isotropic scattering is a convenient simplification applied in the radiative heat transfer modeling, and for a moderate-temperature furnace wall, the error appears to be small. However, the impact of in-scattering is much more significant when the furnace wall is hot, e.g., in applications such as the rotary kiln. It is, therefore, important to continue to develop the modeling, as well as to study experimentally the radiative scattering that occurs in combustion processes in the presence of particles.

To gain further insights into the heat transfer that occurs in the full-scale industrial rotary kiln, the performance of measurements within the kiln is desirable. As mentioned earlier, the dimensions of the kiln and the rotation of the wall complicate such measurements. However, a technique that could give access for measurements of the gas composition and temperatures in the kiln freeboard is LIDAR, operated from positions close to either the burner or the pellet feeding. LIDAR is an optical measurement technique that has the advantage that the light source and detector can be placed at the same position. In addition, performing experiments with co-firing of coal and biomass in a full-scale rotary kiln during the production process would be very valuable and interesting.

The rotary kiln model could also be useful in the development of rotary kilns other than those designed for iron ore pelletizing, such as for cement production, lime regeneration or alumina melting. However, an effort must be made to treat each bed type in an appropriate way. Moreover, the modeling tool applying the discrete ordinates method could be improved further by including a suitable combustion model.

In recent times, discussions as to how to reduce the greenhouse gas emissions from industries that are heavy emitters, such as iron ore pelletizing and cement production, have started to include electrification. An interesting alternative for rotary kilns is to substitute coal burners with plasma torches, for which the model could prove useful. Plasma temperatures are, however, much higher than those found in suspension-fired systems and experimental as well as modeling work would be required before implementing plasma torches for industrial production.

It is also probable that industries in the future will have to adapt their production rates for those during which the electricity or energy demand is greater than the supply, on a yearly or even

daily basis. It would, therefore, be interesting to examine the heat treatment of the bed for variations in production rate and process operations, with the focus on radiative heat transfer for transient processes.

Finally, it would be interesting to study more extensively the rapid shifts in soot formation that were observed for the propane flames as the oxygen concentration was increased. Experiments performed to isolate the different contributions to the soot formation from thermal, chemical and mixing effects would be interesting. Also, the soot volume fraction was measured at one axial distance from the burner using the LII system during the latest campaign, and it would be of interest to study how this change along the axis of the furnace.

9.Nomenclature

Abbreviation

2D	two-dimensional
3D	three-dimensional
BA	biomass A, wood treated with steam explosion
BB	biomass B, pelletized and ground wood
BC	biomass C, torrefied wood
C1 – C4	cooler zones
CCD	charge-coupled device camera
CCS	carbon capture and storage
CFD	computational fluid dynamics
CPC	condensation particle counter
DMA	differential mobility analyzer
DOM	discrete ordinates method
DTM	discrete transfer model
erf	error function
ECF	experimental combustion furnace
FTIR	Fourier-transform infrared spectroscopy
G1 – G4	grate zones
IFRF	International Flame Research Foundation
IR	infrared
KK2	Kiruna Kulsinterverk 2
L1500	1.5-MW_{th} multifuel furnace
LII	laser-induced incandescence
LKAB	Luossavaara-Kiirunavaara Aktiebolag
MH1 – MH7	measurement ports
NAR	narrow angle radiometer
Nd:YAG	neodymium-doped yttrium aluminum garnet ($Y_3Al_5O_{12}$) laser
PASS-3	photo-acoustic soot spectrometer with three laser wavelengths
PAH	polycyclic aromatic hydrocarbon
PM	premixed reference coal and biomass A
RC	reference coal
RTE	radiative transfer equation

SC	second coal
SMPS	scanning mobility particle sizer
SNBM	statistical narrow band model
WSGG	weighted-sum-of-gray-gases model

Symbols

a	particle radius [µm]
a_j	weighting factor of gray gas *j* in the WSGG-model [-]
a_n	Mie scattering coefficient [-]
a_0	weighting factor of a clear gas in the WSGG-model [-]
A	area [m^2]
A	air flame [-]
A	cell surface area in radial direction [m^2]
A_{proj}	projected particle surface area [m^2m^{-3}]
b_n	Mie scattering coefficient [-]
B	cell surface area in angular direction [m^2]
c	light velocity [ms^{-1}]
c_{ij}	coefficient in the WSGG-model [-]
C	cell surface area in axial direction [m^2]
C	coefficient in the WSGG-model [-]
C_p	specific heat capacity [$Jkg^{-1}K^{-1}$]
d_k	mean line spacing for a narrow band [cm^{-1}]
d_T	temperature distribution within the thermal penetration depth [-]
D	diameter [m]
E	oxygen-enriched air flame [-]
E	emitted radiation [Wm^{-2}]
E	absorption function [-]
f_{proj}	projected surface area [m^2m^{-3}]
f_v	soot volume fraction [ppb]
F	view factor [-]
G	intensity integrated over all directions [Wm^{-2}]
G	mass flux [m^2s^{-1}]
h	convective heat transfer coefficient [$Wm^{-2}K^{-1}$]
$\hat{\boldsymbol{\imath}}$	unit vector [-]

I	intensity [$Wm^{-2}sr^{-1}$]
$I-II$	cell type [-]
I_ν	spectral intensity [$Wm^{-2}sr^{-1}cm^{-1}$]
I_0	incident intensity [$Wm^{-2}sr^{-1}$]
$\hat{\boldsymbol{j}}$	unit vector [-]
J	radiosity [Wm^{-2}]
k	thermal conductivity [Wm^{-1}]
k_k	ratio of mean line intensity to typical line spacing for a narrow band [cm^{-1}]
k_λ	absorptive index [-]
$\widehat{\boldsymbol{k}}$	unit vector [-]
K	coefficient in the WSGG-model [-]
L	length [m]
m_λ	complex index of refraction [-]
M	measurement port [-]
n	cell node [-]
n	cell number [-]
n	integer [-]
n_{max}	stop criterion used in Mie theory calculations [-]
n_λ	refractive index [-]
N	total cell number in one direction [-]
N	order of the S_N-approximation [-]
OF	oxy-fuel flame [-]
p	probability function [-]
P	total pressure [bar]
q''	heat flux [Wm^{-2}]
Q_{abs}	absorption coefficient [-]
Q_{ext}	extinction coefficient [-]
Q_{sca}	scattering coefficient [-]
r	radius [m]
r	radial distance [m]
R	furnace radius [m]
R_f	flame radius [m]
s	coordinate along a radiative path [-]
$\hat{s}$	unit vector in a given direction [-]
S	total path length [m]

S_l	line strength [-]
S_N	order of discrete ordinates [-]
t	time [s]
T	temperature [K]
V	volume [m^3]
w	weight for a discrete ordinate [sr]
W	transferred heat [J]
x	size parameter [-]
X_c	contact factor [-]
X_{bf}	rotary kiln volume bed portion [-]
X_{bfe}	filling degree error [-]
Y	mole fraction [-]
z	axial distance [m]

Greek symbols

α	absorptivity [-]
α	angular derivative coefficient [-]
β	extinction coefficient [m^{-1}]
β	kiln inclination
γ	mean line half-width [cm^{-1}]
δ	penetration depth [m]
ΔH	heat of reaction [$kJmol^{-1}$]
Δs_{cell}	length of computational cell [m]
$\Delta \nu$	bandwidth [cm^{-1}]
$\Delta \omega$	angle of one cell, in the angular direction, in the DOM [rad]
ε	emissivity [-]
ζ	direction cosine [-]
η	direction cosine [-]
θ	polar angle [rad]
κ	absorption coefficient [cm^{-1}]
κ_ν	spectral absorption coefficient [cm^{-1}]
λ	wavelength [µm]
λ	oxygen-to-fuel ratio [-]
λ_d	diode laser wavelength [µm]

μ	direction cosine [-]
ν	wavenumber [cm^{-1}]
ξ	direction cosine [-]
ρ	reflectivity [-]
ρ	density [kgm^{-3}]
σ	Stefan-Boltzmann constant [$Wm^{-2}K^{-4}$]
$\sigma_{s\nu}$	spectral scattering coefficient [cm^{-1}]
τ	transmissivity [-]
Φ_ν	spectral scattering phase function [sr^{-1}]
ϕ	azimuthal angle [rad]
ψ	rotational angle [rad]
Ω_i	solid angle [sr]
ω	scattering albedo [-]
ω	angle in the angular direction in the DOM [rad]
ω	angular rotation speed [rpm]

Subscripts

abs	absorption
b	bed
b	bottom bed layer
b	black body
c	conduction
c	center
$conv$	convection
cs	surface contact
d	diode laser
E	error
ext	extinction
g	gas
i	cell number
i	inner
i	cosine direction number
i	radial cell number
j	gray-gas number

j	angular cell number
k	narrow-band number
k	axial cell number
m	discrete direction of ray
me	measured
mo	modeled
o	outer
p	particle
P	node point
r	radiation
r	radial position
ref	reference
s	surface bed layer
sca	scattering
tc	thermocouple
tot	total
w	wall
z	axial position
ψ	angular position
∞	far from surface

Dimensionless numbers

Gr	Grashof number
Nu	Nusselt number
Pr	Prandtl number
Ra	Rayleigh number
Re	Reynold number

10. Bibliography

[1] A. A. Boateng, *Rotary Kilns Transport Phenomena and Transport Processes*. Burlington: Butterworth-Heinmann, 2008.

[2] M. F. Modest, *Radiative Heat Transfer*, Third. United States of America: Elsevier, 2013.

[3] J. G. Marakis, C. Papapavlou, and E. Kakaras, "A parametric study of radiative heat transfer in pulverised coal furnaces," *Int. J. Heat Mass Transf.*, vol. 43, no. 16, pp. 2961–2971, 2000.

[4] M. P. Mengüc and R. Viskanta, "A Sensitivity Analysis for Radiative Heat Transfer in a Pulverized Coal-Fired Furnace," *Combust. Sci. Technol.*, vol. 51, pp. 51–74, 1987.

[5] B. W. Butler, M. K. Denison, and B. W. Webb, "Radiation Heat Transfer in a Laboratory-Scale, Pulverized Coal-Fired Reactor," *Exp. Therm. Fluid Sci.*, vol. 9, pp. 69–79, 1994.

[6] R. Viskanta and M. P. Mengüc, "Radiation heat transfer in combustion systems," *Prog. Energy Combust. Sci.*, vol. 13, no. 2, pp. 97–160, 1987.

[7] Z. Guo, C. Lou, Z. Liu, and H. Zhou, "The impact of combustion characteristics and flame structure on soot formation in oxy-enhanced and oxy-fuel diffusion flames," *Sci. China*, vol. 56, no. 7, pp. 1618–1628, 2013.

[8] A. Beltrame, P. Porshnev, W. Merchan-merchan, A. Saveliev, A. Fridman, L. A. Kennedy, O. Petrova, S. Zhdanok, F. Amouri, and O. Charon, "Soot and NO Formation in Methane – Oxygen Enriched Diffusion Flames," *Combust. Flame*, vol. 124, no. 1–2, 2001.

[9] P. Desgroux, A. Faccinetto, X. Mercier, T. Mouton, D. Aubagnac Karkar, and A. El Bakali, "Comparative study of the soot formation process in a 'nucleation' and a 'sooting' low pressure premixed methane flame," *Combust. Flame*, vol. 184, pp. 153–166, 2017.

[10] I. M. Kennedy, "Models of soot formation and oxidation," *Prog. Energy Combust. Sci.*, vol. 23, pp. 95–132, 1997.

[11] L. Wang, D. C. Haworth, S. R. Turns, and M. F. Modest, "Interactions among soot, thermal radiation, and NOx emissions in oxygen-enriched turbulent nonpremixed flames: A computational fluid dynamics modeling study," *Combust. Flame*, vol. 141, no. 1–2, pp. 170–179, 2005.

[12] H. Richter and J. B. Howard, "Formation of polycyclic aromatic hydrocarbons and their growth to soot - a review of chemical reaction pathways," *Prog. Energy Combust. Sci.*, vol. 26, no. 4, pp. 565–608, 2000.

[13] D. X. Du, R. L. Axelbaum, and C. K. Law, "The Influence of Carbon Dioxide and Oxygen as Additives on Soot Formation in Diffusion Flames," *Twenty-Third Symp. Combust.*, pp. 1501–1507, 1990.

[14] K. T. Kang, J. Y. Hwang, S. H. Chung, and W. Lee, “Soot zone structure and sooting limit in diffusion flames: Comparison of counterflow and co-flow flames,” *Combust. Flame*, vol. 109, no. 1–2, pp. 266–281, 1997.

[15] V. R. Stull and G. N. Plass, “Emissivity of Dispersed Carbon Particles,” *J. Opt. Soc. Am.*, vol. 50, no. 2, pp. 121–129, 1960.

[16] W. H. Dalzell and A. F. Sarofim, “Optical Constants of Soot and Their Application to Heat-Flux Calculations,” *J. Heat Transfer*, vol. 91, pp. 100–104, 1969.

[17] S. C. Lee and C. . Tien, “Optical Constants of Soot in Hydrocarbon Flames,” *Eighteenth Symp. Combust.*, pp. 1159–1166, 1981.

[18] H. Chang and T. T. Charalampopoulos, “Determination of the Wavelength Dependence of Refractive Indices of Flame Soot,” *Proc. R. Soc. A Math. Phys. Eng. Sci.*, vol. 430, no. 1880, pp. 577–591, 1990.

[19] R. S. Mehta, M. F. Modest, and D. C. Haworth, “Radiation characteristics and turbulence–radiation interactions in sooting turbulent jet flames,” *Combust. Theory Model.*, vol. 14, no. 1, pp. 105–124, 2010.

[20] J. Lalak, D. Martyniak, A. Kasprzycka, G. Zurek, W. Moroń, M. Chmielewska, D. Wiacek, and J. Tys, “Comparison of selected parameters of biomass and coal,” *Int. Agrophysics*, vol. 30, no. 4, pp. 475–482, 2016.

[21] L. Baxter, “Biomass-coal co-combustion: Opportunity for affordable renewable energy,” *Fuel*, vol. 84, no. 10, pp. 1295–1302, 2005.

[22] J. Thornock, D. Tovar, D. R. Tree, Y. Xue, and R. Tsiava, “Radiative intensity, no emissions, and burnout for oxygen enriched biomass combustion,” *Proc. Combust. Inst.*, vol. 35, no. 3, pp. 2777–2784, 2015.

[23] D. Bäckström, R. Johansson, K. Andersson, H. Wiinikka, and C. Fredriksson, “On the use of alternative fuels in rotary kiln burners — An experimental and modelling study of the effect on the radiative heat transfer conditions,” *Fuel Process. Technol.*, vol. 138, pp. 210–220, 2015.

[24] A. K. Furre, O. Eiken, H. Alnes, J. Nesland Vevatne, and A. F. Kiær, “20 Years of Monitoring CO_2-injection at Sleipner,” *Energy Procedia*, vol. 114, no. August 1997, pp. 3916–3926, 2017.

[25] K. Andersson, R. Johansson, S. Hjärtstam, F. Johnsson, and B. Leckner, “Radiation intensity of lignite-fired oxy-fuel flames,” *Exp. Therm. Fluid Sci.*, vol. 33, no. 1, pp. 67–76, 2008.

[26] K. Andersson, R. Johansson, F. Johnsson, and B. Leckner, “Radiation Intensity of Propane-Fired Oxy-Fuel Flames: Implications for Soot Formation,” *Energy & Fuels*, vol. 22, no. 3, pp. 1535–1541, 2008.

[27] W. Merchan-Merchan, S. McCollam, and J. F. C. Pugliese, “Soot formation in diffusion oxygen-enhanced biodiesel flames,” *Fuel*, vol. 156, pp. 129–141, 2015.

[28] C. R. Shaddix and T. C. Williams, “The effect of oxygen enrichment on soot formation and thermal radiation in turbulent, non-premixed methane flames,” *Proc. Combust. Inst.*,

vol. 36, pp. 4051–4059, 2017.

[29] L. Wang, N. E. Endrud, S. R. Turns, M. D. D'Agostini, and A. G. Slavejkov, "A Study of the Influence of Oxygen Index on Soot , Radiation , and Emission Characteristics of Turbulent Jet Flames," *Combust. Sci. Technol.*, vol. 174, no. 8, pp. 45–72, 2002.

[30] K. Lee, C. M. Megaridis, S. Zelepouga, A. V Saveliev, L. A. Kennedy, O. Charon, and F. Ammouri, "Soot Formation Effects of Oxygen Concentration in the Oxidizer Stream of Laminar Coannular Nonpremixed Methane / Air Flames," *Combust. Flame*, vol. 121, pp. 323–333, 2000.

[31] S. A. Zelepouga, A. V Saveliev, L. A. Kennedy, and A. A. Fridman, "Relative Effect of Acetylene and PAHs Addition on Soot Formation in Laminar Diffusion Flames of Methane with Oxygen and Oxygen-Enriched Air," *Combust. Flame*, vol. 122, no. 1, pp. 76–89, 2000.

[32] K. C. Oh and H. D. Shin, "The effect of oxygen and carbon dioxide concentration on soot formation in non-premixed flames," *Fuel*, vol. 85, no. 5–6, pp. 615–624, 2006.

[33] F. Liu, H. Guo, G. J. Smallwood, and Ö. L. Gülder, "The Chemical Effects of Carbon Dioxide as an Additive in an Ethylene Diffusion Flame : Implications for Soot and NOx Formation," *Combust. Flame*, vol. 125, pp. 778–787, 2001.

[34] C. E. Baukal, *Oxygen-Enhanced Combustion*, 2nd ed. 2013.

[35] T. R. Barfknecht, "Toxicology of soot," *Prog. Energy Combust. Sci.*, vol. 9, no. 3, pp. 199–237, 1983.

[36] J. M. Samet, F. Dominici, F. C. Curriero, I. Coursac, and S. L. Zeger, "Fine Particulate Air Pollution and Moratlity in 20 U.S. Cities, 1987-1994," *N. Engl. J. Med.*, vol. 343, no. 24, pp. 1742–1749, 2000.

[37] C. Y. C. Jonsson, J. Stjernberg, H. Wiinikka, B. Lindblom, D. Boström, and M. Öhman, "Deposit formation in a grate-kiln plant for iron-ore pellet production. Part 1: Characterization process gas particles," *Energy and Fuels*, vol. 27, no. 10, pp. 6159–6170, 2013.

[38] F. Herz, I. Mitov, E. Specht, and R. Stanev, "Experimental study of the contact heat transfer coefficient between the covered wall and solid bed in rotary drums," *Chem. Eng. Sci.*, vol. 82, pp. 312–318, 2012.

[39] F. Herz, I. Mitov, E. Specht, and R. Stanev, "Influence of the Motion Behavior on the Contact Heat Transfer Between the Covered Wall and Solid Bed in Rotary Kilns," *Exp. Heat Transf.*, vol. 28, no. 2, pp. 174–188, 2015.

[40] G. W. J. Wes, A. A. H. Drinkenburg, and S. Stemerding, "Heat Transfer in a Horizontal Rotary Drum Reactor," *Powder Technol.*, vol. 13, no. 2, pp. 185–192, 1976.

[41] S. H. Tscheng and A. P. Watkinson, "Convective Heat Transfer in a Rotary Kiln," *Can. J. Chem. Eng.*, vol. 57, pp. 433–443, 1979.

[42] J. P. Gorog, T. N. Adams, and J. K. Brimacombe, "Regenerative Heat Transfer in Rotary Kilns," *Metall. Trans. B*, vol. 13, no. 2, pp. 153–163, 1982.

[43] J. P. Gorog, J. K. Brimacombe, and T. N. Adams, “Radiative heat transfer in rotary kilns,” *Metall. Trans. B*, vol. 12, no. 1, pp. 55–70, 1981.

[44] P. V. Barr, J. K. Brimacombe, and A. P. Watkinson, “A heat-transfer model for the rotary kiln: Part II. Development of the Cross-Section Model,” *Metall. Mater. Trans. B*, vol. 20, no. 3, pp. 403–419, 1989.

[45] A. A. Boateng and P. V. Barr, “A thermal model for the rotary kiln including heat transfer within the bed,” *Int. J. Heat Mass Transf.*, vol. 39, no. 10, pp. 2131–2147, 1996.

[46] J. P. Gorog, T. N. Adams, and J. K. Brimacombe, “Heat Transfer from Flames in a Rotary Kiln,” *Metall. Trans. B*, vol. 14, no. 3, pp. 411–424, 1983.

[47] U.S. Geological Survey, “Mineral commodity summaries 2019,” 2019.

[48] International Energy Agency, “CO_2 emissions from fuel combustion overview: overview,” 2018.

[49] Naturvårdsverket, “Utsläpp i siffror,” 2019. .

[50] H. C. Hottel and A. F. Sarofim, *Radiative Transfer*, 1st ed. United States of America: McGraw-Hill, Inc., 1967.

[51] R. Siegel and J. R. Howell, *Thermal Radiation Heat Transfer*. United States of America: McGraw-Hill, Inc., 1972.

[52] M. N. Özisik, *Radiative Transfer and Interactions with Conduction and Convection*. United States of America: John Wiley & Sons, Inc., 1973.

[53] D. Bäckström, R. Johansson, K. Andersson, F. Johnsson, S. Clausen, and A. Fateev, “Gas Temperature and Radiative Heat Transfer in Oxy-Fuel Flames,” in *37th International Technical Conference on Clean Coal & Fuel Systems, Clearwater Clean Coal Conference*, 2012.

[54] D. Bäckström, R. Johansson, K. Andersson, F. Johnsson, S. Clausen, and A. Fateev, “Measurement and modeling of particle radiation in coal flames,” *Energy and Fuels*, vol. 28, no. 3, pp. 2199–2210, 2014.

[55] D. Bäckström, D. Gall, M. Pushp, R. Johansson, K. Andersson, and J. B. C. Pettersson, “Particle composition and size distribution in coal flames – The influence on radiative heat transfer,” *Exp. Therm. Fluid Sci.*, vol. 64, pp. 70–80, 2015.

[56] D. Bäckström, A. Gunnarsson, D. Gall, X. Pei, R. Johansson, K. Andersson, R. Kant Pathak, and J. B. C. Pettersson, “Measurements of the size distribution, volume fraction and optical properties of soot in an 80 kW propane flame,” 2017.

[57] B. Axelsson, R. Collin, and P. E. Bengtsson, “Laser-induced incandescence for soot particle size and volume fraction measurements using on-line extinction calibration,” *Appl. Phys. B*, vol. 72, no. 3, pp. 367–372, 2001.

[58] A. Gunnarsson, J. Simonsson, D. Bäckström, M. N. Mannazhi, P. E. Bengtsson, and K. Andersson, “Radiative Heat Transfer Modeling and in Situ Diagnostics of Soot in an 80 kWth Propane Flame with Varying Feed-Gas Oxygen Concentration,” *Ind. Eng. Chem. Res.*, vol. 57, no. 36, pp. 12288–12295, 2018.

[59] J. Simonsson, A. Gunnarsson, M. N. Mannazhi, D. Bäckström, K. Andersson, and P.-E. Bengtsson, “In-situ soot characterization of propane flames and influence of additives in a 100 kW oxy-fuel furnace using two-dimensional laser-induced incandescence,” *Proc. Combust. Inst.*, vol. 37, pp. 833–840, 2018.

[60] R. Johansson, B. Leckner, K. Andersson, and F. Johnsson, “Account for variations in the H_2O to CO_2 molar ratio when modelling gaseous radiative heat transfer with the weighted-sum-of-grey-gases model,” *Combust. Flame*, vol. 158, no. 5, pp. 893–901, 2011.

[61] R. M. Goody, “A statistical model for water-vapour absorption,” *R. Meteorol. Soc.*, vol. 78, no. 338, pp. 165–169, 1952.

[62] W. Malkmus, “Random Lorentz Band Model with Exponential-Tailed S-1 Line-Intensity Distribution Function,” *J. Opt. Soc. Am.*, vol. 57, no. 3, pp. 323–329, 1967.

[63] A. Soufiani and J. Taine, “High temperature gas radiative property parameters of statistical narrow-band model for H_2O, CO_2 and CO, and correlated-K model for H_2O and CO_2,” *Int. J. Heat Mass Transf.*, vol. 40, no. 4, pp. 987–991, 1996.

[64] P. Rivière and A. Soufiani, “Updated band model parameters for H_2O, CO_2, CH_4 and CO radiation at high temperature,” *Int. J. Heat Mass Transf.*, vol. 55, no. 13–14, pp. 3349–3358, 2012.

[65] S. J. Young, “Nonisothermal band model theory,” *J. Quant. Spectrosc. Radiat. Transf.*, vol. 18, no. 1, pp. 1–28, 1977.

[66] Y. Yamada, J. D. Cartigny, and C. L. Tien, “Radiative Transfer With Dependent Scattering by Particles : Part 2 — Experimental Investigation,” *J. Heat Transfer*, vol. 108, pp. 614–618, 1986.

[67] A. R. Coderre, K. A. Thomson, D. R. Snelling, and M. R. Johnson, “Spectrally resolved light absorption properties of cooled soot from a methane flame,” *Appl. Phys. B Lasers Opt.*, vol. 104, no. 1, pp. 175–188, 2011.

[68] G. Mie, “Beiträge zur Optik trüber Medien, speziell kolloidaler Metallösungen,” *Ann. Phys.*, vol. 25, no. 3, pp. 377–445, 1908.

[69] H. C. van de Hulst, *Light Scattering By Small Particles*. New York: Dover Publications, 1981.

[70] C. F. Bohren and D. R. Huffman, *Absorption and Scattering of Light by Small Particles*. 1983.

[71] P. J. Foster and C. R. Howarth, “Optical Constants of Carbons and Coals in the Infrared,” *Carbon N. Y.*, vol. 6, no. 5, pp. 719–729, 1968.

[72] A. Lohi, J. R. Wynnyckyj, and E. Rhodes, “Spectral measurement of the complex refractive index of fly ashes of canadian lignite and sub-bituminous coals,” *Can. J. Chem. Eng.*, vol. 70, no. 4, pp. 751–758, 1992.

[73] R. P. Gupta and T. F. Wall, “The optical properties of fly ash in coal fired furnaces,” *Combust. Flame*, vol. 61, no. 2, pp. 145–151, 1985.

[74] D. G. Goodwin and M. Mitchner, “Flyash Radiative Properties and Effects on Radiative Heat-Transfer in Coal-fired Systems,” *Int. J. Heat Mass Transf.*, vol. 32, no. 4, pp. 627–638, 1989.

[75] R. Johansson, B. Leckner, K. Andersson, and F. Johnsson, “Influence of particle and gas radiation in oxy-fuel combustion,” *Int. J. Heat Mass Transf.*, vol. 65, pp. 143–152, 2013.

[76] W. A. Fiveland, “Three-Dimensional Radiative Heat-Transfer Solutions by the Discrete-Ordinates Method,” *J. Thermophys. Heat Transf.*, vol. 2, no. 4, pp. 309–316, 1988.

[77] J. R. Tsai and M. N. Özişik, “Radiation in cylindrical symmetry with anisotropic scattering and variable properties,” *Int. J. Heat Mass Transf.*, vol. 33, no. 12, pp. 2651–2658, 1990.

[78] A. S. Jamaluddin and P. J. Smith, “Predicting Radiative Transfer in Axisymmetric Cylindrical Enclosures Using the Discrete Ordinates Method,” *Combust. Sci. Technol.*, vol. 62, no. 4–6, pp. 173–186, 1988.

[79] F. C. Lockwood and N. G. Shah, “A new radiation solution method for incorporation in general combustion prediction procedures,” *Proc. Combust. Inst.*, vol. 18, pp. 1405–1414, 1981.

[80] B. G. Carlson and K. D. Lathrop, “Transport Theory The Method of Discrete Ordinates,” in *Computing Methods in Reactor Physics*, 1st ed., H. Greenspan, C. N. Kelber, and D. Okrent, Eds. New York: Gordon and Breach Science Publishers, 1968, pp. 171–265.

[81] A. S. Jamaluddin and P. J. Smith, “Discrete-Ordinates Solution of Radiative Transfer Equation in Nonaxisymmetric Cylindrical Enclosures,” *J. Thermophys. Heat Transf.*, vol. 6, no. 2, pp. 242–245, 1992.

[82] M. Y. Kim and S. W. Baek, “Modeling of radiative heat transfer in an axisymmetric cylindrical enclosure with participating medium,” *J. Quant. Spectrosc. Radiat. Transf.*, vol. 90, no. 3–4, pp. 377–388, 2005.

[83] G. J. Thornton and R. J. Batterham, “The Transfer of Heat in Kilns,” in *Tenth Australian Chemical Engineering Conference*, 1982, pp. 260–266.

[84] J. Liu, H. M. Shang, and Y. S. Chen, “Development of an unstructured radiation model applicable for two-dimensional planar, axisymmetric, and three-dimensional geometries,” *J. Quant. Spectrosc. Radiat. Transf.*, vol. 66, no. 1, pp. 17–33, 2000.

[85] T. Gronarz, M. Schnell, C. Siewert, L. Schneiders, W. Schröder, and R. Kneer, “Comparison of scattering behaviour for spherical and non-spherical particles in pulverized coal combustion,” *Int. J. Therm. Sci.*, vol. 111, pp. 116–128, 2017.

[86] T. Gronarz, J. Schulze, M. Laemmerhold, P. Graeser, J. Gorewoda, V. Kez, M. Habermehl, M. Schiemann, J. Ströhle, B. Epple, V. Scherer, and R. Kneer, “Quantification of the influence of parameters determining radiative heat transfer in an oxy-fuel operated boiler,” *Fuel Process. Technol.*, vol. 157, pp. 76–89, 2017.

[87] H. Henein, J. K. Brimacombe, and A. P. Watkinson, “Experimental Study of Transverse Bed Motion in Rotary Kilns,” *Metall. Trans. B*, vol. 14, no. 2, pp. 191–205, 1983.

[88] E. U. Schlünder and N. Mollekopf, “Vacuum contact drying of free flowing

mechanically agitated particulate material," *Chem. Eng. Process.*, vol. 18, no. 2, pp. 93–111, 1984.

[89] S. Q. Li, L. B. Ma, W. Wan, and Q. Yao, "A mathematical model of heat transfer in a rotary kiln thermo-reactor," *Chem. Eng. Technol.*, vol. 28, no. 12, pp. 1480–1489, 2005.

[90] F. P. Incropera, D. P. Dewitt, T. L. Bergman, and A. S. Lavine, *Principles of Heat and Mass Transfer*, Seventh. Hoboken: John Wiley & Sons, Inc., 2013.

[91] W. D. Owens, G. D. Silcox, J. S. Lighty, X. X. Deng, D. W. Pershing, V. A. Cundy, C. B. Leger, and A. L. Jakway, "Thermal Analysis of Rotary Kiln Incineration: Comparison of Theory and Experiment," *Combust. Flame*, vol. 86, no. 1–2, pp. 101–114, 1991.

[92] L. Le Guen, M. Piton, Q. Hénaut, F. Huchet, and P. Richard, "Heat convection and radiation in flighted rotary kilns: A minimal model," *Can. J. Chem. Eng.*, vol. 95, no. 1, pp. 100–110, 2017.

[93] S. P. E. Forsmo, S.-E. Forsmo, P.-O. Samskog, and B. M. T. Björkman, "Mechanisms in oxidation and sintering of magnetite iron ore green pellets," *Powder Technol.*, vol. 183, no. 2, pp. 247–259, 2008.

[94] R. A. Davis, "Mathematical Model of Magnetite Oxidation in a Rotary Kiln furnace," *Can. J. Chem. Eng.*, vol. 74, pp. 1004–1009, 1996.

[95] S. G. Melamud and B. P. Yur'ev, "Oxidation of iron ore at moderate and high temperatures," *Steel Transl.*, vol. 46, no. 6, pp. 384–389, 2016.

[96] T. K. Sandeep Kumar, N. N. Viswanathan, H. Ahmed, A. Dahlin, C. Andersson, and B. Bjorkman, "Developing the Oxidation Kinetic Model for Magnetite Pellet," *Metall. Mater. Trans. B*, vol. 50, no. 1, pp. 162–172, 2018.

[97] S. W. Churchill and H. H. S. Chu, "Correlating Equations For Laminar and Turbulent Free Convection From a Horizontal Cylinder," *Int. J. Heat Mass Transf.*, vol. 18, no. 9, pp. 1049–1053, 1975.

[98] P. R. Griffiths and J. A. Haseth, *Fourier Transform Infrared Spectrometry*, Second Edi. John Wiley & Sons, Inc., 2007.

[99] W. Zhang, F. Johnsson, and B. Leckner, "Momentum probe and sampling probe for measurement of particle flow properties in CFB boilers," *Chem. Eng. Sci.*, vol. 52, no. 4, pp. 497–509, 1997.

[100] F. R. Quant, R. C. Flagan, and K. D. Horton, "Implementation of a Scanning Mobility Particle Sizer (SMPS)," *J. Aerosol Sci.*, vol. 24, no. 1, pp. 83–84, 1993.

[101] J. Pagels, M. Strand, J. Rissler, A. Szpila, A. Gudmundsson, M. Bohgard, L. Lillieblad, M. Sanati, and E. Swietlicki, "Characteristics of aerosol particles formed during grate combustion of moist forest residue," *J. Aerosol Sci.*, vol. 34, no. 8, pp. 1043–1059, 2003.

[102] M. Strand, M. Bohgard, E. Swietlicki, A. Gharibi, and M. Sanati, "Laboratory and field test of a sampling method for characterization of combustion aerosols at high temperatures," *Aerosol Sci. Technol.*, vol. 38, no. 8, pp. 757–765, 2004.

[103] S. C. Wang and R. C. Flagan, "Scanning Electrical Mobility Spectrometer," *J. Aerosol*

Sci., vol. 20, no. 8, pp. 1485–1488, 1989.

[104] H. Moosmüller, R. K. Chakrabarty, and W. P. Arnott, "Aerosol light absorption and its measurement: A review," *J. Quant. Spectrosc. Radiat. Transf.*, vol. 110, no. 11, pp. 844–878, 2009.

[105] G. D. Yoder, P. K. Diwakar, and D. W. Hahn, "Assessment of soot particle vaporization effects during laser-induced incandescence with time-resolved light scattering.," *Appl. Opt.*, vol. 44, no. 20, pp. 4211–4219, 2005.

[106] R. L. Vander Wal and K. J. Weiland, "Laser-Induced incandescence: Development and characterization towards a measurement of soot-volume fraction," *Appl. Phys. B Laser Opt.*, vol. 59, pp. 445–452, 1994.

[107] H. Bladh, J. Johnsson, and P. E. Bengtsson, "On the dependence of the laser-induced incandescence (LII) signal on soot volume fraction for variations in particle size," *Appl. Phys. B Lasers Opt.*, vol. 90, no. 1, pp. 109–125, 2008.

[108] R. Edland, F. Normann, C. Fredriksson, and K. Andersson, "Implications of Fuel Choice and Burner Settings for Combustion Efficiency and NOxFormation in PF-Fired Iron Ore Rotary Kilns," *Energy and Fuels*, vol. 31, no. 3, pp. 3253–3261, 2017.

[109] S. Hjärtstam, R. Johansson, K. Andersson, and F. Johnsson, "Computational fluid dynamics modeling of oxy-fuel flames: The role of soot and gas radiation," *Energy and Fuels*, vol. 26, no. 5, pp. 2786–2797, 2012.

[110] E. G. Eddings, D. McAvoy, and R. L. Coates, "Co-firing of pulverized coal with Pinion Pine/Juniper wood in raw, torrefied and pyrolyzed forms," *Fuel Process. Technol.*, vol. 161, pp. 273–282, 2017.

[111] A. Fry, B. Adams, A. Paschedag, P. Kazalski, C. Carney, D. Oryshchyn, R. Woodside, S. Gerdemann, and T. Ochs, "Principles for retrofitting coal burners for oxy-combustion," *Int. J. Greenh. Gas Control*, vol. 5, no. SUPPL. 1, pp. 151–158, 2011.